

**Spinpolarisierter Transport
in
epitaktischen
Manganoxid-
und
Doppelperowskitschichten**

Dissertation
zur Erlangung des Grades
Doktor der Naturwissenschaften (Dr. rer. nat.)
am Fachbereich Physik
der Johannes Gutenberg-Universität Mainz

von
Wilhelm Westerbürg
geb. in Nastätten

**UNIVER
SITÄT 
MAINZ**

Mainz, 2000
D 77

Tag der Einreichung: 06.10.2000
Tag der mündlichen Prüfung: 23.07.2001

**Spin Polarized Transport
in
Manganese Oxide
and
Double-Perovskite Thin Films**

Ph.D. thesis
by
Wilhelm Westerburg



Mainz, Germany 2000

*“Electrons have spin as well as charge, and this may make
all the difference in future electronics.”*

Gary A. Prinz

Physics Today, April 1995

Meinen Eltern und Nicole

Contents

Introduction and motivation	1
1 Properties of perovskites	5
1.1 Crystal structure	5
1.2 Magnetic perovskites	6
1.2.1 Undoped perovskites $AMnO_3$	7
1.2.2 Hole-doped manganites	8
1.2.3 Double-exchange	9
1.3 Spin polarized transport	10
1.4 Hall effect in ferromagnetic materials	11
1.5 X-ray and neutron scattering	14
1.5.1 X-ray diffraction	14
1.5.2 Neutron diffraction	15
1.5.3 Rietveld refinement	17
2 Ca- and Sr-doped epitaxially grown manganite thin films	19
2.1 Preparation and characterization	20
2.2 Magnetotransport measurements	24
2.3 Charge-carrier density collapse	26
2.4 Conclusion	33
3 Artificial grain boundaries in $La_{0.67}Ca_{0.33}MnO_3$ thin films	35
3.1 Thin film deposition on bicrystal substrates	36
3.2 Characterization	36
3.2.1 Crystallographic properties	36
3.2.2 Morphology	37
3.3 Magnetotransport	39
3.3.1 Simmons model of tunneling	39
3.3.2 Jullière model of tunneling	42
3.3.3 Low-field magnetoresistance	44
3.3.4 Current dependence of magnetoresistance	47
3.4 Summary	51

4	Epitaxial double-perovskite $\text{Sr}_2\text{FeMoO}_6$ thin films	53
4.1	Thin film fabrication	53
4.2	Half-metallic ground state	54
4.3	Crystal structure	55
4.4	Morphology	62
4.5	Magnetotransport	63
4.5.1	Longitudinal resistivity	63
4.5.2	Double-exchange-like mechanism	69
4.5.3	Hall effect	70
4.6	Magnetization	72
4.7	Summary	74
5	Investigation of double-perovskite $\text{Ca}_2\text{FeReO}_6$	77
5.1	Powder preparation and experiment	77
5.2	Crystal structure	79
5.2.1	Neutron diffraction	79
5.2.2	X-ray diffraction	88
5.3	Magnetic properties	89
5.3.1	Magnetic susceptibility	89
5.3.2	DC magnetization	90
5.3.3	Magnetic structure from neutron scattering	91
5.4	^{57}Fe -Mössbauer measurements	92
5.5	Transport properties	94
5.6	Conclusion	95
	Summary	99
A	Symmetry elements in the monoclinic space group $P2_1/n$	103
B	Preparation parameters	105
C	Rietveld refinement with FULLPROF	109
	Bibliography	123
	List of Publications	137
	Curriculum Vitae	139
	Acknowledgements	141

List of Figures

1	Roadmap for areal densities in hard disk drives.	1
2	Schematic diagram of a magnetic random access memory.	2
1.1	Ideal cubic perovskite structure.	6
1.2	Energy level scheme for LaMnO_3	7
1.3	Phase diagrams for Ca- and Sr-doped manganites.	8
1.4	Schematic energy level diagram for Ni and $\text{La}_{0.67}\text{Sr}_{0.33}\text{MnO}_3$	11
1.5	Schematic view of $V_{\text{Hall}}(B)$ for a ferromagnet.	12
2.1	$\theta/2\theta$ -scan of $\text{La}_{0.67}\text{Sr}_{0.33}\text{MnO}_3$	21
2.2	Bitter type magnet.	23
2.3	Resistivities in zero field and in $B = 8$ T.	24
2.4	Magnetoresistance (MR) at $T = 300$ K.	26
2.5	Hall resistivity and Hall voltage of $\text{La}_{0.67}\text{Sr}_{0.33}\text{MnO}_3$	27
2.6	Ferromagnetic hysteresis curve for $\text{La}_{0.67}\text{Ca}_{0.33}\text{MnO}_3$	28
2.7	Measured Hall resistivity of $\text{La}_{0.67}\text{Ca}_{0.33}\text{MnO}_3$	29
2.8	Normalized charge-carrier density versus temperature.	30
2.9	Data compilation of $\text{La}_{0.67}\text{Ca}_{0.33}\text{MnO}_3$	32
3.1	$\theta/2\theta$ -scan of $\text{La}_{0.67}\text{Ca}_{0.33}\text{MnO}_3$	36
3.2	ϕ -scan of $\text{La}_{0.67}\text{Ca}_{0.33}\text{MnO}_3$	37
3.3	AFM and SEM scan of the grain boundary (GB).	38
3.4	Patterned thin film geometry on the bicrystal substrate.	39
3.5	Rectangular potential barrier.	40
3.6	Density of states in the junction.	43
3.7	GB resistance and MR at $T = 4.2$ K as a function of B	44
3.8	Hysteretic low-field MR.	45
3.9	Temperature dependence of the maximum low-field MR.	46
3.10	I - V curves in zero field at $T = 4.2$ K.	47
3.11	Differential conductivity of GB meander.	48
3.12	Hysteresis loops of the low-field MR.	49
3.13	Decrease of the low-field MR at the GB with increasing I	50
3.14	Reversible MR of the GB meander as function of B	51

4.1	Density of states of $\text{Sr}_2\text{FeMoO}_6$	54
4.2	Perovskite unit cell.	55
4.3	$\theta/2\theta$ -scans and rocking curves of $\text{Sr}_2\text{FeMoO}_6$	56
4.4	Dependence of lattice parameters on T_D	57
4.5	hk scans for constant l values.	58
4.6	ϕ -scan of the $\text{Sr}_2\text{FeMoO}_6$ $\{311\}$ reflections.	59
4.7	kl scans for $h = 2$	61
4.8	SEM area scans of sample A and B.	62
4.9	$\rho_{xx}(T)$ for the semiconducting sample A.	63
4.10	Detailed temperature dependence of ρ_{xx}	64
4.11	$\rho_{xx}(T)$ for the metallic sample B.	65
4.12	High field MR below and above the Curie temperature T_C	66
4.13	Transition from semiconducting to metallic behavior.	68
4.14	Dependence of the rocking curve width $\Delta\omega$ on T_D	69
4.15	Hall voltage of $\text{Sr}_2\text{FeMoO}_6$ as a function of magnetic field.	70
4.16	Magnetic hysteresis loops measured at $T = 10$ K.	73
5.1	Crystal structure for different B, B' arrangements.	79
5.2	Neutron diffraction pattern of $\text{Ca}_2\text{FeReO}_6$ at $T = 548$ K.	80
5.3	View of the monoclinic unit cell.	81
5.4	Temperature dependence of the (040) reflection peak.	83
5.5	Neutron diffraction pattern for $\text{Ca}_2\text{FeReO}_6$ at $T = 2$ K.	85
5.6	Temperature dependence of the lattice constants and the β angle.	86
5.7	X-ray powder diffraction pattern taken at room temperature.	88
5.8	Temperature dependence of the AC susceptibility.	89
5.9	Hysteresis loops.	90
5.10	Temperature dependence of the (011) and (101) Bragg peaks.	91
5.11	^{57}Fe -Mössbauer spectra.	93
5.12	Temperature dependence of the longitudinal resistivity.	95
5.13	$\theta/2\theta$ -scans of $A_2\text{FeReO}_6$ ($A = \text{Ba}, \text{Sr}, \text{and Ca}$).	97
A.1	Glide plane in $\text{Ca}_2\text{FeReO}_6$	103
A.2	Screw axis in $\text{Ca}_2\text{FeReO}_6$	104

List of Tables

2.1	X-ray transitions in ionized Cu.	22
2.2	Fitting parameters for $\text{La}_{0.67}\text{Ca}_{0.33}\text{MnO}_3$ and $\text{La}_{0.67}\text{Sr}_{0.33}\text{MnO}_3$. . .	25
4.1	Differences in physical properties of sample A and sample B. . . .	74
5.1	Positional and thermal parameters at 548 K.	82
5.2	Lattice constants and β angles.	84
5.3	Positional and thermal parameters at 2 K.	86
5.4	Bond lengths and bond angles for $\text{Ca}_2\text{FeReO}_6$ at 2 K and 548 K. .	87
5.5	Mössbauer parameters for $\text{Ca}_2\text{FeReO}_6$	92
5.6	Properties of $A_2\text{FeMoO}_6$ and $A_2\text{FeReO}_6$	96
B.1	$\text{La}_{0.67}\text{Sr}_{0.33}\text{MnO}_3$ target preparation procedure.	105
B.2	Laser ablation parameters for manganites.	106
B.3	Sputtering parameters for manganites.	106
B.4	$\text{Sr}_2\text{FeMoO}_6$ target preparation procedure.	107
B.5	Laser ablation parameters for $\text{Sr}_2\text{FeMoO}_6$	107
B.6	Patterning parameters for manganites.	108
B.7	Patterning parameters for $\text{Sr}_2\text{FeMoO}_6$	108

Introduction and motivation

During its brilliant half-century-long success story, electronics has almost completely ignored the spin of the electron. This situation is currently changing, with the emergence of a novel field investigating spin polarized transport. Magneto-electronics, Spin Electronics, and Spintronics are different names for the same thing: the use of electrons spins (not just their electrical charge) in information circuits. Spin transistors are possible devices in the future [1]. The latest demonstration of spin versatility is the organized movement of a herd of spins over a lateral distance of $100 \mu\text{m}$ [2]. Such coherence will be necessary if spin currents are used to transport information from place to place, particularly in quantum computers. Nowadays two technical applications, spin valves and magnetic random access memories, are realized.

Already 10 years after the giant magnetoresistive (GMR) effect was discovered in the late 1980s by two European scientists Peter Grünberg [3] and Albert Fert [4], IBM exploits this effect in new sensors called spin valves. Already a billion dollar business, GMR read-heads boost disk drive areal densities above

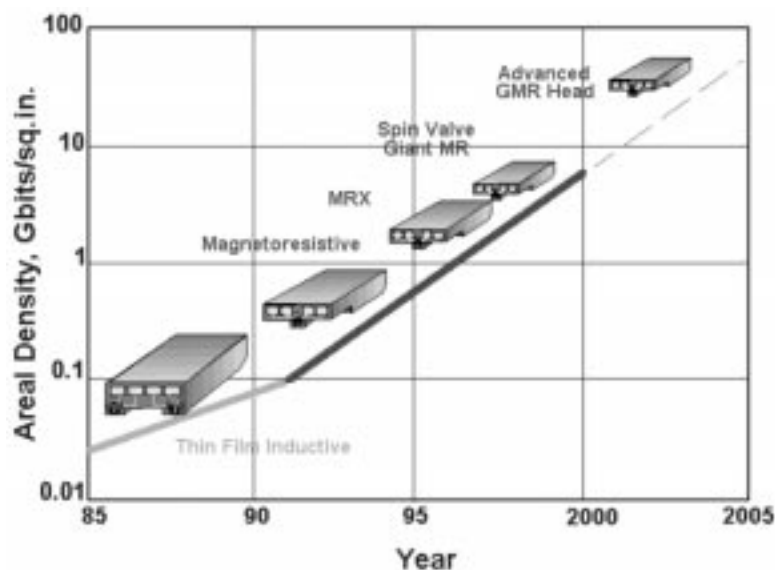


Figure 1: Roadmap for areal densities in hard disk drives with different read-head technologies [5].

35 Gbits/in². The sensors are sputtered polycrystalline multilayers consisting of a stack of alternating layers of magnetic and nonmagnetic atoms (Co/Cu/NiFe).

There is great interest in a novel magnetic storage concept which retains its memory even after removing power from the device. Such a nonvolatile memory has important military applications for missiles and satellites. Clearly such a device could also have important commercial applications if the nonvolatility is accomplished without impacting other properties of the memory, notably density, read and write speed, as well as lifetime. One possible device is the magnetic

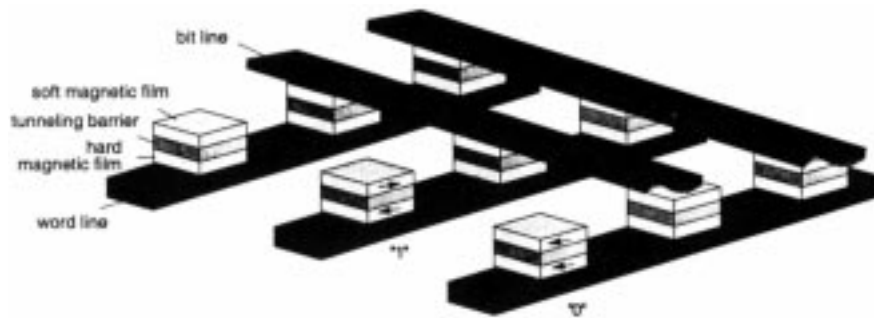


Figure 2: *Schematic diagram of a magnetic random access memory [6].*

random access memory (MRAM), using the tunnel magnetoresistance (TMR), consisting of two ferromagnetic layers separated by an insulating tunnel barrier as Al_2O_3 or SrTiO_3 . The magnetic alignment of one layer can be changed without affecting the other. This permits one to store binary information. A parallel (antiparallel) alignment of the magnetization in the two layers, i.e. a low (high) resistance of the tunnel junction, may correspond to a bit '0' ('1'). IBM presented already a 1 kbit MRAM prototype with read/write times of 10 ns. A further application is to replace the GMR read-heads by new TMR elements to reach even higher areal densities in hard disk drives.

The ferromagnetic materials used up to now in these devices were transition metal ferromagnets and their alloys. Their spin polarization is in general below 40% which restricts the sensitivity of devices built up of these materials. Higher sensitivity is possible with half-metallic materials, i.e. compounds with a complete spin polarization of the conduction band as Heusler alloys (NiMnSb), chromium dioxide (CrO_2), pyrochlores ($\text{Tl}_2\text{Mn}_2\text{O}_7$), perovskites as manganites ($\text{La}_{1-x}\text{A}_x\text{MnO}_3$), and double-perovskites ($\text{Sr}_2\text{FeMoO}_6$). Half-metals are in the majority of cases metallic oxide ferromagnets that have predominantly d orbital character at the Fermi level. An obstacle for applications is, in most cases, the fact that ideal half-metallic behavior is expected only at low temperatures where thermal excitation of magnons is weak, and a significant gap exists for one electron spin direction. Hence, it is desirable to have a material with a high spin polarization and a high Curie temperature.

This thesis is focused on the investigation of magnetic perovskites. The task was to find the material suitable in relation to practical applications, to deposit it as an epitaxial thin film, and to investigate its crystal structure, as well as its magnetotransport properties.

Most of the experiments of the present work were carried out at the Institute of Physics at the University of Mainz in Germany. Part of the Hall effect measurements took place at the High Field Magnet Laboratory at the University of Nijmegen in the Netherlands. The neutron diffraction measurements were performed at the Institute Laue Langevin at Grenoble in France.

An introductory overview of perovskites, spin polarized transport, and the Hall effect in ferromagnets is given in the first chapter. In the second chapter the magnetotransport properties of epitaxial $\text{La}_{0.67}\text{Sr}_{0.33}\text{MnO}_3$ thin films in comparison with $\text{La}_{0.67}\text{Ca}_{0.33}\text{MnO}_3$ thin films are presented. The main focus is the investigation of the temperature dependence of the charge-carrier density. By replacing the dopant atom from Ca to Sr it was possible to shift the Curie temperature from 240 K to 340 K and to enhance the intrinsic colossal magnetoresistance at room temperature. Nevertheless, the sensitivity needed for applications was not achieved, i.e. large magnetic fields are necessary to obtain significant changes in resistivity. Therefore, epitaxial $\text{La}_{0.67}\text{Ca}_{0.33}\text{MnO}_3$ thin films on bicrystal substrates were studied. The results are shown in the third chapter. Due to spin polarized tunneling in the artificial grain boundary, large magnetoresistance effects in low magnetic fields were observed at low temperatures. However, the low-field tunnel magnetoresistance decreases with increasing temperature due to magnon excitations. In the meantime it became obvious that the manganites with their Curie temperatures below 400 K would hardly be a good candidate for practical devices which have to work at ambient temperature.

In 1998 Kobayashi *et al.* [7] determined the magnetotransport properties of another oxide material with a higher Curie temperature above 400 K, the double-perovskite $\text{Sr}_2\text{FeMoO}_6$. As in the case of the manganites this compound was already previously investigated in the 1960s. On the basis of this publication efforts were concentrated to obtain epitaxial thin films of $\text{Sr}_2\text{FeMoO}_6$.

In the fourth chapter the preparation and structure-property relationship of $\text{Sr}_2\text{FeMoO}_6$ is presented. The last chapter finally deals with the investigation of $\text{Ca}_2\text{FeReO}_6$ a further double-perovskite with the highest Curie temperature of 540 K up to now published for perovskites. The main focus is the determination of the crystal structure of polycrystalline powder by neutron diffraction.

Chapter 1

Properties of perovskites

The most frequent minerals on earth are perovskites [8, 9]. This structure of metal atoms and nonmetal atoms usually oxygen was first described in the 1830s by the german chemist and mineralogist Gustav Rose, who named it after the famous russian mineralogist Count Lev Aleksevich von Perovski [10]. It is a key to understanding the history of earth. Synthetic perovskites are beside the natural perovskites of great technological importance, e.g. they are the backbone of the electroceramic industry. Since 1945, when the ferroelectric properties of BaTiO_3 were found, ABO_3 compounds with the perovskite structure have been investigated extensively. These studies have resulted in the discovery of many new ferroelectric, piezoelectric, superconducting and ferromagnetic materials. Nowadays, one goal of research is to reveal the structure-property relationship in detail to design the ideal material for the respective application. This work is focused on preparation, structure and properties of ferromagnetic perovskite-type compounds as epitaxial thin films.

1.1 Crystal structure

Most of the materials with the general formula ABO_3 crystallize in the perovskite structure which was first found for the mineral perovskite CaTiO_3 ¹. The ideal cubic structure is shown in Fig. 1.1. The large A cation, similar in size to O^{2-} , is coordinated with twelve oxygen ions, whereas the small B cation is surrounded by six oxygen ions, i.e. octahedrally-coordinated. The octahedra BO_6 themselves are corner-shared with the A atom in the interstitials formed by the oxygen octahedra. The anion can be replaced by a halide or chalcogenide ion which is not discussed here [13]. New perovskite-type compounds as AA'BB'O_6 could be prepared by introducing more than one element in the A and/or B position of the

¹The simple cubic structure has retained the name perovskite, even though CaTiO_3 was later determined to be orthorhombic [11, 12].

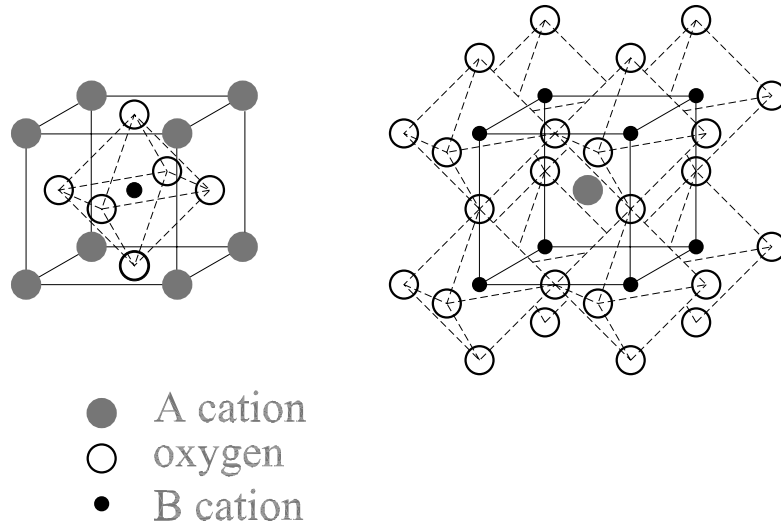


Figure 1.1: *The ideal cubic ABO_3 perovskite structure. A is a large cation and B is a small cation octahedrally-coordinated with oxygen.*

perovskite structure. The cubic perovskite structure is stable only if a tolerance factor t , given by

$$t = \frac{r_A + r_O}{\sqrt{2}(r_B + r_O)} \quad (1.1)$$

with r_A , r_B , and r_O the ionic radii has a value close to unity as shown by Goldschmidt [14]. In the arrangement with $t = 1$ the A , B , and O ion spheres have contact. The structure can be modified by cation displacements, tilts and/or distortions of the octahedra. This will be discussed in detail in the last chapter.

1.2 Magnetic perovskites

Ferromagnetic perovskites in the form of polycrystalline ceramic samples were investigated in the 1950s by Jonker and van Santen [15] working at Philips research laboratories in Eindhoven. They focused on the preparation, crystal structure, magnetic properties [16, 17], and electrical conductivity [18, 19] of the doping series $La_{1-x}A_xBO_3$ ($A = Ca, Sr, Ba$), called manganites ($B = Mn$) and cobaltites ($B = Co$). The manganites are nowadays of great interest due to their large magnetoresistance (MR), which is the relative change in the electrical resistivity of a material due to the application of a magnetic field. This effect was first discovered by Lord Kelvin [20] and is generally defined by

$$\text{MR} = \frac{\rho(T, \mu_0 H) - \rho(T, \mu_0 H = 0 \text{ T})}{\rho(T, \mu_0 H = 0 \text{ T})} = \frac{\rho(H) - \rho_0}{\rho_0}, \quad (1.2)$$

where $\rho(H)$ and ρ_0 are the resistivities at constant temperature in the presence and absence of an external magnetic field H , respectively. The MR can be positive

in nonmagnetic metals and alloys due to the Lorentz force or negative in magnetic materials due to the suppression of spin disorder by the magnetic field. In manganites a negative MR with peak values near the Curie temperature T_C was first reported in 1954 by Volger [21], but no further attention was paid to this unusual physical property. A comprehensive compilation of crystallographic and magnetic data on perovskites and related compounds including double-perovskites was published in the Landolt-Börnstein volume ‘*Magnetic and Other Properties of Oxides and Related Compounds*’ by Goodenough and Longo [22].

A strong theoretical and experimental interest on these meanwhile forgotten compounds revived 40 years later on the basis of a very large MR observed in single crystals by Kusters *et al.* [23] and thin films by Helmholt *et al.* [24], a phenomenon now called colossal magnetoresistance².

1.2.1 Undoped perovskites $AMnO_3$

A perovskite compound without hole doping such as $LaMnO_3$ is an insulator at all temperatures and is antiferromagnetic below the Néel temperature T_N of 150 K. Due to the Jahn-Teller effect of Mn^{3+} this compound is distorted into an orthorhombic structure [25]. The MnO_6 octahedra are deformed in such a way that there are long and short Mn — O bonds [26]. As a result of the Jahn-Teller distortion the conduction band is split and the material is insulating. Further, the octahedral crystal field eliminates the degeneracy of the five d orbitals in a t_{2g} triplet (d_{xy}, d_{xz}, d_{yz}) and e_g doublet ($d_{3z^2-r^2}, d_{x^2-y^2}$). The intraatomic Coulomb interaction enforces the compliance of Hund’s rule. The t_{2g}^3 electrons are localized on the Mn site giving rise to a local spin S of $3/2$, but the e_g state, which is

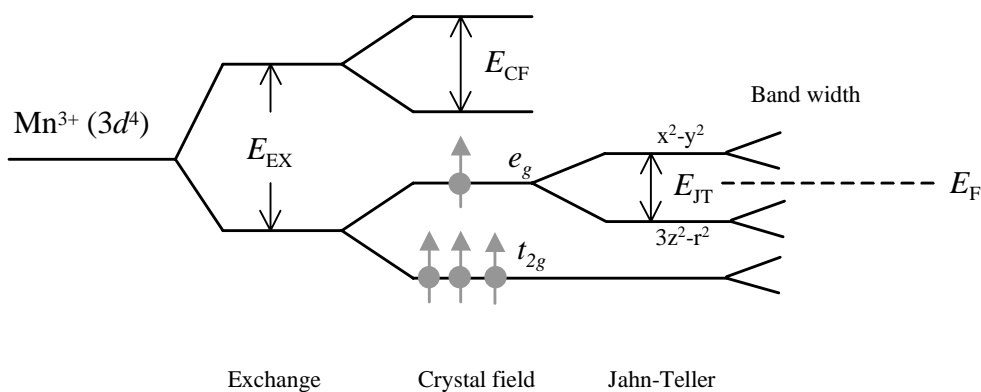


Figure 1.2: Energy level scheme for $LaMnO_3$ [27, 28]. The values for the exchange energy E_{EX} , crystal field energy E_{CF} , and Jahn-Teller energy E_{JT} are 3 eV, 2 eV and 1.5 eV, respectively. Typical bandwidth is 1.5 eV – 2.0 eV. The Fermi energy E_F is situated between the Jahn-Teller split orbitals.

²The term giant magnetoresistance was already assigned for large magnetoresistance effects in magnetic superlattices due to spin dependent scattering at the interfaces [4].

hybridized with the oxygen $2p$ state, can be localized or itinerant. In Fig. 1.2 the band diagram of LaMnO_3 is sketched.

1.2.2 Hole-doped manganites

The trivalent cation La^{3+} in LaMnO_3 can be progressively substituted by a divalent cation A such as Ca^{2+} or Sr^{2+} . This new perovskite can be regarded as a solid solution between $\text{La}^{3+}\text{Mn}^{3+}\text{O}_3^{2-}$ and $A^{2+}\text{Mn}^{4+}\text{O}_3^{2-}$, leading to a mixed-valence compound $(\text{La}_{1-x}A_x)(\text{Mn}_{1-x}^{3+}\text{Mn}_x^{4+})\text{O}_3^{2-}$. The orthorhombic distortion decreases to a pseudocubic symmetry. Also by oxygen deficiency the enforced valence fluctuation $\text{Mn}_{1-x}^{3+}\text{Mn}_x^{4+}$ on the B sites can be obtained. The hole-doped material becomes ferromagnetic and exhibits an insulator-metal transition. The saturated magnetic moment is close to the calculated value based on the theory of localized spin moments. A metallic behavior is observed below the Curie temperature and in the paramagnetic regime a thermally activated polaron transport takes place [29]. In the metallic regime there is still a strong Hund's rule coupling between the now itinerant e_g electrons (or holes) which are hybridized strongly with the oxygen $2p$ states and the localized t_{2g} spins which can be viewed as a single local spin. The interplay between the configuration of the local spin and the dynamics of the e_g carriers governs the electronic properties including the temperature and magnetic field dependent metal-nonmetal phenomena. There is a competition between ferromagnetism with metallic behavior and cooperative Jahn-Teller effect with charge-ordering, i.e. insulating and antiferromagnetic be-

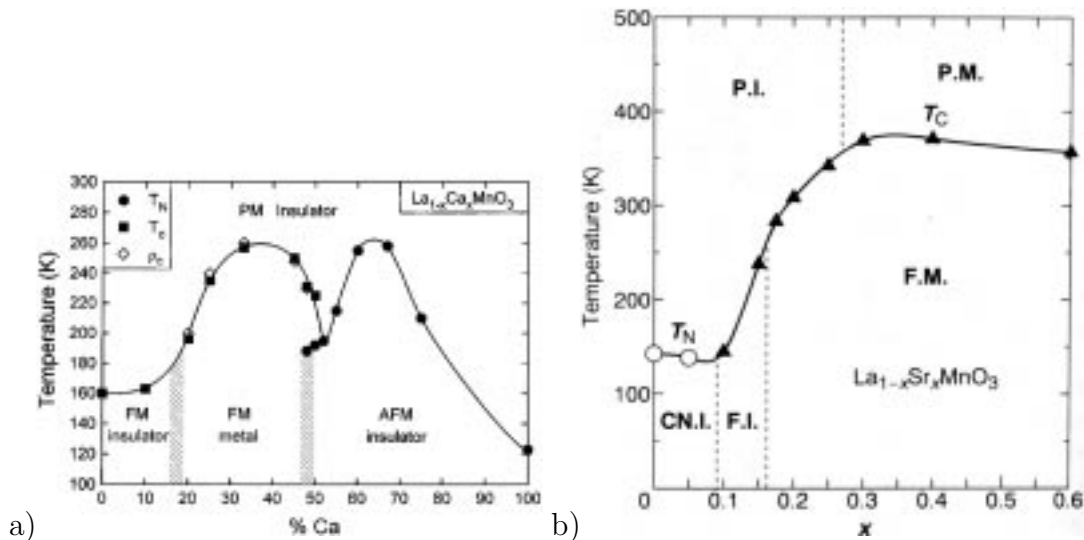
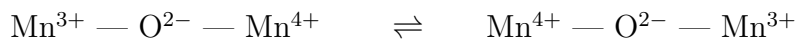


Figure 1.3: Temperature-composition diagram of $\text{La}_{1-x}A_x\text{MnO}_3$ with $A = \text{Ca}$ (a) and $A = \text{Sr}$ (b). PM = paramagnetic, FM = ferromagnetic, AFM = antiferromagnetic, PI = paramagnetic insulator, FI = ferromagnetic insulator, and CN.I. = spin canted insulator. Diagrams are taken from Ref. [25, 30].

havior [31, 32, 33]. Also the end member CaMnO_3 ($x = 1$) is, as its counterpart at the opposite end LaMnO_3 ($x = 0$), an antiferromagnetic insulator. In Fig. 1.3 the temperature-composition diagrams of the solid solutions $\text{La}_{1-x}\text{Ca}_x\text{MnO}_3$ and $\text{La}_{1-x}\text{Sr}_x\text{MnO}_3$ with a large variety of different phases are shown.

1.2.3 Double-exchange

The simultaneous occurrence of itinerant electron behavior and ferromagnetism is explained by the *double-exchange* mechanism introduced by Zener [34]. He considered the problem of the electron exchange between neighboring Mn^{3+} ($d^4, t_{2g}^3 e_g^1$) and Mn^{4+} (d^3, t_{2g}^3) ions via a connecting oxygen ion and introduced the concept of simultaneous transfer (hopping) of an electron from the Mn^{3+} to the oxygen and from the oxygen to the neighboring Mn^{4+} . Such transfer was called double-exchange. Zener assumed that Hund's-rule coupling is strong between the e_g and the t_{2g}^3 electrons and that the carriers do not change their spin orientation when hopping from one ion to the next. The exchange energy is given by $h\nu/2$ where ν is the frequency of oscillation of the electron between two Mn sites resulting in two degenerated configurations:



The lowest energy corresponds to a parallel alignment of the spins of the two adjacent Mn cations. Double-exchange is always ferromagnetic. In the configurations $\text{Mn}^{3+} - \text{O}^{2-} - \text{Mn}^{3+}$ and $\text{Mn}^{4+} - \text{O}^{2-} - \text{Mn}^{4+}$, on the other hand, superexchange is antiferromagnetic. It is dominant in the end members LaMnO_3 and CaMnO_3 , respectively. If the manganese spins are not parallel or if the bond $\text{Mn} - \text{O} - \text{Mn}$ is bent, the electron transfer is reduced and the mobility decreases, e.g. in the insulating orthorhombic compound LaMnO_3 the bond angle is 150° , whereas in the metallic cubic $\text{La}_{0.67}\text{Ca}_{0.33}\text{MnO}_3$ the bond angle is nearly 180° . This relationship will be important in the last chapter discussing the properties of a strongly distorted double-perovskite structure.

Anderson and Hasegawa [35] generalized the double-exchange mechanism by considering interactions between a pair of magnetic ions with general spin directions. The transfer integral t_{ij} between the neighboring sites i and j was calculated to be

$$t_{ij} = t_{ij}^0 \cos\left(\frac{\theta_{ij}}{2}\right), \quad (1.3)$$

where t_{ij}^0 is the normal transfer integral which depends on the spatial wavefunctions and the term $\cos(\theta_{ij}/2)$ results from the spin wavefunction. θ_{ij} is the angle between the two (classical) spins of the involved cations. This angle-dependence of the transfer integral is different to the superexchange where the coupling is proportional to $\cos(\theta_{ij})$.

It follows that there is a direct connection between conductivity and ferromagnetism which is responsible for the colossal magnetoresistance. A very intuitive scenario is given in the following. The ferromagnetic metallic state is stabilized by maximizing the kinetic energy of the conduction electrons ($\theta_{ij} = 0$). When temperature is raised up to near or above T_C , the configuration of the spins is dynamically disordered and accordingly the effective hopping interaction is also the subject to disorder. It is reduced on average. This leads to an enhancement of the resistivity near T_C towards an insulating behavior. Therefore, the large MR can be expected around the Curie temperature, since the local spins are easily aligned by an external field and hence the average angle θ_{ij} is reduced leading to metallic transport.

The theory of the double-exchange mechanism was generalized by several research groups taking into account magnetic polarons and local lattice distortions [36, 37, 38]. The occurrence of metallic behavior together with ferrimagnetism in the double-perovskites will be discussed in the framework of a double-exchange-like mechanism in the fourth chapter.

1.3 Spin polarized transport

A normal metal such as Cu has in zero field the same number of occupied states with spin up and spin down. Therefore, it has no net moment and the densities of states for spin up and spin down electrons at the Fermi level are equal, i.e. the material is unpolarized. On the other hand, in a ferromagnetic material, such as Fe, Co, or Ni, the exchange energy lifts the degeneracy of the spin up and spin down states. The conduction band is split into majority and minority carrier bands. Therefore, a spin imbalance of the occupied spin up and spin down states results, i.e. the material has a net magnetic moment. Further, the spin up and spin down densities of states at the Fermi energy could become different and a so called spin polarization arises which is important for the transport measurements discussed in this work. The value of the spin polarization for electron transport P depends on the extent to which the conduction bands cross the Fermi surface and is here defined as

$$P \equiv \frac{N_{\uparrow}(E_F) - N_{\downarrow}(E_F)}{N_{\uparrow}(E_F) + N_{\downarrow}(E_F)}, \quad (1.4)$$

where $N_{\sigma}(E_F)$ with $\sigma = \uparrow, \downarrow$ are the spin dependent densities of states at the Fermi level for electrons with spin σ . A typical ferromagnet such as Ni has a wide conduction band and a small exchange energy which results in a partial polarization of 11% at the Fermi level [39, 40]. Magnetic materials with a complete spin polarization, i.e. only for one spin direction states exist at the Fermi level, are termed half-metallic. In Fig. 1.4 the densities of states for Ni and $\text{La}_{0.67}\text{Sr}_{0.33}\text{MnO}_3$ are

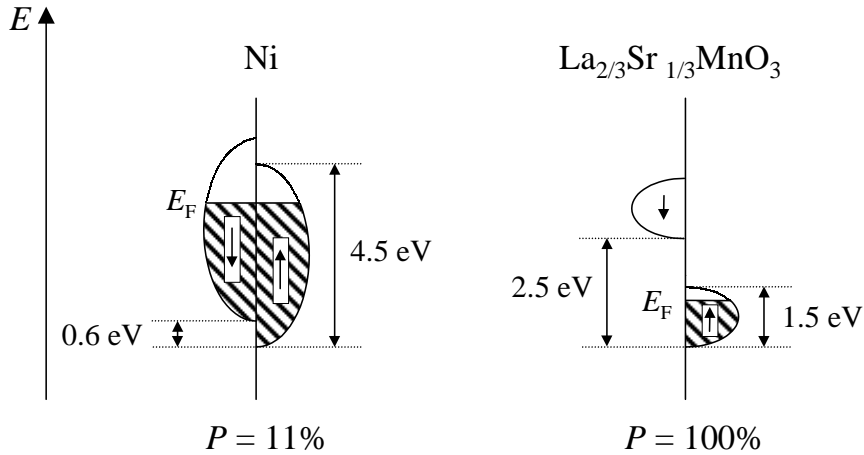


Figure 1.4: Schematic energy level diagram for Ni and $La_{0.67}Sr_{0.33}MnO_3$ [39, 41].

shown schematically. $La_{0.67}Ca_{0.33}MnO_3$ and $La_{0.67}Sr_{0.33}MnO_3$ are due to the narrow conduction band and the large exchange energy close to a true half-metallic ground state [41, 42]. Pickett and Singh calculated that the material is not fully half-metallic, i.e. a small number of minority charge-carriers is still present [43]. A number of experimental techniques as spin resolved photoemission measurements [44] and ferromagnet-superconductor tunnel junction techniques [45, 46], have been exploited to measure the degree of spin polarization. A further method to determine the high spin polarization degree with a ‘ferromagnet-insulator-ferromagnet tunnel junction’ is described in the third chapter. With such devices one can obtain large MR in magnetic field ranges of millitesla. This is of great technological importance, e.g. for read-heads in hard disk drives. Further, the possibility to have a source of spin polarized carriers enables the development of *spin electronics*.

1.4 Hall effect in ferromagnetic materials

The occurrence of a transverse resistivity ρ_{xy} in cubic materials requires a symmetry breaking field, which is in Hall effect measurements the magnetic induction B . The moving electrons in a conductor with charge e and velocity \vec{v} are deflected due to the Lorentz force $-e(\vec{v} \times \vec{B})$ and a Hall voltage is built up perpendicular to the current and magnetic field direction [47]. In ferromagnetic materials it is well known that the magnetization M of the sample is as well symmetry breaking. The transverse resistivity is generally given by

$$\rho_{xy} = V_{\text{Hall}}t/I = R_H B + R_A \mu_0 M \quad (1.5)$$

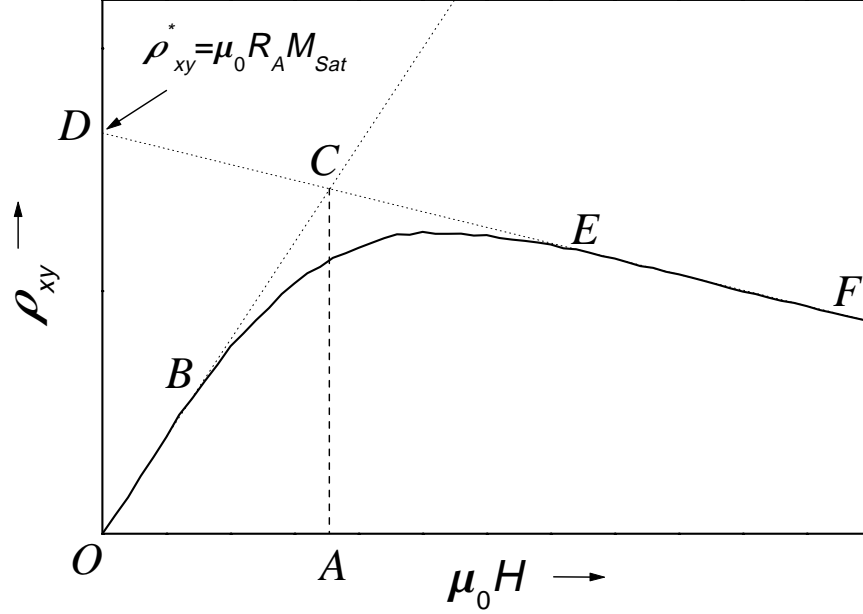


Figure 1.5: Schematic view of the Hall voltage as a function of external magnetic field for a ferromagnet. A holelike (electronlike) anomalous (ordinary) Hall effect is sketched. From the linear slope $E-F$ at high magnetic fields one determines the ordinary Hall coefficient R_H . From the axis intercept of the linear slope $E-F$ at $\mu_0H = 0$ (point D) the anomalous Hall coefficient R_A is calculated.

with the Hall voltage V_{Hall} , the film thickness t , the applied current I , the ordinary Hall coefficient R_H , and the anomalous Hall coefficient R_A [48, 49]. The first term on the right side of Eq. 1.5 is called the ordinary Hall effect and the second term is known as the anomalous (sometimes also called extraordinary or spontaneous) Hall effect.

In the case of a ferromagnet the magnetic induction B is influenced by the internal magnetic field H_{int} and the magnetization M : $B = \mu_0(H_{\text{int}} + M)$. Further, the internal magnetic field H_{int} is reduced in comparison to the external magnetic field H due to the demagnetization factor N [50]: $H_{\text{int}} = H - NM$. Hence, Eq. 1.5 changes to

$$\rho_{xy} = R_H \mu_0 [H + (1 - N)M] + R_A \mu_0 M, \quad (1.6)$$

i.e. the magnetization contributes to the ordinary and the anomalous Hall effect [51, 52]. For the thin film geometry used for Hall effect measurements (normal vector of film plane \parallel magnetic field vector) N is close to unity and therefore the contribution of the magnetization to the ordinary Hall effect can be neglected.

A typical measured Hall voltage as a function of magnetic field is shown schematically in Fig. 1.5. In high magnetic fields at magnetic saturation, it is obvious from Eq. 1.5 that the second term on the right side is constant. Therefore, a linear field dependence between the points E and F due to the ordinary Hall

effect is visible. In this field region the first term of Eq. 1.5 controls the field dependence of ρ_{xy} . The linear slope (here negative) is equal to the ordinary Hall coefficient. The electronlike charge-carrier concentration n can be determined in a one band model by

$$n = \frac{1}{R_H q}, \quad (1.7)$$

with the charge $q = -e$ in this case. Together with the longitudinal resistivity ρ_{xx} , the mobility μ of the charge-carriers can be evaluated:

$$\mu = \frac{1}{qn\rho_{xx}}. \quad (1.8)$$

The origin of the linear increase of the Hall resistivity in low fields is the increasing magnetization component perpendicular to the thin film plane. In this field region the second term of Eq. 1.5 dominates the field dependence of ρ_{xy} . The anomalous Hall coefficient can be extracted from the data by extrapolation of the linear high-field data to the ordinate axis at $B = 0$ (point D). The obtained value (here positive) is then, according to Eq. 1.5,

$$\rho_{xy}^* := R_A \mu_0 M_{\text{Sat}}, \quad (1.9)$$

with M_{Sat} the saturated magnetic moment. The absolute value of R_A is frequently more than two orders of magnitude larger than R_H . In ferromagnetic materials the anomalous Hall effect has two possible origins, an unsymmetry of scattering (skew scattering) or a sideward displacement of the center of weight of an electron wave packet during the scattering process (side-jump), both due to spin orbit interaction [53]. The anomalous Hall effect is closely related to the longitudinal resistivity ρ_{xx} by

$$R_A \mu_0 M_{\text{Sat}} = \gamma \rho_{xx}^n, \quad (1.10)$$

but with a different exponent $n = 1$ and $n = 2$ for skew scattering and side jump, respectively.

Mixed-valence manganites are delicate materials for Hall effect measurements. Experimental problems arise mainly from two reasons. The first difficulty is to achieve a complete magnetic saturation in order to evaluate the ordinary Hall effect. Because of the large MR a second problem forms. Any imbalance in the Hall leads produces a field dependent ρ_{xx} signal which may mask the Hall contribution. Hence, very high magnetic fields and a special circuit configuration, described in the following chapter, were used. This work is focused on the analysis of the ordinary Hall effect. The anomalous Hall effect was discussed in detail in the Master thesis of the author [29].

1.5 X-ray and neutron scattering

It is well known that the most general methods for investigating the spatial structure of solids are based on diffraction phenomena using X-rays, electrons, and thermal neutrons with characteristic wavelengths comparable with interatomic distances. Elastic scattering is of great importance in various branches of science and technology, including solid state physics, molecular biology and biophysics, polymer science, and metallurgy.

1.5.1 X-ray diffraction

The scattering of X-rays by matter is dominated by the interaction of incident radiation with electrons. A contribution from nuclear scattering is negligible in that the mass of nuclei is more than 10^3 times larger than the electron mass and the nuclear scattering energy is accordingly 10^6 times less than the electron scattering energy.

X-rays are produced when fast electrons hit on matter, e.g. a Cu target. Deceleration of the electron by the electric fields in the solid gives rise to emitted X-rays of continuously varying wavelength (bremsstrahlung). In practice another kind of process is exploited. The electron kicks out an inner shell electron from the Cu and the remaining hole can be filled by an electron from a higher shell, thereby emitting an X-ray photon. The highest intensity is obtained for the transition from the L shell to the K shell, the so called $K\alpha$ transition. Due to spin orbit interaction this line is split into two lines, $K\alpha_1$ and $K\alpha_2$, which can be resolved in the diffraction experiment. To fade out the bremsstrahlung spectrum and further transition lines ($K\beta$) a monochromatizing crystal, e.g. graphite is often used.

The interaction of incident X-ray radiation with the electrons in the crystal is accompanied by a change in the wave vector $\vec{q} = \vec{k} - \vec{k}'$, called the scattering vector with incident and outgoing wave vector \vec{k} and \vec{k}' , respectively. The total scattered amplitude by an atom consisting of Z electrons is given by the atomic scattering factor (also called atomic form factor)

$$f_0(\vec{q}) = \sum_{l=1}^Z \int \rho_l(\vec{r}) \exp(i\vec{q}\vec{r}) d\vec{r} \quad (1.11)$$

with \vec{r} the position vector and $\rho(\vec{r})$ the electron density. For a spherical symmetry f_0 depends only on the magnitude of the scattering vector $q = 4\pi \sin(\theta)/\lambda$ with λ the wavelength and θ the angle of incidence.

If a crystal, consisting of S unit cells with position vectors \vec{R}_i , is a Bravais lattice with a basis, then to each lattice point corresponds a group of atoms ($j = 1, \dots, N$) located at positions \vec{r}_j in the space of the unit cell. The total

amplitude of scattered X-rays results from a superposition of the S unit cells and the N different atoms in each unit cell

$$F(\vec{q}) = \sum_{i,j=1}^{S,N} f_{0i,j}(\vec{q}) \exp\left(i\vec{q}(\vec{R}_i + \vec{r}_j)\right). \quad (1.12)$$

The amplitude $F(\vec{q})$ is called the structure factor of the basis.

For an infinite scattering volume the only significant contributions to the right side in Eq. 1.12 arise when the change in wave vector \vec{q} is a vector of the reciprocal lattice \vec{G} . This condition is named the Laue condition after Max von Laue [54, 55].

The measurable quantity is the intensity $I(\vec{q})$ which is given by the square of the modulus of the amplitude of the structure factor:

$$I(\vec{q}) = |F(\vec{q})|^2. \quad (1.13)$$

Several corrections for the structure factor have to be taken into account. It is calculated for stationary atoms, i.e. vibrations have to be regarded by the Debye-Waller factor as discussed in the last chapter [56]. Further corrections are the Lorentz factor and polarization factor considering the beam divergence and the polarization, respectively [57].

For a spherosymmetric distribution of the electrons around the center of the atom j one obtains for the atomic scattering factor f_j as a function of the magnitude of the scattering vector

$$f_j(q) = 4\pi \int_{r=0}^{\infty} \rho(r) r^2 \frac{\sin(qr)}{r} dr \stackrel{q=0}{\equiv} Z. \quad (1.14)$$

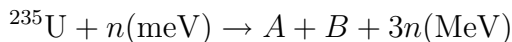
In the limit $q \rightarrow 0$, i.e. $\theta \rightarrow 0$, the atomic scattering factor f_j is equal to the number of electrons in the respective atom and for large $q > r_a$ it decreases strongly due to the finite radial extent r_a of the electron shell, which is a restriction in the experiment. Values for f_j are tabulated in Ref. [58]. Eq. 1.14 reveals a second disadvantage of X-rays when investigating oxides. The intensities of the oxygen atoms ($Z = 8$) are masked by the heavy cation ions incorporated in the perovskite structure, e.g. in the investigated compounds La ($Z = 57$), Mo ($Z = 42$), and Re ($Z = 75$). Using thermal neutrons one can surmount this problem as shown in the following.

1.5.2 Neutron diffraction

Contrary to X-rays, neutrons interact mainly with the nuclei because of the strong interaction. Due to the magnetic dipole moment, a neutron interacts as well with the magnetic moment of the unpaired electrons. The wavelength of neutrons is

given by the well-known de Broglie relation $\lambda = h/mv$. To investigate crystals thermal neutron energies of 10 meV – 100 meV are required.

Free neutrons can be produced in nuclear reactors. The typical nuclear reaction is the nuclear fission of an uranium nucleus by a thermal neutron.



Two nuclear fragments A and B and three epithermal neutrons are produced. The high energy neutrons were thermalized through a moderator (heavy water) and can then initiate further nuclear fissions (chain reaction). One neutron source is the high-flux reactor at the ILL (Institute Laue Langevin) in Grenoble with a thermal power of 58 MW. The thermal neutron flux has a Maxwellian distribution with a peak at 1.2 Å.

Consider a neutron with wave vector k that scatters elastically at an atomic nucleus. The wave function $\Psi(r, \theta, \phi)$ of the neutron in polar coordinates at a large distance of the scattering center is given by

$$\Psi(r, \theta, \phi) = A \left[\exp(ikz) + f(\theta, \phi) \frac{\exp(ikr)}{r} \right] \quad (1.15)$$

with A a normalizing factor and $f(\theta, \phi)$ the scattering amplitude (first Born approximation or kinematic approximation). The first term in Eq. 1.15 is the incident plane wave and the second term is the scattered spherical wave. The wavelength of thermal neutrons is large compared with the range of the nuclear forces and therefore, the scattering amplitude is a constant $f(\theta, \phi) = -b$. It is called the coherent scattering length and plays the same role as the atomic scattering factor for X-rays times a characteristic length, the classical Thomson electron radius $r_0 = e^2/m_e c^2 \approx 2.82 \times 10^{-15}$ m. The scattering intensity of the N different atoms in the unit cell, called the differential cross section $d\sigma/d\Omega$, is expressed by

$$\frac{d\sigma}{d\Omega} = |F(\vec{q})|^2 = \left| \sum_{j=1}^N b_j \exp(i\vec{q}\vec{r}_j) \right|^2 \quad (1.16)$$

with $d\Omega$ the solid angle. As in the case of X-rays corrections due to the Debye-Waller factor have to be taken into account [59]. The advantage of neutron scattering over X-rays is that the scattering length b_j in contrast to the atomic scattering factor f_j does not depend on the glancing angle θ , i.e. one has high intensities even at high angles whereas the atomic scattering factor decreases strongly with increasing glancing angle in X-ray experiments. A further advantage is that b depends on the details of the nuclear potential, i.e. one has a nonmonotonic dependence of b_j on the atomic number, light and heavy atoms have comparable scattering lengths around $\pm 5 \times 10^{-15}$ m [60]. Therefore, the oxygen positions in perovskites can be identified by neutron diffraction.

The elastic magnetic scattering of thermal neutrons has been used in two fields. First, the determination of magnetic structures, i.e. the location and orientation of unpaired spins in crystal structures, and second, to gain information on the properties of the unpaired spin by measuring magnetic form factors. Due to the magnetic dipole moment, a neutron can interact with the magnetic field in solids. The scattering lengths of the strong interaction and the dipole-dipole interaction are comparable and therefore neutrons are ideal sondes to investigate magnetic oxides. As for the atomic form factor the magnetic form factor decreases rapidly with increasing q because of the finite size of the electron shells involved [61, 62]. The magnetic scattering is negligible for all except the first few Bragg peaks. For a detailed discussion see Ref. [63, 64].

The neutron diffraction measurements were performed at the high-resolution two-axis diffractometer D2B situated in the reactor hall of the ILL [65, 66]. The instrument is characterized by the very high take-off angle (135°) for the monochromator consisting of 28 Ge (115) crystals of $1 \times 5 \times 1 \text{ cm}^3$. In the experiment, a neutron beam with a wavelength of 1.594 \AA using the Ge (551) reflection is used. At the sample the beam size is $2 \times 5 \text{ cm}^2$. After 100 steps of 0.025° in 2θ a complete diffraction pattern is obtained, since the 64 detectors (^3He counting tubes [67]) are spaced at 2.5° intervals. A whole scan takes typically only 30 minutes. To improve statistics the scan is repeated several times.

1.5.3 Rietveld refinement

The whole pattern of powdered or polycrystalline samples can be analyzed by a profile-refinement technique first described by Rietveld [68, 69]. This method is used when the main features of a structure are already known, i.e. a reasonably good starting model is needed. Therefore, the first step is the determination of the reflection positions $2\theta_i$ with corresponding intensities and the respective lattice plane distances d_i . With a comparison of the reflection list including relative intensities with lists from known structures the reflections are indexed ($d_i \rightarrow d_{hkl}$). After this qualitative phase analysis the crystal symmetry system is fixed and a quantitative phase analysis with the Rietveld method follows.

In this computer-based analytical procedure least-squares refinements [70] are carried out until the best fit is obtained between the entire observed powder diffraction pattern taken as a whole and the entire calculated pattern based on the *simultaneously* refined models for the crystal structure(s), diffraction optics effects, instrumental factors, and other specimen characteristics (e.g. lattice parameters). A key feature is the feedback, during refinement, between improving knowledge of the structure and improving allocation of observed intensity or partially overlapping individual Bragg reflections. The quantity minimized in the

least-squares refinement is

$$S = \sum_i \frac{(y_i(\text{obs}) - y_i(\text{calc}))^2}{y_i(\text{obs})} \quad (1.17)$$

where $y_i(\text{obs})$ ($y_i(\text{calc})$) is the observed (calculated) intensity at the i th step of the pattern and the sum is overall data points. The calculated intensities are determined from the absolute values of the square of the structure factor $|F_K|^2$ computed from the structural model by summing of the calculated contributions from neighboring Bragg reflections plus the background:

$$y_i(\text{calc}) = s \sum_K L_K |F_K|^2 \phi(2\theta_i - 2\theta_K) P_K A + y_i(\text{bg}) \quad (1.18)$$

where s is the scale factor, K the Miller indices, L_K contains the Lorentz, polarization, and multiplicity factors, ϕ is the reflection profile function, P_K the preferred orientation function, A is an absorption factor, and $y_i(\text{bg})$ is the background intensity at the i th step (see appendix for details). Multiple phases may be refined simultaneously and comparative analysis of the separate overall scale factors for the phases offers what is probably the most reliable current method for doing quantitative phase analysis. Further details of the least-squares procedures are presented in Ref. [71].

The X-ray and neutron diffraction patterns of $\text{Ca}_2\text{FeReO}_6$ were analyzed with the program FULLPROF developed by Rodríguez-Carvajal [72]. In the fifth chapter the results are presented. The input file for the program FULLPROF with all refinable parameters is described in the appendix.

Chapter 2

Ca- and Sr-doped epitaxially grown manganite thin films

An external magnetic field reduces spin disorder in a ferromagnet most effectively in the neighborhood of the Curie temperature T_C . In manganites the resistivity is metallic with a positive temperature coefficient below T_C . Above T_C , a change to a thermally activated behavior is observed for the Ca-doped compound. The temperature value of the resistivity anomaly, marking a metal-insulator transition, is nearby the Curie temperature. The suppression of this anomaly in resistivity at T_C with an external magnetic field leads to the colossal magnetoresistance (CMR). At low temperatures in the ferromagnetically ordered phase and at high temperatures in the paramagnetic regime the large MR effect is diminished. Epitaxial thin films of $\text{La}_{1-x}\text{Ca}_x\text{MnO}_3$ were studied in detail previously by the author and several coworkers [29, 73, 74], but Curie temperatures below room temperature prevent the application of these compounds in sensor technology. The highest Curie temperatures in the solid solution $\text{La}_{1-x}\text{Ca}_x\text{MnO}_3$ were obtained with $x = 0.33$ (see Fig. 1.3a). By changing the dopant atom from Ca to Sr, T_C can be shifted above room temperature. In the Sr-doped sample $\text{La}_{1-x}\text{Sr}_x\text{MnO}_3$ the highest value of T_C was found as well for $x = 0.33$ (see Fig. 1.3b).

Therefore, in order to have higher intrinsic CMR at ambient temperature, the first goal of this work was to increase T_C in epitaxial manganite thin films close to room temperature using Sr instead of Ca doping. In this chapter the results of the preparation, characterization and transport properties including Hall effect for epitaxial $\text{La}_{0.67}\text{Sr}_{0.33}\text{MnO}_3$ thin films in comparison with epitaxial $\text{La}_{0.67}\text{Ca}_{0.33}\text{MnO}_3$ thin films are presented. For both compounds a holelike charge-carrier density of more than one electron per unit cell was found. In low magnetic fields or at high temperatures, an anomalous electronlike contribution dominates the Hall voltage. Due to the application of high magnetic fields up to 20 T, a general charge-carrier density collapse at the Curie temperature in manganites could be revealed.

2.1 Preparation and characterization

Thin films of $\text{La}_{0.67}\text{Sr}_{0.33}\text{MnO}_3$ were prepared using pulsed laser deposition (PLD). In PLD a beam from a pulsed laser¹, typically a KrF excimer laser operating in the ultraviolet at $\lambda = 248$ nm is focused through a window onto a ceramic target with the required composition mounted in a vacuum chamber. A frequency-tripled or quadrupled neodymium-doped yttrium aluminium garnet (Nd:YAG) laser may also be used in off-axis geometry [75]. The oxygen partial pressure in the preparation chamber during deposition is around 10 Pa. To obtain a homogeneous ablation, the target rotates and in addition the laser scans a limited area on the target. Due to the high energy density per pulse of about 2 J/cm^2 a plasma is created which takes the form of a plume that is several centimetres long, emerging normal to the surface of the target. The particles in the plasma are collected onto a heated substrate and the thin film is built up. The procedure and the experimental setup (on-axis geometry) used here is described in detail elsewhere [76, 77].

As substrates (100) SrTiO_3 and (100) LSAT $[(\text{LaAlO}_3)_{0.3} - (\text{Sr}_2\text{AlTaO}_6)_{0.7}$ untwinned] insulating perovskites were used. The LSAT substrates with a lattice constant of $a_0 = 3.868 \text{ \AA}$ have a smaller lattice mismatch to the Sr-doped films with 3.847 \AA compared to the SrTiO_3 substrates with $a_0 = 3.905 \text{ \AA}$. The optimized deposition conditions are a substrate temperature of 950°C in an oxygen partial pressure of 14 Pa and annealing after deposition at 900°C for 1 h in an oxygen partial pressure of 600 hPa for full oxygen loading. The deposition rate was 0.3 \AA/pulse with a pulse frequency of 3 Hz. In the appendix the parameters for target and thin film preparation are listed.

Epitaxial thin films of $\text{La}_{0.67}\text{Ca}_{0.33}\text{MnO}_3$ were deposited by magnetron sputtering. This preparation procedure is based on an experience several years old gained with high-temperature superconductors in the research group [78]. In a vacuum chamber one has a high negative potential of several hundred volts on a stoichiometric target (cathode) against a heated substrate (anode). The target surface is bombarded by ions of the filling gas in the chamber, which is in the most cases argon with a partial pressure of 0.1 Pa – 10 Pa. A permanent plasma is created because of the avalanche effect. Through the field accelerated electrons create in collisions more and more new argon ions which are accelerated towards the target. Due to collisions of the argon ions with the target surface atoms are emitted. They condense on the heated substrate and form the thin film. Preparation and characterization is described in Ref. [29].

By scanning electron and scanning force microscopy a homogeneous surface composition was found. The film thicknesses of around 270 nm were determined by a Mireau interferometer.

¹Lambda Physik COMPEX301.

With X-ray diffraction in Bragg-Brentano geometry, only film reflections corresponding to a $(l00)$ orientation of the cubic perovskite cell are visible for both compounds. A $\theta/2\theta$ -scan is shown in Fig. 2.1. The $\text{La}_{0.67}\text{Sr}_{0.33}\text{MnO}_3$ (400) re-

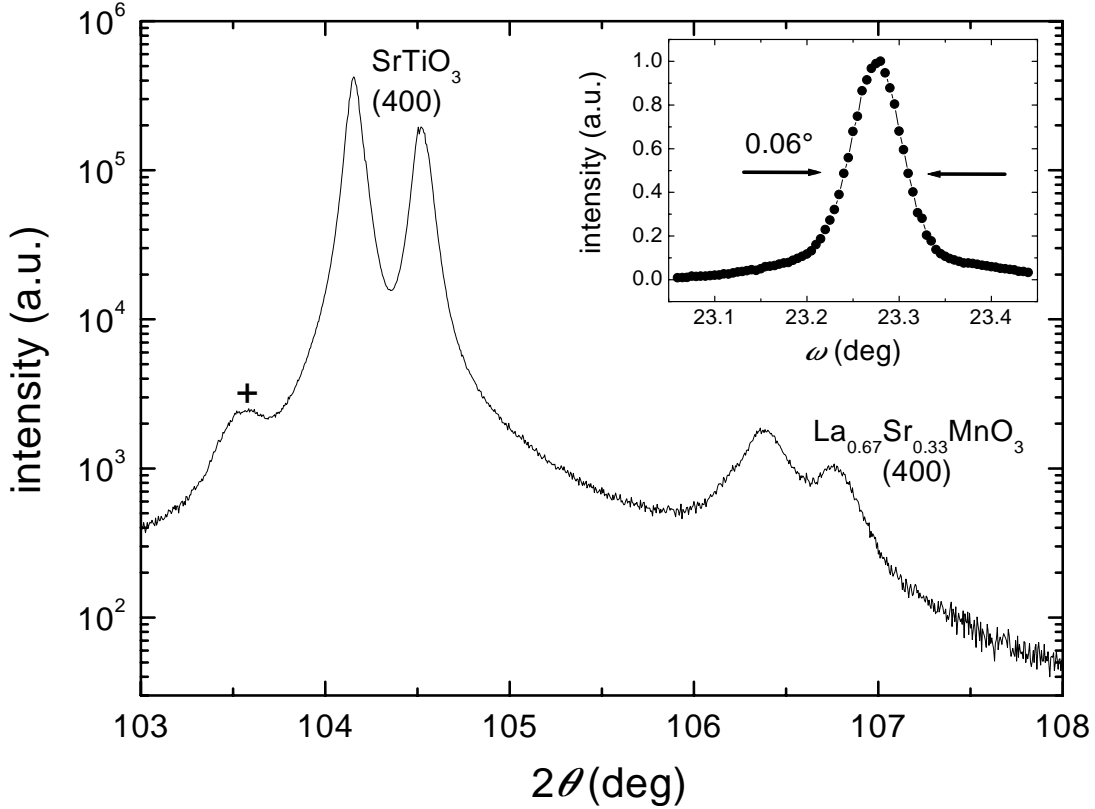


Figure 2.1: $\theta/2\theta$ -scan of the $\text{La}_{0.67}\text{Sr}_{0.33}\text{MnO}_3$ thin film showing the (400) reflection (Cu $K\alpha$ doublet). In the inset the narrow rocking curve of the (200) ($2\theta = 47.21^\circ$) reflection is shown. The cross marks a peak generated by the X-ray source (see text).

flexion is visible in the neighborhood of the SrTiO_3 (400) reflection peak. Both reflections are doubled due to the $K\alpha_1$ and $K\alpha_2$ transitions in Cu with wavelengths of $1.5405952(13)$ Å [79] and $1.5444256(19)$ Å [80], respectively. Just below the $K\alpha_1$ reflection of the substrate a satellite line is present (marked by ‘+’) which can be seen also in $\theta/2\theta$ -scans of other compounds investigated in this thesis (see Fig. 3.1 and Fig. 4.3). The origin of this faint peak are single electron jumps (together five transitions: α' , α_3 , α_4 , α_5 , and α_6) in doubly ionized Cu atoms, i.e. one electron missing in the K shell and one electron missing in the L shell [81, 82]. Due to the low resolution of the used two-axis X-ray diffractometer, the five satellite transition lines are unresolved [83]. All transitions are listed in the Table 2.1 [84].

Rocking angle analysis shows epitaxial $(l00)$ axis oriented growth with an angular spread smaller than 0.06° as presented in the inset of Fig. 2.1. With

Table 2.1: X-ray transitions in ionized Cu. A Russel-Saunders coupling is assumed for the doubly ionized atom [81].

	Transition	Initial state		Final state
Cu ¹⁺	$\alpha 1$	$(1s)^1(2s)^2(2p)^6$	$^2S \rightarrow$	$(1s)^2(2s)^2(2p)^5$ $^2P_{3/2}$
	$\alpha 2$	$(1s)^1(2s)^2(2p)^6$	$^2S \rightarrow$	$(1s)^2(2s)^2(2p)^5$ $^2P_{1/2}$
	α'	$(1s)^1(2s)^1(2p)^6$	$^1S \rightarrow$	$(1s)^2(2s)^1(2p)^5$ 1P
Cu ²⁺	$\alpha 4$	$(1s)^1(2s)^1(2p)^6$	$^3S \rightarrow$	$(1s)^2(2s)^1(2p)^5$ 3P
	$\alpha 3$	$(1s)^1(2s)^2(2p)^5$	$^3P \rightarrow$	$(1s)^2(2s)^2(2p)^4$ 3P
	$\alpha 5$	$(1s)^1(2s)^2(2p)^5$	$^1P \rightarrow$	$(1s)^2(2s)^2(2p)^4$ 1S
	$\alpha 6$	$(1s)^1(2s)^2(2p)^5$	$^1P \rightarrow$	$(1s)^2(2s)^2(2p)^4$ 1D

ϕ -scans of the {310} reflections the in-plane orientation was studied. The cubic perovskite axes of the films are parallel to that of the substrates with an angular spread smaller than 1°. The temperature dependence of the unit cell volume of the La_{0.67}Ca_{0.33}MnO₃ sample was determined by measuring the in- and out-of-plane lattice constants using a helium flow cryostat with beryllium windows on a four-axis X-ray diffractometer [85].

The samples were patterned with a standard photolithographic process and wet chemically etched to a 3 mm wide and 8 mm long Hall bar structure [29].

For measuring in the temperature regime from 2 K up to room temperature a ⁴He bath cryostat with a 15 T superconducting solenoid from Oxford Instruments was used. The temperature regulation was obtained with a variable temperature insert (VTI). Helium gas streams through a needle valve from the liquid helium reservoir into the insulated inner chamber where the sample is mounted. The constant gas flow passing the sample can be heated and therewith the temperature of the sample can be regulated. To have a faster and better temperature constance, a second heater was mounted on the sample-holder. The measuring arrangement and process is described in Ref. [86].

Magnetotransport measurements above 270 K were carried out using two pieces of equipment, both with room temperature access to the magnetic field. With a cryostat containing a superconducting split-coil from Magnex Scientific, measurements in magnetic fields up to 8 T were performed. To investigate the samples in even higher magnetic fields up to 20 T, a Bitter type magnet was used. It is situated in the High Field Magnet Laboratory at the University of Nijmegen. The Bitter type magnet consists of two concentric electrical coils in form of alternating metallic and insulating plates (Bitter plates) which are powered by a 6000 kW power supply (20 kA, 300 V) as shown in Fig. 2.2. The resistive magnet is cooled by deionized water of 10°C at a flow of 300 m³/h and an inlet pressure of 120 kPa. The cooling water is pumped in axial direction through the small

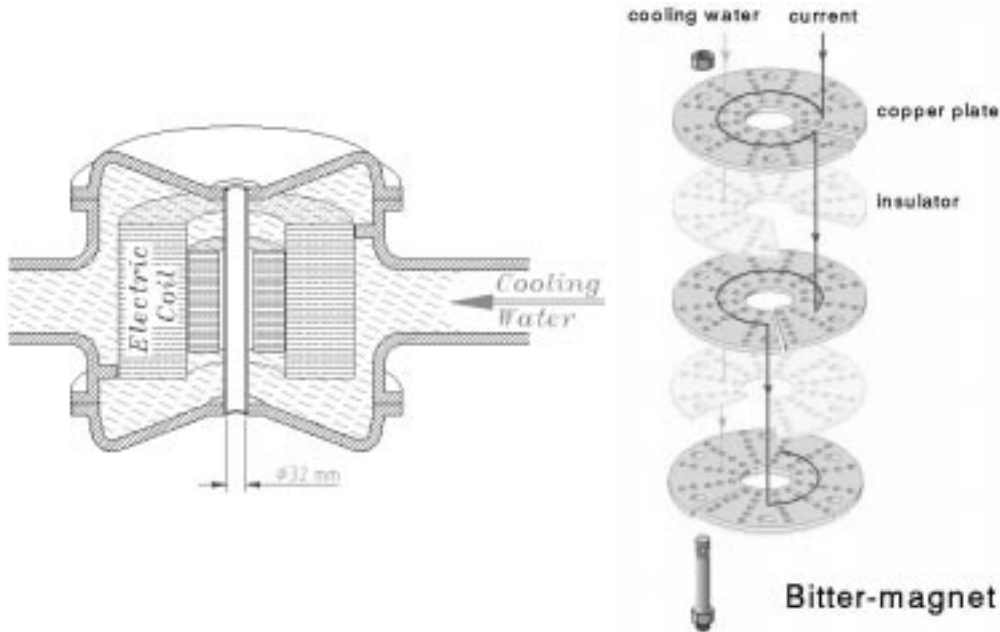


Figure 2.2: *Bitter type magnet* [87].

holes in the bitter plates of the coils, which line up exactly in every plate.

For measurements from ambient temperature up to 600 K, a small 50 W tube furnace was placed into the respective room temperature accesses. In an ohmic regime with a DC current density $j = 1.23 \times 10^6 \text{ A/m}^2$ (current $I = 1 \text{ mA}$) the measurements were performed using a conventional four-point technique. With a temperature sensor² exhibiting a very low MR, the temperature was stabilized to better than 0.02 K during a magnetic field sweep. A complete hysteresis loop was measured, i.e. the field was increased from zero to maximum, decreased to the negative maximum and again increased to zero. Before starting it was ensured that in zero field the opposite Hall contacts are on an equipotential line. In the case of high-resistive manganites with a resistivity of 0.11 mΩcm – 30 mΩcm a bridge circuit with a current injection along three terminals were used [88]. For low-resistance samples, on the other hand, one utilizes in general a bridge circuit with a voltage measurement along three terminals [89]. The remaining imbalance and thermal voltages were compensated by taking data at reversed field and current directions, respectively. In order to eliminate hysteresis effects in the ferromagnetic state, only the reproducible field sweeps from the positive maximum field down to zero field and the negative minimum field up to zero field were evaluated.

With a S.H.E. SQUID magnetometer ferromagnetic hysteresis loops were taken at fixed temperatures. The temperature dependence of the spontaneous magnetic moment was measured in a small field of $\mu_0 H = 20 \text{ mT}$.

²CernoxTM from Lake Shore.

2.2 Magnetotransport measurements

The measured longitudinal resistivities $\rho_{xx}(T)$ of the Ca- and Sr-doped compounds in zero field (solid lines) and in 8 T (dashed lines) are shown in Fig. 2.3. By arrows the Curie temperatures of both samples are indicated, 232 K for

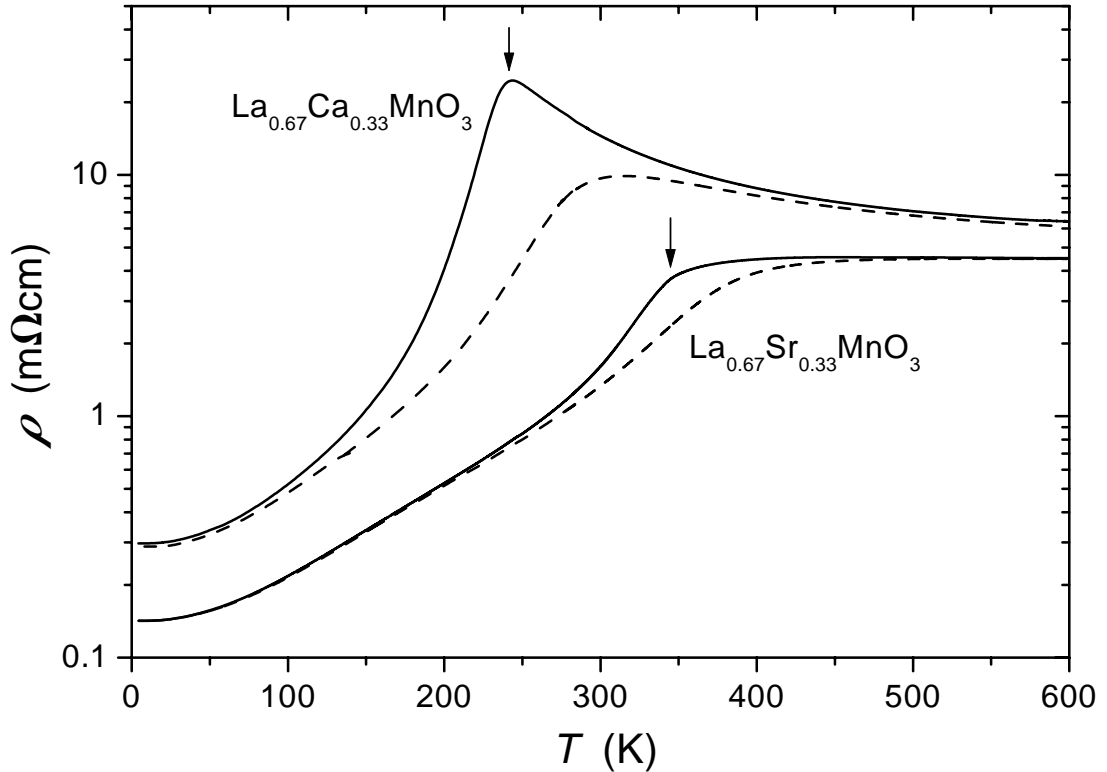


Figure 2.3: Resistivities ρ_{xx} in zero field (solid lines) and in 8 T magnetic field (dashed lines) as functions of temperature. The arrows at 232 K (345 K) indicate the Curie temperatures for $\text{La}_{0.67}\text{Ca}_{0.33}\text{MnO}_3$ ($\text{La}_{0.67}\text{Sr}_{0.33}\text{MnO}_3$).

$\text{La}_{0.67}\text{Ca}_{0.33}\text{MnO}_3$ and 345 K for $\text{La}_{0.67}\text{Sr}_{0.33}\text{MnO}_3$, respectively. For the Ca-doped compound a maximum in resistivity at T_C occurs. At very high and very low temperatures the curves are asymptotic, i.e. the MR diminishes. The resistivity as function of temperature is up to $T/T_C = 0.6$ given by

$$\rho = \rho_0 + \rho_2 T^2 + \rho_{4.5} T^{4.5}. \quad (2.1)$$

The parameters of Eq. 2.1, obtained by fitting the experimental data, are listed in Table 2.2. The quadratic contribution is not changed in presence of a high magnetic field. This was also observed by Snyder *et al.* [90, 91] while Mandal *et al.* [92] found both factors to be magnetic field dependent. One possible origin of a quadratic temperature dependence of the resistivity is the emission and absorption of magnons, but in this case a magnetic field dependence would be expected. Furthermore, in these processes an electron reverses its spin and changes

Table 2.2: Residual resistivities ρ_0 and fitting parameters of Eq. 2.1 for $\text{La}_{0.67}\text{Ca}_{0.33}\text{MnO}_3$ and $\text{La}_{0.67}\text{Sr}_{0.33}\text{MnO}_3$ thin films.

Sample	ρ_0 (m Ω cm)	ρ_2/ρ_0 (10^{-6} K $^{-2}$)	$\rho_{4.5}(0 \text{ T})/\rho_0$ (10^{-11} K $^{-4.5}$)	$\rho_{4.5}(8 \text{ T})/\rho_0$ (10^{-11} K $^{-4.5}$)
$\text{La}_{0.67}\text{Ca}_{0.33}\text{MnO}_3$	0.294	68	256	134
$\text{La}_{0.67}\text{Sr}_{0.33}\text{MnO}_3$	0.139	54	41	36

its momentum. However, in the manganites spin flip processes play no role at low temperatures due to strong spin splitting of the electronic subband states. Therefore, this T^2 -dependent term is attributed to electron-electron scattering in a Fermi liquid. The term proportional to $T^{4.5}$ results from electron-magnon scattering in the double-exchange theory of Kubo and Ohata [93]. In these scattering events the electron spin is conserved, while momentum is exchanged between the electron and magnon system. Its contribution to the resistivity in Eq. 2.1 is proportional to

$$\rho_{4.5} = \frac{3}{32\pi} \frac{\hbar}{e^2 k_F} \frac{1}{S^2} (ak_F)^6 \left(\frac{m}{M}\right)^{4.5} \left(\frac{k_B}{E_F}\right)^{4.5} \left(2.52 + 0.0017 \frac{M}{m}\right) \quad (2.2)$$

with \hbar the Plancks constant, e the charge of a hole, a the lattice constant, $k_F = 0.45\pi/a$ the Fermi wave vector [43], S the spin of a Mn ion, k_B the Boltzmanns constant, $E_F = 1.2$ eV the Fermi energy [43], and M the effective mass of a hole. The effective mass of a spin wave m is defined by $E = \hbar^2 q^2/2m$ with E the spin wave energy and q the wave vector. The strong temperature dependence of this scattering mechanism is partly determined by the number of magnons $\propto T^{3/2}$. In magnetic field this term is suppressed reflecting the increased magnetic order. For manganites a mass ratio of $m/M \approx 1000$ with M the free electron mass results, indicating that the spin wave energy is much lower than the Fermi energy. More direct access than from the resistivity measurements was achieved from neutron scattering [94]. There, a mass ratio of only $m/M \approx 20$ was deduced.

For the Ca-doped compound the transport above T_C is thermally activated [73] and can be described by small polaron hopping [95]. The Sr-doped sample has a slightly lower resistivity and a lower maximal magnetoresistance (MR) at the Curie temperature, because the absolute MR decreases with increasing T_C [96]. Therefore, the sensitivity of the film, i.e. the derivative $d\rho/dB$ at ambient temperature cannot be significantly increased by changing the dopant atom from Ca to Sr. In Fig. 2.4 the magnetic field dependencies of the longitudinal resistivities at $T = 300$ K for $\text{La}_{0.67}\text{Ca}_{0.33}\text{MnO}_3$ and $\text{La}_{0.67}\text{Sr}_{0.33}\text{MnO}_3$ thin film are shown. The different curvature stems from the fact that at room temperature the Ca-doped sample is paramagnetic, whereas the Sr-doped film is still

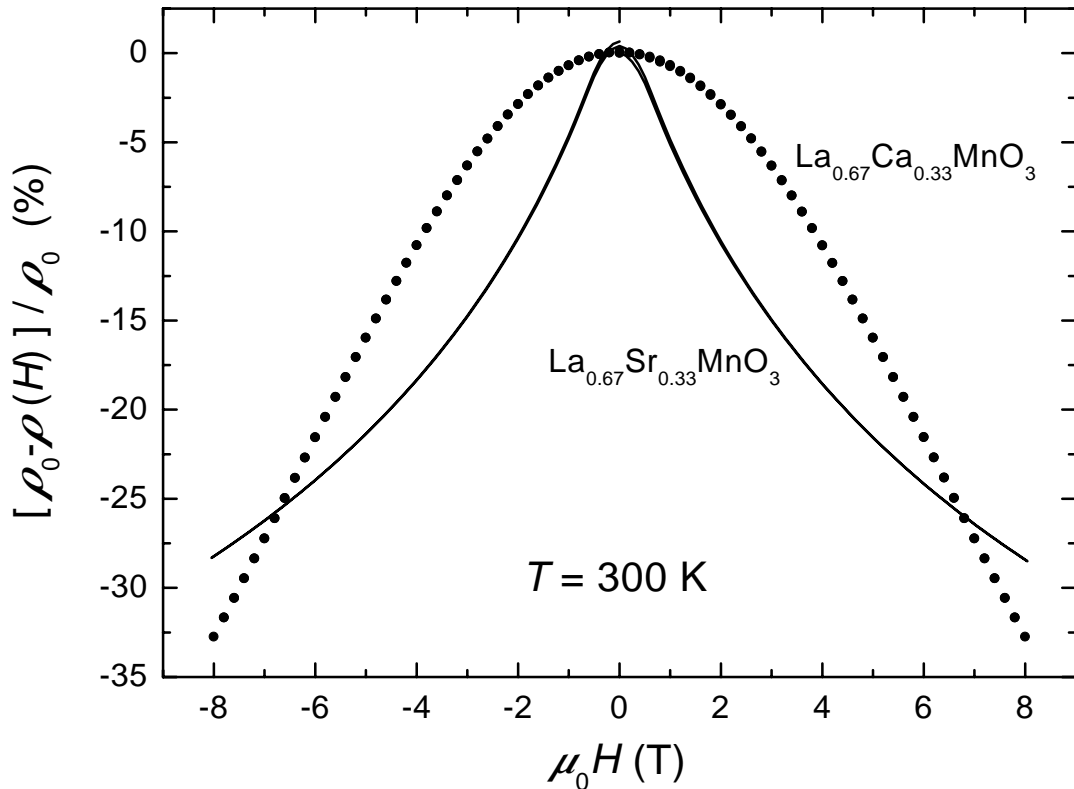


Figure 2.4: High field magnetoresistance of $\text{La}_{0.67}\text{Ca}_{0.33}\text{MnO}_3$ and $\text{La}_{0.67}\text{Sr}_{0.33}\text{MnO}_3$ at temperature $T = 300$ K.

ferromagnetic [90].

Above T_C the resistivity for $\text{La}_{0.67}\text{Sr}_{0.33}\text{MnO}_3$ is described by a crossover between two types of polaron conduction [90, 91]. Scattering of polarons by phonons just above T_C results in a positive $d\rho/dT$, so that in the case of $\text{La}_{0.67}\text{Sr}_{0.33}\text{MnO}_3$ T_C does not coincide with the maximum in resistivity which is less pronounced at $T = 460$ K. The Curie temperature is at a lower value of 345 K (see Fig. 2.3) where an anomaly in the temperature dependence of the resistivity is observed [97].

2.3 Charge-carrier density collapse

The Hall resistivity ρ_{xy} for $\text{La}_{0.67}\text{Sr}_{0.33}\text{MnO}_3$ at different constant temperatures as a function of the external magnetic field H is shown in Fig. 2.5. At low magnetic fields a steep decrease of the Hall voltage V_{Hall} is seen, which is strongest at T_C and becomes less pronounced at low temperatures and above T_C . This part is dominated by the increase in local magnetization with magnetic field. Therefore, the anomalous Hall effect, which is electronlike for manganites, dominates the Hall voltage according to Eq. 1.5 with $R_A > R_H$. At higher fields

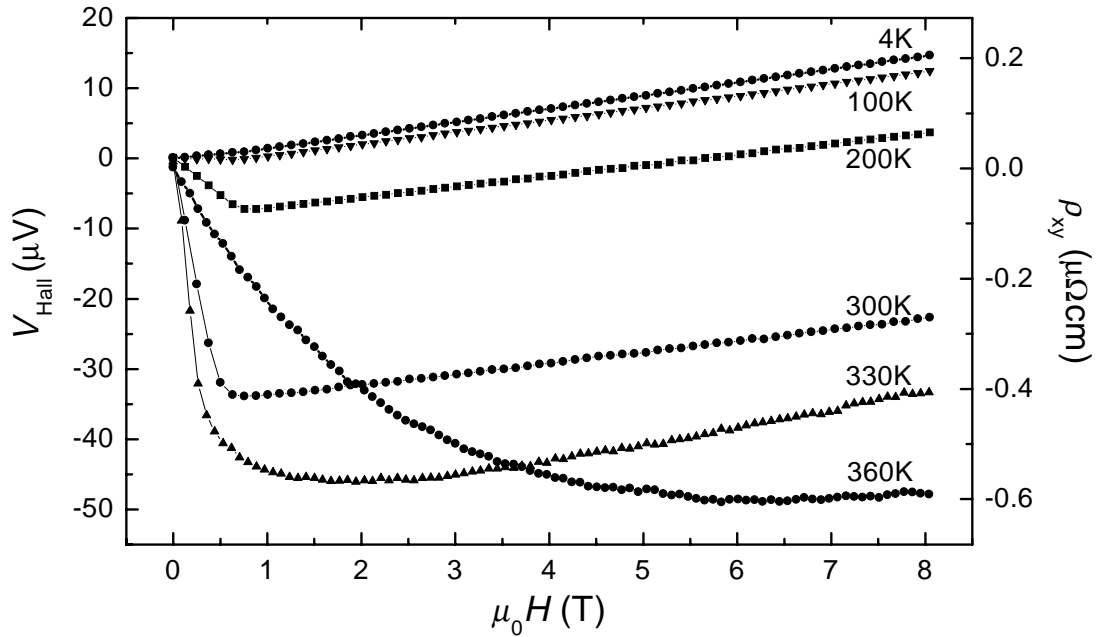


Figure 2.5: The Hall resistivity ρ_{xy} and the Hall voltage V_{Hall} as a function of the external magnetic field at various temperatures for $La_{0.67}Sr_{0.33}MnO_3$.

the magnetization saturates, i.e. the second term in Eq. 1.5 becomes constant. The positive constant slope corresponds to the ordinary Hall constant which is holelike for $La_{0.67}Sr_{0.33}MnO_3$. This behavior is very similar to the Ca-doped compound, if one compares the reduced temperatures T/T_C [29]. The initial slopes $d\rho_{xy}/d(\mu_0H)(H \rightarrow 0)$ are highest at the Curie-temperature for both compounds in agreement with the Berry phase theory of the anomalous Hall effect [98]. The temperature dependence of the electronlike anomalous Hall constant is thermally activated, similar to the longitudinal resistivity and qualitatively consistent with the theory of Friedman and Holstein [99]. This was also observed by Jaime *et al.* [100, 101] and provides another strong evidence of small polarons in manganites. More details with respect to the interpretation of the anomalous Hall effect are discussed in Ref. [29, 73].

In the following, the high-field regime is considered where the constant slopes $d\rho_{xy}/d(\mu_0H)$ are positive indicating hole conduction. The saturation of the magnetic moment at high magnetic fields was confirmed by SQUID measurements of the thin films at low temperatures. In these measurements the magnetic field vector is parallel to the film surface, i.e. the demagnetization factor (see page 12) is equal to zero. In Fig. 2.6 the hysteresis loop of the $La_{0.67}Ca_{0.33}MnO_3$ sample is shown. Clearly small fields around 0.5 T are sufficient to achieve nearly full saturation magnetization. In the case of $La_{0.67}Ca_{0.33}MnO_3$ and $La_{0.67}Sr_{0.33}MnO_3$ the average magnetization per formula unit (f.u.) or unit cell volume (ucv) is

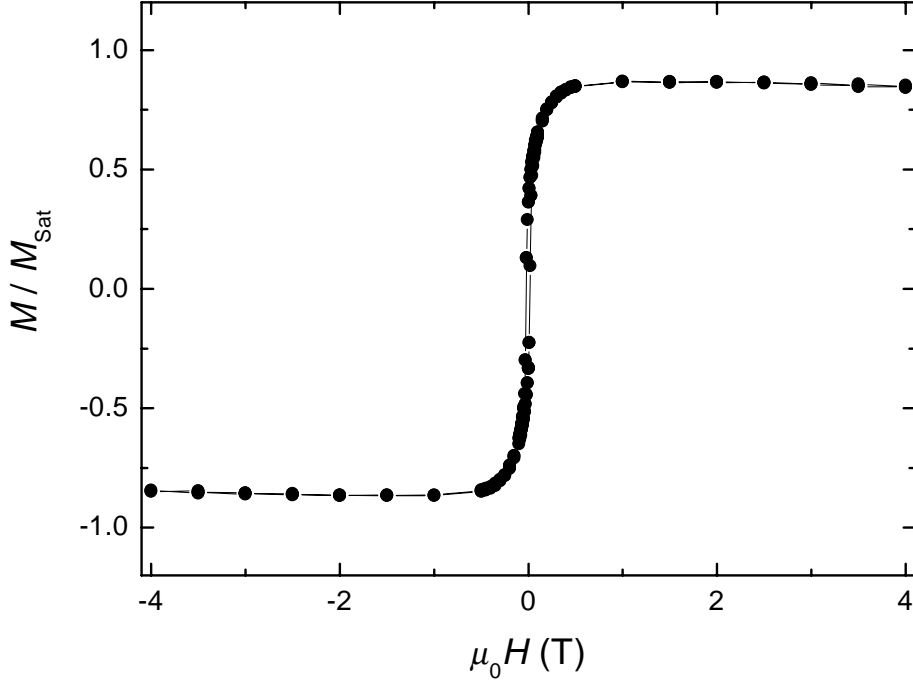


Figure 2.6: Ferromagnetic hysteresis curve for the $\text{La}_{0.67}\text{Ca}_{0.33}\text{MnO}_3$ film measured at 20 K normalized to the expected saturation value. The magnetic field vector is parallel to the film surface. The error of the measured magnetic moments is smaller than the symbol size. However, the uncertainty in film thickness leads to a possible error of 10% in the scale factor. The diamagnetism of the substrate is responsible for the small decrease of the magnetic moment at high magnetic fields.

given by an alignment of all local Mn^{3+} and Mn^{4+} spins

$$M_{\text{Sat}} = \frac{4 \mu_{\text{B}} \cdot 0.67 + 3 \mu_{\text{B}} \cdot 0.33}{\text{ucv}} = \frac{3.67 \mu_{\text{B}}}{\text{ucv}} = 5.96 \times 10^5 \frac{\text{A}}{\text{m}} \quad (2.3)$$

with μ_{B} the Bohr magneton. The orbital angular momentum does not contribute to the magnetization.

Due to the different demagnetization factors in magnetization ($N \approx 0$) and transport measurements ($N \approx 1$) the saturation field in the Hall measurements will be enhanced by $\mu_0 M_{\text{Sat}} \approx 0.75$ T (see Eq. 2.3) to approximately $\mu_0 H_{\text{Sat}} = 1.25$ T, well below the field range of 4 T – 8 T where the data are evaluated. Even if a residual increase of the film magnetization will take place at high fields, it will have a negligible contribution to the slope $d\rho_{xy}/d(\mu_0 H)$ at low temperatures, where the anomalous Hall coefficient vanishes. For 4 K, one obtains using a single-band model a charge-carrier concentration $n = 1.4$ holes/f.u. for $\text{La}_{0.67}\text{Sr}_{0.33}\text{MnO}_3$. A smaller value of 1 hole/f.u. was found by Asamitsu and Tokura on single crystals [102] while for a thin film 2.1 holes/f.u. was reported [90, 91]. For the sputtered Ca-doped counterparts values around 1.3 holes/f.u. at 4 K were determined [29]. Similar values were published by Matl *et al.* [103]

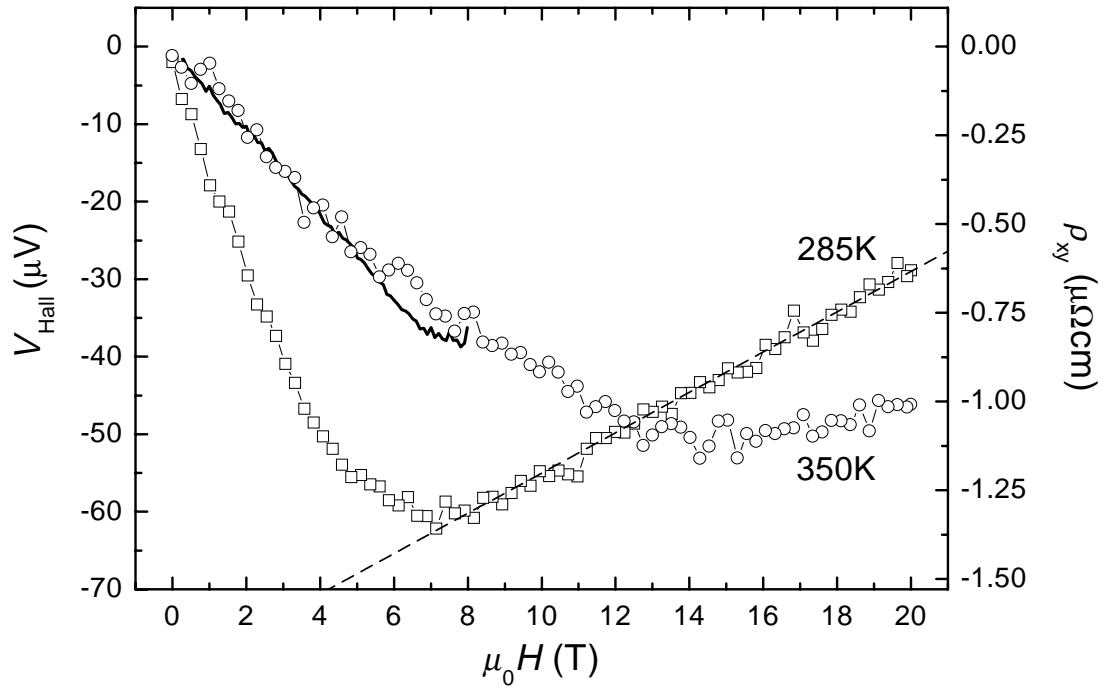


Figure 2.7: Measured Hall resistivities ρ_{xy} and Hall voltages V_{Hall} as functions of external magnetic field at temperatures of 285 K (squares) and 350 K (circles) for $La_{0.67}Ca_{0.33}MnO_3$. The measurements were carried out in a 20 T Bitter magnet. Five measured curves were omitted for clarity. The solid line is a measurement in a 8 T superconducting magnet and shows the agreement between different experimental setups. The dashed line is a linear fit of the slope between 10 T and 20 T.

and in an $La_{2/3}(Ca,Pb)_{1/3}MnO_3$ single crystal the concentration was identified to 2.4 holes/f.u. [104]. These large values for the charge-carrier density in manganites requires the concept of a partly compensated Fermi surface calculated by Pickett and Singh [105].

To investigate the charge-carrier concentration just above T_C , it is important to have magnetic fields as high as possible in order to saturate the magnetization. Therefore, Hall effect measurements were performed for the Ca-doped sample up to 20 T using a Bitter magnet. In this field a positive constant slope $d\rho_{xy}/d\mu_0 H$ can be observed up to $T/T_C = 1.3$. The Hall resistivities $\rho_{xy}(\mu_0 H)$ are shown in Fig. 2.7. For clarity several curves ($T = 275$ K, 300 K, 305 K, 310 K and 315 K) are omitted. Just above T_C at 285 K it is yet possible to almost saturate the magnetization of the sample and a broad field range with a linear dependence remains to evaluate R_H . The fit of the slope between 10 T and 20 T is indicated in Fig. 2.7 by the dashed line. At 350 K ($T/T_C = 1.5$) the shift of the minimum in the Hall voltage to higher fields allows no longer a quantitative analysis of R_H .

Assuming full saturation of the magnetization in high magnetic fields the charge-carrier concentration n as a function of the reduced temperature T/T_C for

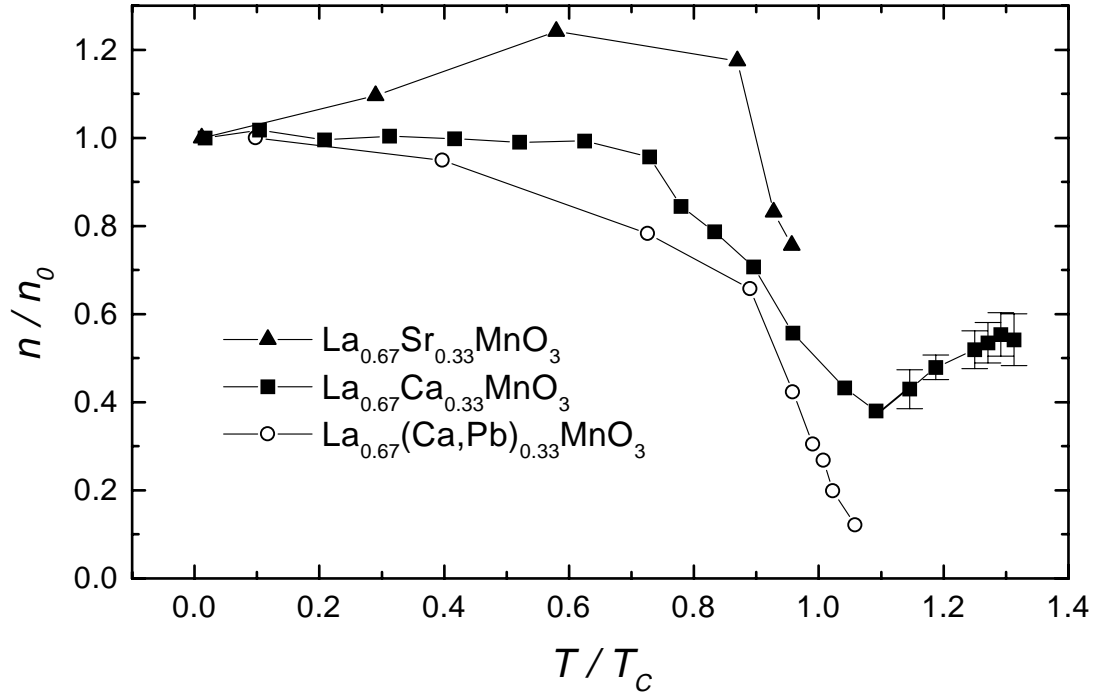


Figure 2.8: Normalized charge-carrier density $n \propto (d\rho_{xy}/d(\mu_0 H))^{-1}$ of $\text{La}_{0.67}\text{Ca}_{0.33}\text{MnO}_3$ (filled squares, $T_C = 232$ K) and $\text{La}_{0.67}\text{Sr}_{0.33}\text{MnO}_3$ (filled triangles, $T_C = 345$ K) as a function of the reduced temperature T/T_C . For the measurements in the 12 T superconducting magnet errors are comparable to symbol size. In the 20 T Bitter magnet electrical noise leads to enhanced error bars for the slopes $(d\rho_{xy}/d(\mu_0 H))^{-1}$ as indicated. Additionally data are shown from Ref. [104] (open circles, $T_C = 287.5$ K) on a single crystal of $\text{La}_{0.67}(\text{Ca,Pb})_{0.33}\text{MnO}_3$.

$\text{La}_{0.67}\text{Ca}_{0.33}\text{MnO}_3$ (squares) and $\text{La}_{0.67}\text{Sr}_{0.33}\text{MnO}_3$ (triangles) is plotted in Fig. 2.8. The Ca-doped compound has a constant carrier concentration at low temperatures, whereas for the Sr-doped sample n increases with temperature. Nevertheless, for both doped manganites, a decrease of n nearby the Curie temperature is clearly seen. This temperature dependence of n seems to be a characteristic behavior of the manganites in the vicinity of T_C , since this was also observed by Wagner *et al.* [106] in thin films of $\text{Nd}_{0.5}\text{Sr}_{0.5}\text{MnO}_3$, indirectly by Ziese *et al.* [107] in thin films of $\text{La}_{0.67}\text{Ca}_{0.33}\text{MnO}_3$ and $\text{La}_{0.67}\text{Ba}_{0.33}\text{MnO}_3$ and by Chun *et al.* [104] in single crystals of $\text{La}_{0.67}(\text{Ca,Pb})_{0.33}\text{MnO}_3$. The latter data are also shown as open circles in Fig. 2.8 for comparison. The experimentally determined increase of the ordinary Hall coefficient at the metal-insulator transition translates into a charge-carrier density collapse (CCDC) in the band picture. According to Fig. 2.8 the number of charge-carriers seems to reincrease above T_C . The error bars indicate the accuracy of the determination of the constant slopes $d\rho_{xy}/d(\mu_0 H)$, as shown for $T = 285$ K in Fig. 2.7. However, well above the Curie temperature, the magnetization of the sample cannot be saturated in experimentally accessible

magnetic fields. From the derivative of Eq. 1.6

$$\frac{d\rho_{xy}}{d(\mu_0 H)} = R_H + R_A \frac{dM}{dH}, \quad (2.4)$$

it is obvious, that a linearly increasing magnetization in the paramagnetic regime does not affect the linear field dependence of the Hall resistivity ρ_{xy} but changes its slope $d\rho_{xy}/d(\mu_0 H)$. Without quantitative knowledge of the anomalous Hall coefficient R_A and the sample magnetization $M(T, H)$, it is not possible to separate this contribution. Nevertheless, since the sign of the anomalous Hall contribution is electronlike, it is quite evident that the apparent charge-carrier density shown in Fig. 2.8 has to be corrected to *lower* values above the Curie temperature, thus *enhancing* the CCDC.

This CCDC indicates strong changes in the electronic distribution function close to the Fermi energy. Since coincidence of structural, magnetic and electronic phase transitions has been reported for $\text{La}_{1-x}\text{Ca}_x\text{MnO}_3$ with $x = 0.25$ and $x = 0.50$ [108], the temperature dependence of lattice constants, magnetization, longitudinal resistivity, and transversal resistivity for the same sample were investigated. Fig. 2.9 shows a compilation of the results. The charge-carrier density is constant up to $0.7 T_C$. In this temperature range the longitudinal resistivity follows Eq. 2.1 and the volume of the unit cell increases slowly with temperature. The fact that the CCDC is accompanied by a strong increase in unit cell volume and longitudinal resistivity as well as a decay of the spontaneous magnetization shows the coincidence of structural, magnetic, and electronic phase transitions in $\text{La}_{0.67}\text{Ca}_{0.33}\text{MnO}_3$.

As the transport in the manganites above T_C is dominated by polaron hopping [29, 100, 101], the relation between the experimental observation of the CCDC and the polaronic CCDC as proposed recently by Alexandrov and Bratkovsky [109] is discussed. They worked out the theory for a CCDC due to a phase transition of mobile polarons to immobile bipolaronic pairs. At low temperatures the charge-carriers form a polaronic band. With increasing temperature the polaronic bandwidth decreases due to the increase in electron-phonon coupling. Depending on the polaron binding energy and the doping level a first or second order phase transition to a bound bipolaronic state takes place. At still higher temperatures thermal activation of the bipolarons leads to a reincrease of the number of mobile polarons. Indeed their calculated temperature dependence of the number density of mobile polarons in zero field is very similar to the experiment as shown in Fig. 2.8. However, in this model the density of mobile polarons close to T_C is a strong function of magnetic field, which is responsible for the colossal magnetoresistance. In high magnetic fields the polaronic CCDC is strongly reduced, since the formation of bound bipolarons is suppressed and accordingly the number of mobile polarons remains almost constant at T_C . Therefore, the observation of

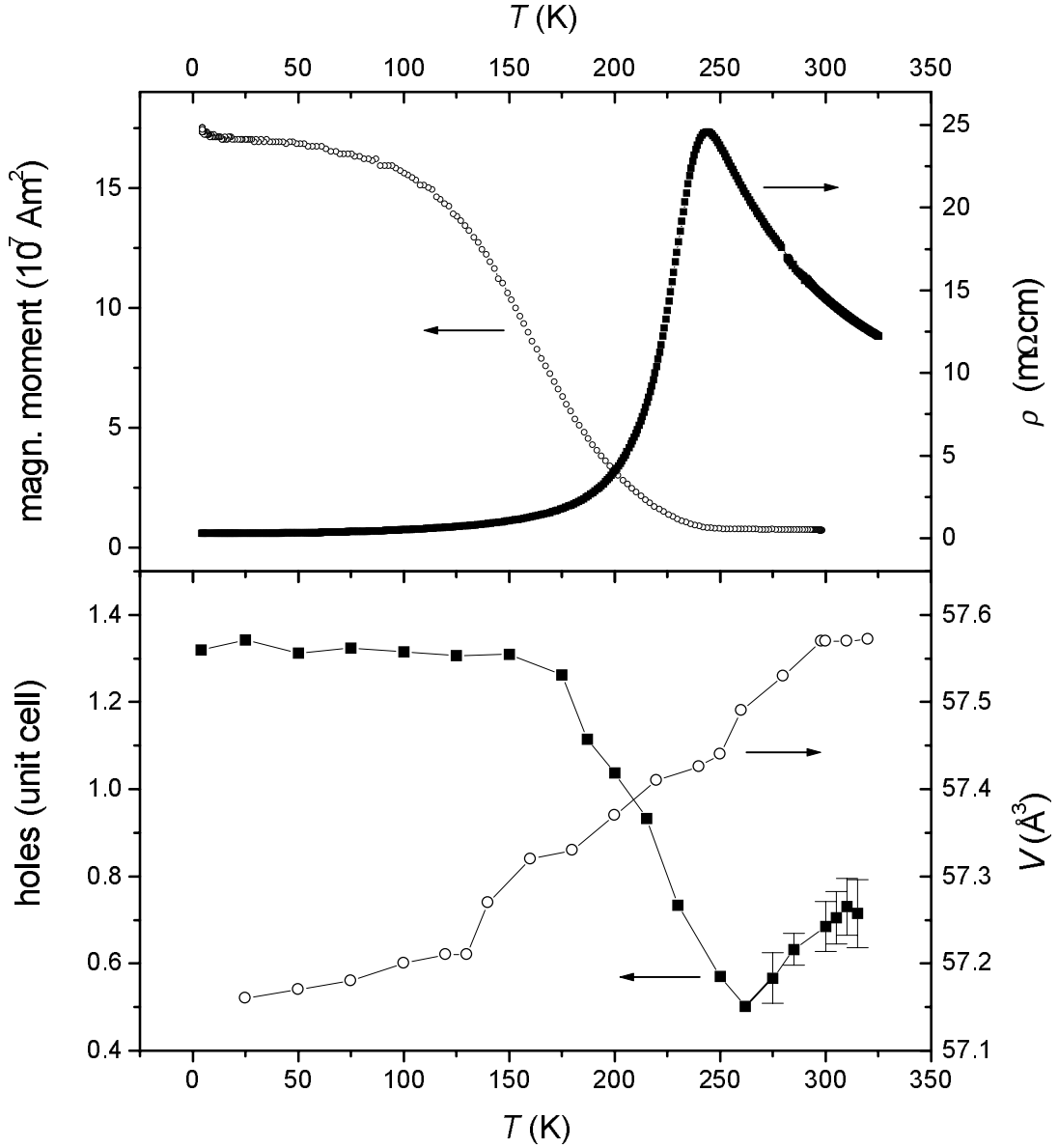


Figure 2.9: Temperature dependence of spontaneous magnetization, zero field resistivity, charge-carrier density, and unit cell volume in zero field for an epitaxial $\text{La}_{0.67}\text{Ca}_{0.33}\text{MnO}_3$ thin film. The coincidence of structural, magnetic, and electronic phase transitions in manganites is obvious.

a CCDC in high fields cannot be identified with the CCDC due to bipolaron formation, but is rather related to structural changes. The charge-carrier density cannot be determined in the low-field regime due to strong anomalous Hall contributions. In their presence the type of phase transition proposed by Alexandrov and Bratkovsky cannot be verified by Hall effect measurements.

2.4 Conclusion

In summary, epitaxial $\text{La}_{0.67}\text{Ca}_{0.33}\text{MnO}_3$ and $\text{La}_{0.67}\text{Sr}_{0.33}\text{MnO}_3$ thin films were prepared by magnetron sputtering and laser ablation, respectively. The longitudinal and transverse resistivities were investigated as function of temperature and magnetic field. In the low temperature range electron-magnon scattering in the longitudinal resistivity was identified.

In the Ca- and Sr-doped manganite thin films a large charge-carrier density of 1.3 holes/f.u. and 1.4 holes/f.u., respectively, was found at low temperatures. At the ferromagnetic transition temperature a charge-carrier density collapse was observed for both compounds. The data indicate a simultaneous structural, magnetic, and electronic phase transition in doped manganite thin films.

With Sr doping instead of Ca doping the Curie temperature could be shifted above room temperature. Thus, the CMR could be enhanced at ambient temperature. Nevertheless, other methods to obtain a more significant MR in low magnetic fields have to be found. One of these methods, increasing the sensitivity of the MR in low magnetic fields by orders of magnitude, is described in the next chapter.

Chapter 3

Artificial grain boundaries in $\text{La}_{0.67}\text{Ca}_{0.33}\text{MnO}_3$ thin films

One motivation for the intense research on CMR materials is the prospect to use these materials for magnetic field sensors. However, a strong field in the Tesla range is necessary to obtain large resistance changes based on the CMR effect as discussed in the preceding chapter. A much more promising path may be found in electronic devices exploiting the electron spin more directly. In manganites the half-metallic ground state has a highly spin polarized conduction band, which allows to achieve high MR in low fields because of spin polarized tunneling.

A large number of natural grain boundaries exists in polycrystalline bulk materials which can act as tunneling barriers. A clear difference in low-field magnetotransport between a single crystal and polycrystalline powder of the same material was shown by Hwang *et al.* [110]. A similar approach is to use polycrystalline substrates with a defined grain size to produce epitaxial polycrystalline films with the same size of the grains [111]. As it is well known from thin film preparation in the field of high-temperature superconductivity [112], a further access is to deposit epitaxial thin manganite films on bicrystal substrates to realize a single artificial grain boundary (GB) [113, 114].

Another possibility is to design an artificial tunneling barrier, e.g. preparation of a heteroepitaxial trilayer tunnel junction on a substrate. The junction consists of two ferromagnetic electrodes and a thin insulating barrier as Al_2O_3 or SrTiO_3 in between. The two electrodes can be both metals $\text{CoFe}/\text{Al}_2\text{O}_3/\text{Co}$ [115] or both manganites $\text{La}_{0.67}\text{Sr}_{0.33}\text{MnO}_3/\text{SrTiO}_3/\text{La}_{0.67}\text{Sr}_{0.33}\text{MnO}_3$ [116, 117] or a mixture of a metal and an oxide electrode $\text{Co}/\text{SrTiO}_3/\text{La}_{0.67}\text{Sr}_{0.33}\text{MnO}_3$ [118]. Alternatives are ramp-edge junctions [119, 120] or thin films under compressive strain [121].

In order to understand the mechanism of the large low-field MR the resistivity of Ca-doped manganite thin films with and without an artificial GB, induced by a bicrystal substrate, was studied as a function of temperature, magnetic field, and current density.

3.1 Thin film deposition on bicrystal substrates

Epitaxial thin films of $\text{La}_{0.67}\text{Ca}_{0.33}\text{MnO}_3$ were grown from a stoichiometric target by pulsed laser deposition with the same system and under the same conditions described in the previous chapter. As substrates SrTiO_3 bicrystals with a 45° artificial GB or SrTiO_3 monocrystals were used. The film thicknesses were chosen to 190 nm determined with a Mireau interferometer.

3.2 Characterization

3.2.1 Crystallographic properties

In X-ray diffraction, in Bragg-Brentano geometry, only film reflections corresponding to a $(l00)$ orientation of the cubic perovskite cell are visible. Fig. 3.1 shows the (200) reflection of $\text{La}_{0.67}\text{Ca}_{0.33}\text{MnO}_3$ in the neighborhood of the (200) reflection of SrTiO_3 . The lattice parameter normal to the substrate plane ($a = 3.821 \text{ \AA}$) is smaller than the bulk value and indicates a tensile strain of the in-plane axes due to the substrate lattice mismatch ($a = 3.905 \text{ \AA}$). The full width at half maximum of the $\text{La}_{0.67}\text{Ca}_{0.33}\text{MnO}_3$ (200) rocking curve is 0.03° on both sides

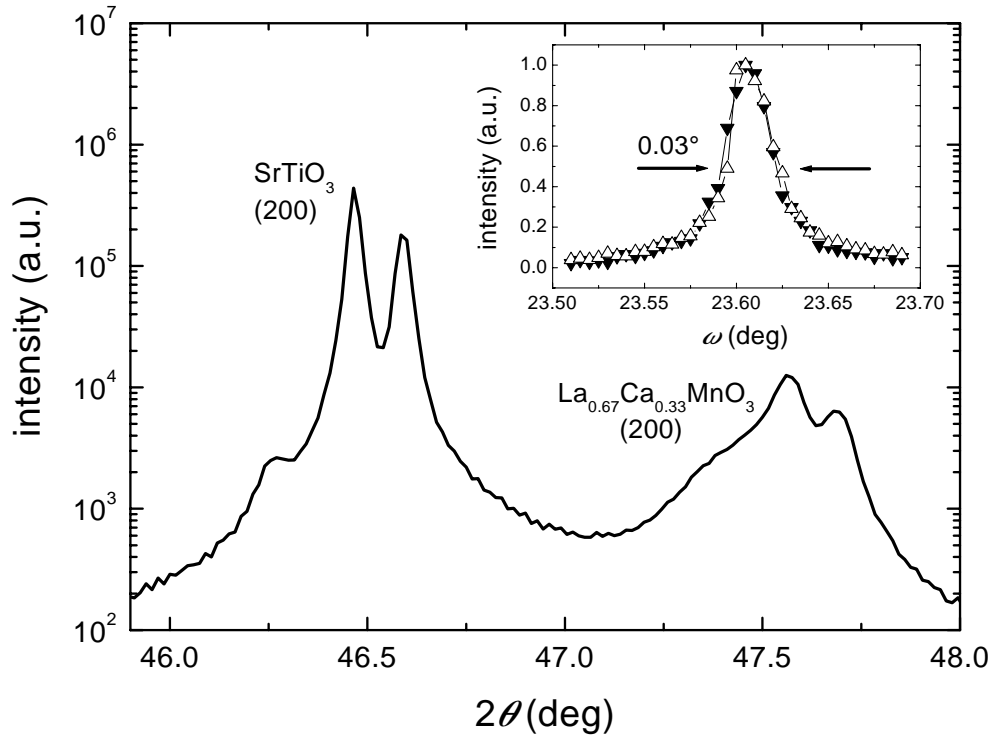


Figure 3.1: $\theta/2\theta$ -scan of a $\text{La}_{0.67}\text{Ca}_{0.33}\text{MnO}_3$ thin film on SrTiO_3 . The (200) reflection peak (Cu $K\alpha$ doublet) is shown. The inset presents rocking curves of the (200) reflection peak on both sides of the bicrystal.

(opened and filled triangles) of the artificial GB as shown in the inset of Fig. 3.1 indicating an epitaxial ($l00$) axis oriented growth. The in-plane orientation was investigated by ϕ -scans on both sides of the bicrystal (black and grey lines) using the $\{202\}$ group of symmetry equivalent reflections as displayed in Fig. 3.2. The perovskite thin film grows relatively to the perovskite substrate cube on cube with an angular spread in the orientation of the individual epitaxial grains of less than 0.5° . Thus the 45° GB in the film induced by the bicrystal substrate is the only relevant large-angle GB in the following experiment.

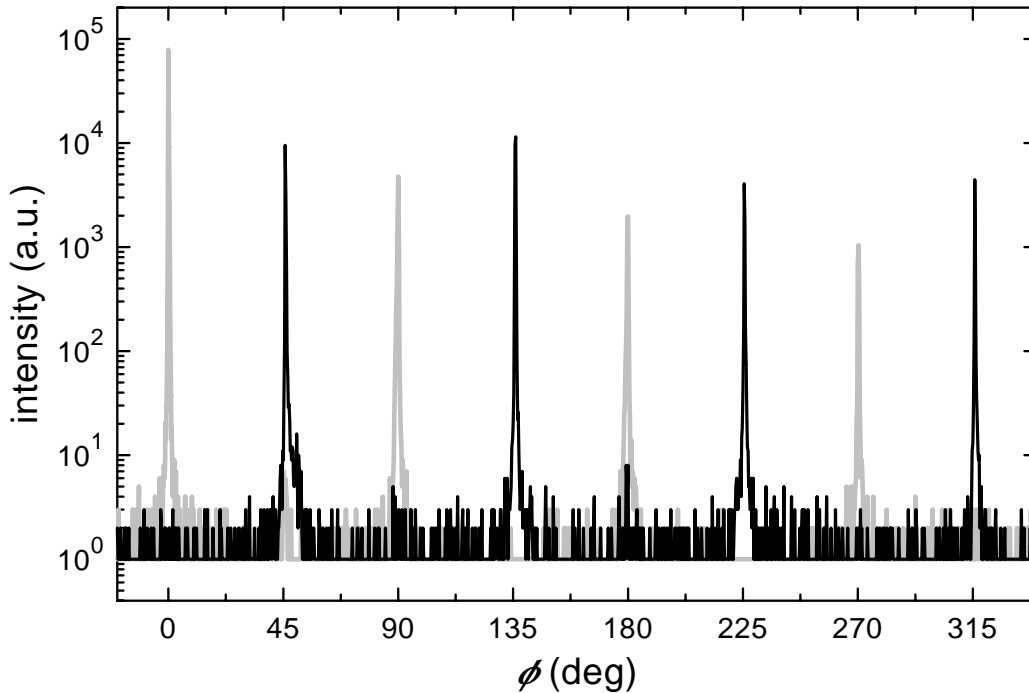


Figure 3.2: ϕ -scans on both sides of the bicrystal (black and grey lines) using the $\{202\}$ group of symmetry equivalent reflections. The 45° shift in the film reflections induced by the artificial GB is obvious.

3.2.2 Morphology

The surface morphology of the samples was studied by scanning electron (SEM) and by atomic force microscopy (AFM). An AFM area scan ($8 \times 8 \mu\text{m}^2$) showing the GB is presented in Fig. 3.3a. A shallow triangular trench structure of 200 nm width and 5 nm depth along the grain boundary was visible in a linescan (indicated in Fig. 3.3a by a white line) shown in Fig. 3.3b. The GB itself was identified as a further sharp dip with characteristic dimensions close to the resolution limit of the used wide area scanner. The SEM scan in Fig. 3.3c reveals that the actual distorted GB region is smaller than 50 nm.

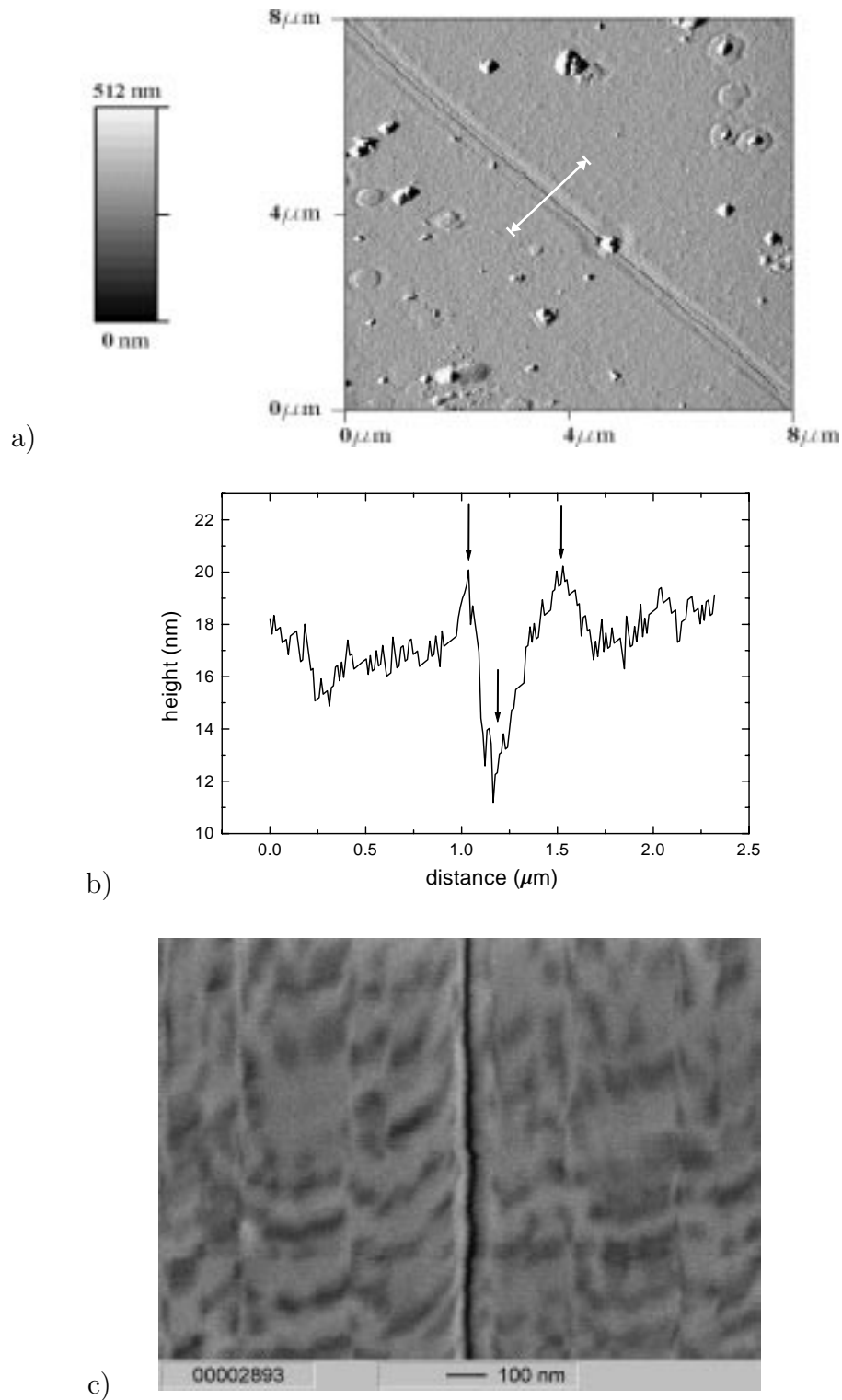


Figure 3.3: a) AFM area scan of the grain boundary in a $La_{0.67}Ca_{0.33}MnO_3$ film. b) Line scan across the distorted region indicated by a white line in part a of the figure. c) SEM scan of the GB induced by the bicrystal substrate in the same Ca-doped thin film. Film growth is distorted on the GB in a region with a width smaller than 50 nm.

3.3 Magnetotransport

The films were patterned with conventional photolithography and wet chemically etched in an acidic solution of hydrogen peroxide [122]. In order to get strips which cross the GB eleven times, meander tracks were chosen. The total length of each meander is 5.6 mm and the width is 0.1 mm. For comparison identical structures were prepared adjacent to the GB, but not crossing it. The geometry

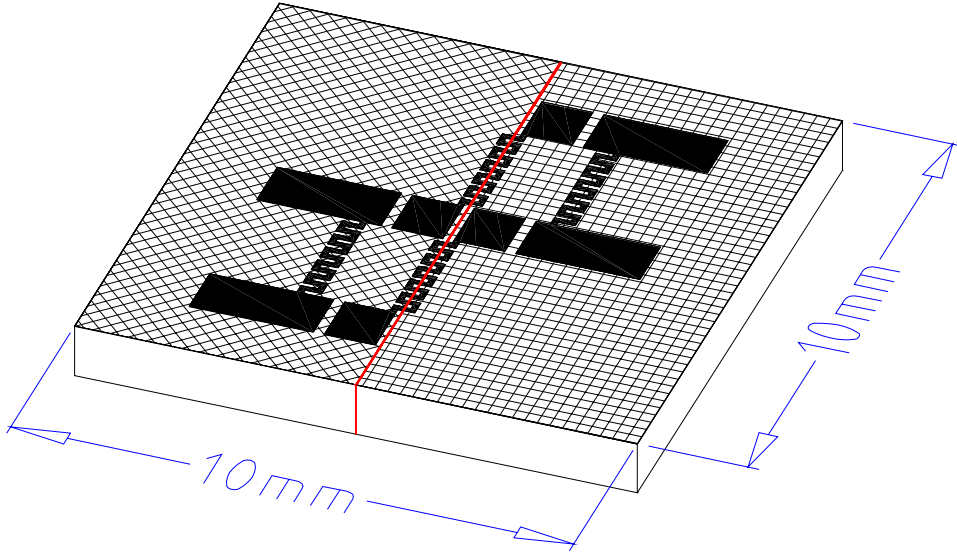


Figure 3.4: *Patterned thin film geometry on a bicrystal substrate. The meander tracks cross the GB eleven times.*

is shown in Fig. 3.4.

The resistivity was measured in a superconducting magnet cryostat by standard four-point technique with a constant DC current between 10 nA and 100 μ A. For higher currents up to 10 mA current pulses of 3 ms length were applied in order to minimize sample heating. To reveal the low-field MR it is necessary to diminish demagnetization effects, which requires that the film plane is parallel to the magnetic field H . Further, the angle between the GB and the magnetic field is important for the MR ratio. In this work the results for $H \parallel$ GB, where the low-field MR is largest, are shown. The control meander away from the GB exhibits no low-field MR in the ferromagnetic regime in contrast to the meander crossing the GB. This unusual behavior can be explained by the Simmons [123, 124] and Jullière models [125] of tunneling which will be described in the following.

3.3.1 Simmons model of tunneling

When two electrodes are separated by a thin insulating barrier there is a nonzero probability of charge transfer through the barrier due to the quantum-mechanical

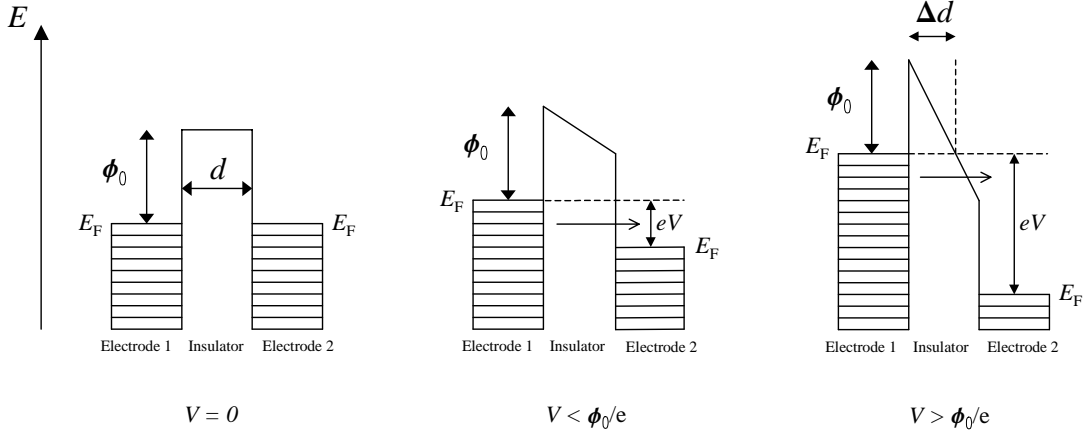


Figure 3.5: Sketch of a rectangular tunneling barrier with height ϕ_0 and thickness d between conducting electrodes [123].

tunneling of electrons. When an external voltage V is applied the energies in the electrodes shift by eV with respect to one another as shown schematically in Fig. 3.5. The barrier height is ϕ_0 . The tunneling currents $I_{1 \rightarrow 2}$ and $I_{2 \rightarrow 1}$ for electrons to tunnel from electrode 1 to 2 and from 2 to 1, respectively, are no longer identical. A net tunnel current I can flow from one side to the other which is in general given by

$$\begin{aligned}
 I &= I_{1 \rightarrow 2} - I_{2 \rightarrow 1} \\
 &= A \sum_{\sigma=\uparrow,\downarrow} |T_\sigma|^2 \int_{-\infty}^{+\infty} N_\sigma^1(E) f(E) N_\sigma^2(E + eV) [1 - f(E + eV)] dE \\
 &\quad - A \sum_{\sigma=\uparrow,\downarrow} |T_\sigma|^2 \int_{-\infty}^{+\infty} N_\sigma^2(E + eV) f(E + eV) N_\sigma^1(E) [1 - f(E)] dE \\
 &= A \sum_{\sigma=\uparrow,\downarrow} |T_\sigma|^2 \int_{-\infty}^{+\infty} N_\sigma^1(E) N_\sigma^2(E + eV) [f(E) - f(E + eV)] dE \quad (3.1)
 \end{aligned}$$

with A a constant of proportionality, f the Fermi function, σ the spin direction, $N_\sigma^{1,2}(E)$ the appropriate density of states, and in general $T_\sigma(E)$ the spin dependent and energy dependent tunneling-matrix elements, which are assumed to be equal for both tunnel directions ($T_{\sigma,1 \rightarrow 2}(E) = T_{\sigma,2 \rightarrow 1}(E)$) and to be constant ($T_\sigma(E) = T_\sigma$) [126]. This assumption is no longer valid for the third case in Fig. 3.5 where the effective barrier thickness depends on the applied voltage. The factors $N_\sigma^1 f$ and $N_\sigma^2 (1 - f)$ give the numbers of occupied initial states and of empty final states in unit energy interval, respectively. It is supposed that no spin flip takes place in the tunneling process.

Simmons derived a theory for a rectangular tunneling barrier [123, 124]. Three cases are to be distinguished, the low-voltage range ($V \ll \phi_0/e$), the interme-

diante-voltage range ($V < \phi_0/e$), and the high-voltage range ($V > \phi_0/e$):

Low-voltage range

In the low-voltage range, i.e. $V \ll \phi_0/e$, the tunneling probability is not affected by the applied voltage and thus the junction is ohmic. This relationship was first obtained by Sommerfeld and Bethe [127]. The current density j according to Simmons is given by

$$j = \frac{1}{d} \left(\frac{e}{h} \right)^2 \sqrt{2m\phi_0} V \exp \left(-\frac{4\pi d}{h} \sqrt{2m\phi_0} \right) \quad (3.2)$$

$$j/\text{A/cm}^2 = 3.16 \times 10^9 \sqrt{\phi_0/\text{eV}} \frac{V/\text{V}}{d/\text{nm}} \exp \left(-10.25 d/\text{nm} \sqrt{\phi_0/\text{eV}} \right)$$

with m the free electron mass and d the barrier thickness. The differential conductivity $G = dj/dV$ is in this regime constant:

$$G = \text{const.} \quad (3.3)$$

Intermediate-voltage range

In the intermediate-voltage range, i.e. $V < \phi_0/e$, the current-voltage characteristic of the junction is nonohmic. In this regime, the current is given by

$$j = \frac{e}{2\pi h(\beta d)^2} \left\{ \left(\phi_0 - \frac{eV}{2} \right) \exp \left(-\frac{4\pi\beta d}{h} \sqrt{2m} \sqrt{\left(\phi_0 - \frac{eV}{2} \right)} \right) - \left(\phi_0 + \frac{eV}{2} \right) \exp \left(-\frac{4\pi\beta d}{h} \sqrt{2m} \sqrt{\left(\phi_0 + \frac{eV}{2} \right)} \right) \right\} \quad (3.4)$$

$$j/\text{A/cm}^2 \stackrel{\beta=1}{=} \frac{6.17 \times 10^8}{(d/\text{nm})^2} \left\{ \left(\phi_0/\text{eV} - \frac{V/\text{V}}{2} \right) \exp \left(-10.25 d/\text{nm} \sqrt{\phi_0/\text{eV} - \frac{V/\text{V}}{2}} \right) - \left(\phi_0/\text{eV} + \frac{V/\text{V}}{2} \right) \exp \left(-10.25 d/\text{nm} \sqrt{\phi_0/\text{eV} + \frac{V/\text{V}}{2}} \right) \right\}$$

with β a correction factor close to unity which depends on V (here $\beta = 1$ [123]). At relatively low voltages an interesting limit of Eq. 3.4 has been considered by Simmons [128]. On expanding the exponentials and dropping terms of V^4 or higher order, the derivation of Eq. 3.4 reduces to

$$G = \alpha \left(1 + 3\gamma V^2 \right). \quad (3.5)$$

whera α and γ are constants. The first term is the familiar ohmic region and the second term is the parabolic dependence symmetric about zero bias. Equation 3.5 is known as the parabolic approximation [129].

High-voltage range

In the high-voltage range, i.e. $V > \phi_0/e$, the effective barrier thickness Δd decreases with increasing V as sketched in the right part of Fig. 3.5. The effective barrier thickness is given by

$$\Delta d = \frac{d\phi_0}{eV} = \frac{\phi_0}{eE} \quad (3.6)$$

with $E = V/d$ the field strength. For the current density this yields:

$$j = \frac{2e^3}{8\pi h\phi_0} \left(\frac{E}{\beta}\right)^2 \left\{ \exp\left(-\frac{4\pi\beta}{heF}\sqrt{m}\phi_0^{\frac{3}{2}}\right) - \left(1 + \frac{2eV}{\phi_0}\right) \exp\left(-\frac{4\pi\beta}{heF}\sqrt{m}\phi_0^{\frac{3}{2}}\sqrt{\left(1 + \frac{2eV}{\phi_0}\right)}\right) \right\} \quad (3.7)$$

$$j/A/\text{cm}^2 \stackrel{\beta=23/24}{\cong} \frac{3.36 \times 10^8 (V/V)^2}{\phi_0/eV (\Delta d/\text{nm})^2} \left\{ \exp\left(-\frac{6.94\Delta d/\text{nm}}{V/V}(\phi_0/eV)^{\frac{3}{2}}\right) - \left(1 + \frac{2V}{\phi_0/eV}\right) \exp\left(-\frac{6.94\Delta d/\text{nm}}{V/V}(\phi_0/eV)^{\frac{3}{2}}\sqrt{\left(1 + \frac{2V}{\phi_0/eV}\right)}\right) \right\}.$$

In this case the correction factor is constant $\beta = 23/24$ [123]. For even higher voltages the Fermi level of electrode 2 lies below the bottom of the conduction band of electrode 1. Under these conditions, electrons cannot tunnel from electrode 2 to electrode 1, since there are no empty levels available to them. The situation is reversed for electrons tunneling from electrode 1 to electrode 2, since all of the available levels in electrode 2 are empty. The situation is analogous to that of field emission from a metal electrode explained first by Fowler and Nordheim [130].

3.3.2 Jullière model of tunneling

Nonlinear I - V curves are often taken as an indication for tunneling transport. The inclusion of spin dependent density of states $N_{\uparrow}(E), N_{\downarrow}(E)$ and hysteretic magnetizations in ferromagnetic materials on both sides of the tunneling barrier can explain a hysteretic MR.

The spin tunneling polarization P is defined by

$$P \equiv \frac{N_{\uparrow}(E_F) |T_{\uparrow}|^2 - N_{\downarrow}(E_F) |T_{\downarrow}|^2}{N_{\uparrow}(E_F) |T_{\uparrow}|^2 + N_{\downarrow}(E_F) |T_{\downarrow}|^2} \approx \frac{N_{\uparrow} - N_{\downarrow}}{N_{\uparrow} + N_{\downarrow}} = 2a - 1 \quad (3.8)$$

where $|T_{\uparrow}|^2$ and $|T_{\downarrow}|^2$ are assumed to be equal and a is the fraction of the electrons whose spin is in the direction of the applied magnetic field [46]. The high spin polarization can be exploited in a tunnel junction as sketched in Fig. 3.6. A thin

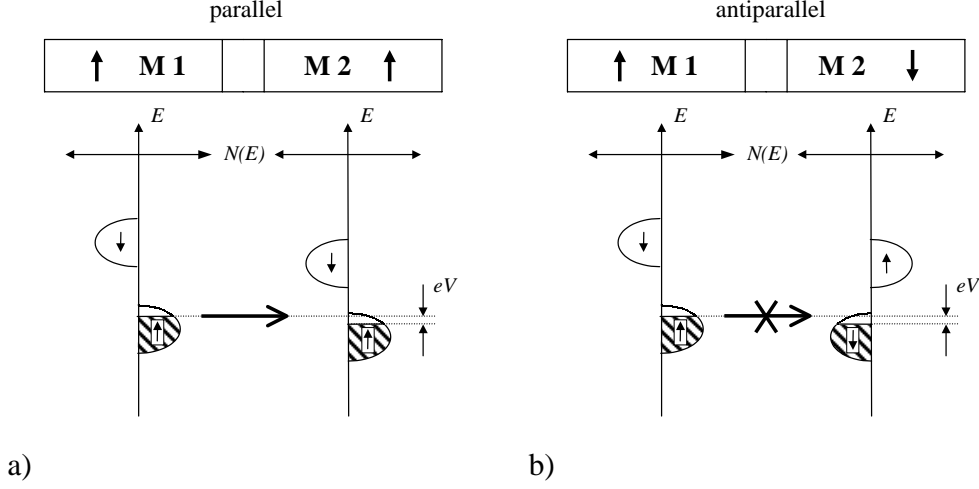


Figure 3.6: Density of states in the junction for the parallel (part a) and antiparallel (part b) configuration. In the antiparallel configuration no tunnel current flows. There are no empty states in metal 2 into which the electron with the same spin direction can tunnel.

insulating barrier separates two magnetic layers M1 and M2. Two cases, parallel and antiparallel configuration of the magnetizations, are shown. The tunneling current $I_{1 \rightarrow 2}$ for low voltages V is proportional to the density of occupied states N_{σ}^1 in metal 1 times the density of unoccupied states N_{σ}^2 in metal 2, with $\sigma = \uparrow, \downarrow$. Spin flip processes are not allowed in the elastic tunneling process. The tunneling currents in the parallel (I_P) and antiparallel (I_A) cases are given by

$$I_P = N_{\uparrow}^1 N_{\uparrow}^2 + N_{\downarrow}^1 N_{\downarrow}^2 \quad > \quad I_A = N_{\uparrow}^1 N_{\downarrow}^2 + N_{\downarrow}^1 N_{\uparrow}^2 \quad (3.9)$$

when the tunnel probability is independent of the spin state. The normalized difference of the tunneling currents is equal to the product of the polarizations of the electrodes [45]:

$$\frac{I_P - I_A}{I_P + I_A} = \frac{(N_{\uparrow}^1 - N_{\downarrow}^1)(N_{\uparrow}^2 - N_{\downarrow}^2)}{(N_{\uparrow}^1 + N_{\downarrow}^1)(N_{\uparrow}^2 + N_{\downarrow}^2)} = P^1 P^2 \quad (3.10)$$

Finally, the polarization can be determined by measuring the resistance in the parallel R_P and antiparallel arrangement as expressed by

$$\frac{I_P - I_A}{I_A} = \frac{R_A - R_P}{R_P} = \left(\frac{\Delta R}{R} \right)_{\max} = \frac{2P^1 P^2}{1 - P^1 P^2} \quad (3.11)$$

or in other words, the maximal MR $(\Delta R/R)_{\max}$ increases with increasing polarization. In the case of half-metallic manganites the junction is in the antiferromagnetic arrangement an insulator and the MR should diverge.

3.3.3 Low-field magnetoresistance

The resistances of the meander tracks as a function of temperature show the usual maximum in the resistivity and its suppression in high magnetic fields as discussed in the previous chapter. The conductivity above the Curie temperature $T_C = 225$ K is thermally activated, which can be explained by small polaron hopping [29, 73]. At low temperatures, the behavior of the two meanders is not the same. The difference between the meander resistance on and next to the GB isolates the temperature dependence of the true GB resistance. In agreement with published data there is a broad flat peak around 100 K below T_C [131].

In Fig. 3.7 the resistivity as a function of magnetic field at 4.2 K measured

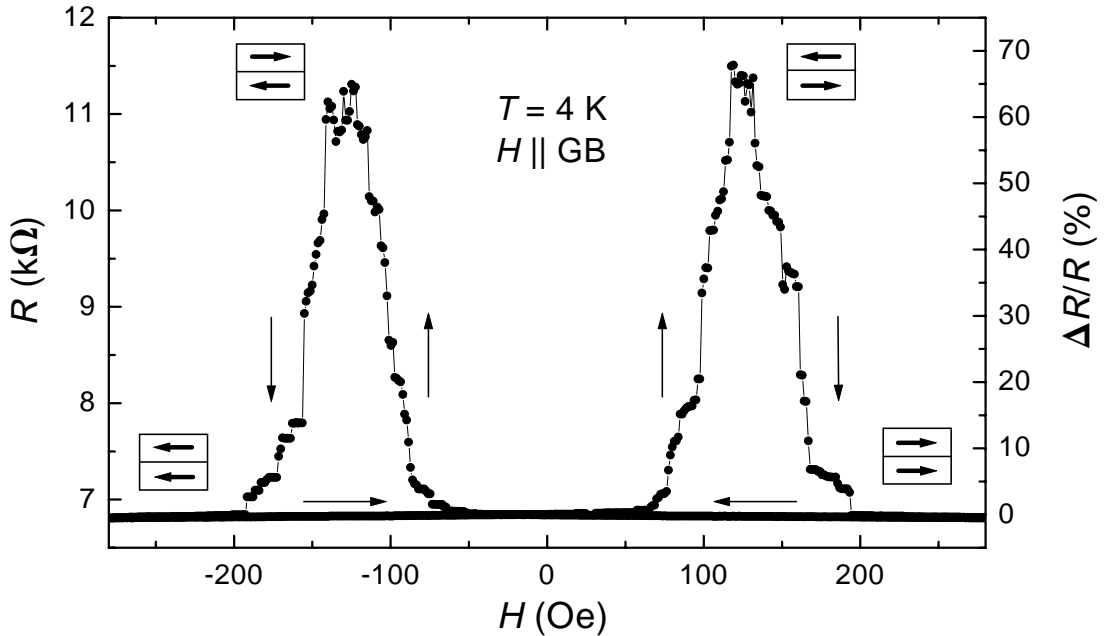


Figure 3.7: GB resistance and MR at $T = 4.2$ K as a function of magnetic field.

with a constant DC current of $1 \mu\text{A}$ is shown. The MR is defined by

$$\text{MR} = \frac{R(H) - R(H = 0)}{R(H = 0)} = \frac{\Delta R}{R} \quad (3.12)$$

and reaches its maximum value of 70% in a field of 120 Oe at 4.2 K, which is approximately equal to the coercitive field H_C . When the magnetic field is increased from a field below $-H_C$ one layer will switch at $+H_C$ and the antiparallel configuration of the magnetizations on both sides of the GB leads to a high resistance. At even higher fields, the second layer switches also according to the external magnetic field direction, and one obtains a parallel arrangement with a low resistance in high fields. Decreasing the field now through $+H_C$ down to zero does not change the parallel configuration. Further decreasing down to $-H_C$ leads to

a switch of one layer and again an antiparallel configuration exists. Therefore, one obtains a hysteretic MR. According to Eq. 3.11 with equal electrodes the maximum MR is given by

$$\left(\frac{\Delta R}{R}\right)_{\max} = \text{MR}_{\max} = \frac{2P^2}{1 - P^2}. \quad (3.13)$$

A value of 70% for $(\Delta R/R)_{\max}$ translates in $P \approx 0.51$ for $\text{La}_{0.67}\text{Ca}_{0.33}\text{MnO}_3$. It is worth mentioning here that the different steps and switches in Fig. 3.7 indicate that in the neighborhood of the GB multiple magnetic domains exist, and thus the spin polarization parameter, which should be nearly 100%, will be underestimated. The highest value of $P = 83\%$ for manganites was reached with tunneling in trilayers ($\text{La}_{0.67}\text{Sr}_{0.33}\text{MnO}_3/\text{SrTiO}_3/\text{La}_{0.67}\text{Sr}_{0.33}\text{MnO}_3$) [117].

For higher temperatures, the maximum low-field MR decreases almost linearly down to 125 K as can be seen in Fig. 3.8 and Fig. 3.9. This temperature dependence scales not with the temperature dependence of the magnetization. It is assumed that the surface magnetization which has a different temperature dependence as the bulk magnetization is responsible for this effect [132]. This behavior is different to that of magnetic tunnel junctions, where below 100 K

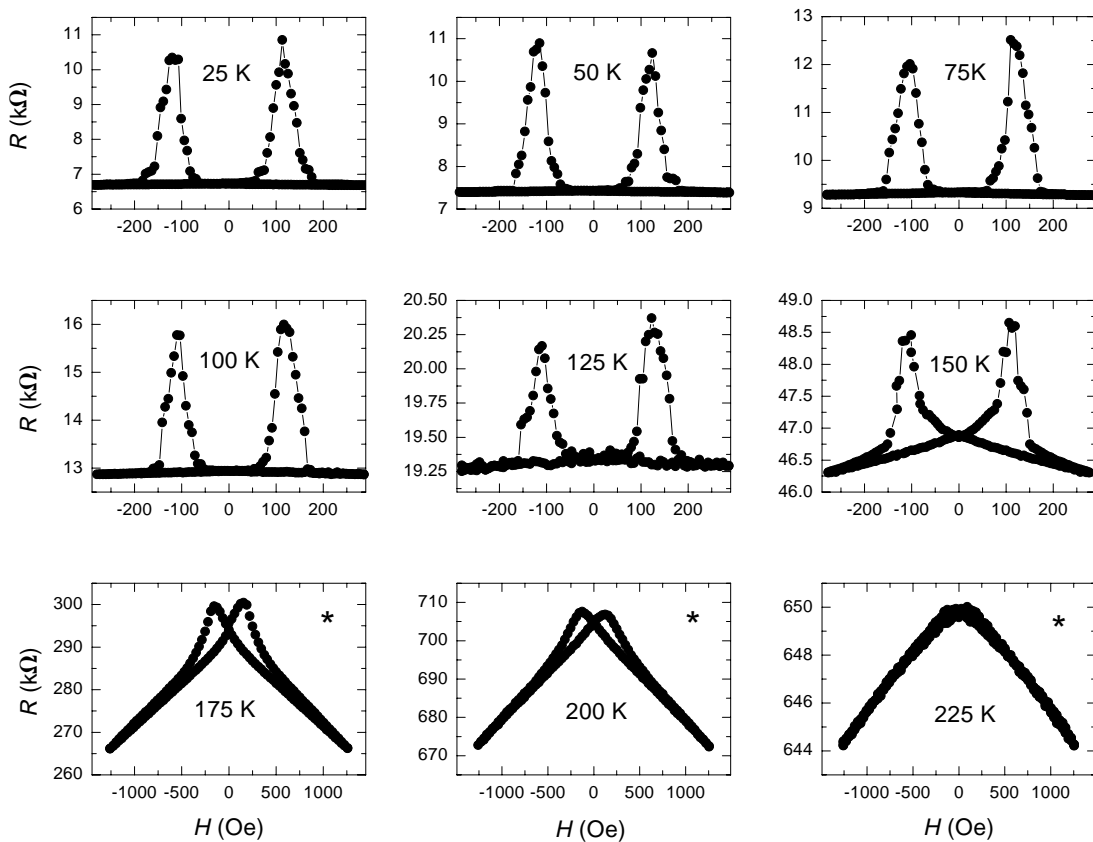


Figure 3.8: *Hysteretic low-field MR at several constant temperatures. The asterisk indicates a broader field range.*

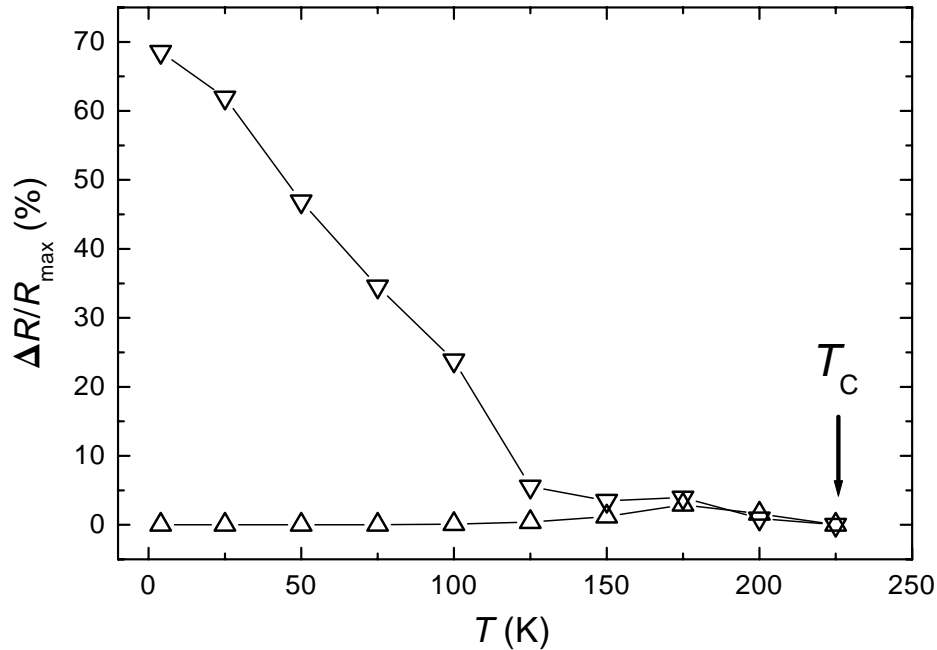


Figure 3.9: Temperature dependence of the maximum low-field MR for the meander crossing (down triangles) and not crossing (up triangles) the GB.

the maximal MR decreases slowly and above 100 K a drop is visible [133]. The magnetic field value, where the maximum MR ratio occurs, does not shift with temperature up to 200 K. At higher temperatures the intrinsic negative CMR effect becomes visible due to the less pronounced hysteretic low-field MR. Above 150 K the meander track not passing the GB shows comparable MR effects. Thus the artificial GB acts, in this case, as a magnetic field independent series resistor. This indicates loss of magnetic order in the distorted GB region well below the bulk T_C [134]. The low-field MR visible above 150 K in both meanders shows a maximum value of 3% at 175 K. This MR results from a large number of small angle grain boundaries between the individual epitaxial grains. This effect decreases at higher temperatures due to the loss of spin orientation in the individual grains near T_C of the sample. Below 175 K the increasing magnetic domain size will lead to ferromagnetic coupling of a large number of grains in each magnetic domain. Thus only grains at magnetic domain boundaries contribute to the low-field MR. If, at low temperatures, the magnetic domains are much larger than the crystal grain size, the number of not spin aligned grains is negligible and the low-field MR vanishes, as can be seen from the lower curve of Fig. 3.9. At 4.2 K the noise level of the experiment sets an upper limit for the MR of the reference meander of $< 0.05\%$. Within the above description this requires a growth of the magnetic domain size by two orders of magnitude. At the Curie temperature the MR due to small angle grain boundaries vanishes as can be seen by the nonhysteretic MR at 225 K in Fig. 3.8.

3.3.4 Current dependence of magnetoresistance

The influence of the GB on the transport properties is also visible in the current-voltage (I - V) curves of the meanders. In the paramagnetic regime both meanders show a nearly identical ohmic response. Below T_C , the one which crosses the GB is strongly nonlinear in contrast to the ohmic behavior of the reference meander as can be seen in Fig. 3.10 for $T = 4.2$ K in zero field. With increasing bias current,

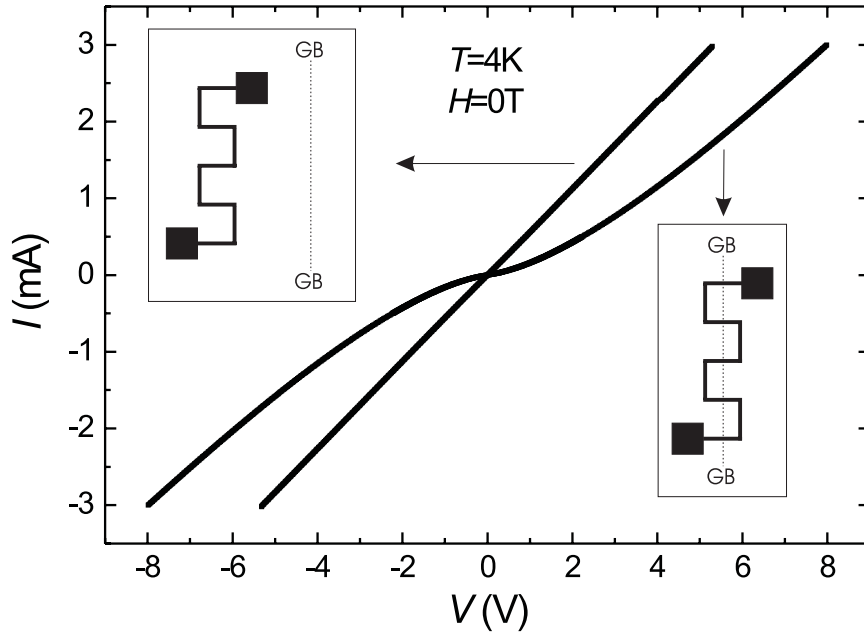


Figure 3.10: I - V curves of the GB and reference meanders in zero field at $T = 4.2$ K. The simplified sketches show only the respective arrangements of the GB and the meanders.

the differential conductivity of the GB meander becomes asymptotic to that of the reference meander. Significant heating effects can be excluded, because the resistance decreases with increasing current while the temperature coefficient of the resistivity is positive.

Nonlinear I - V curves are often taken as an indication for tunneling transport. In ferromagnetic materials the inclusion of spin dependent density of states factors and hysteretic magnetizations on both sides of the tunneling barrier can explain a hysteretic MR. A description of the nonlinear I - V curve shown in Fig. 3.10 with the standard Simmons tunneling model in the parabolic approximation as described above is able to reproduce the data within the linewidth of the figure. In addition to the tunneling parameters one has to take into account in a fitting procedure the resistivity drop in the nondistorted regions. This can be done either as a free parameter or by using the resistivity of the reference meander. One obtains as minimizing parameters a barrier height of $\phi = 0.26$ eV, a width of 2.1 nm, and a resistance of the undistorted region of 1630 Ω . The measured

resistance of the reference meander is $R = 1770 \Omega$. Such a small width of the barrier is not expected in view of the clear visibility of the GB in the SEM scan. In spite of the nearly perfect fit possible for the nonlinear I - V curve of Fig. 3.10, the investigation of direct I - V data gives vanishing weight to the true differential conductivity at zero bias current. Therefore, it is necessary to inspect the differential conductivity shown in Fig. 3.11. For very low bias voltages a

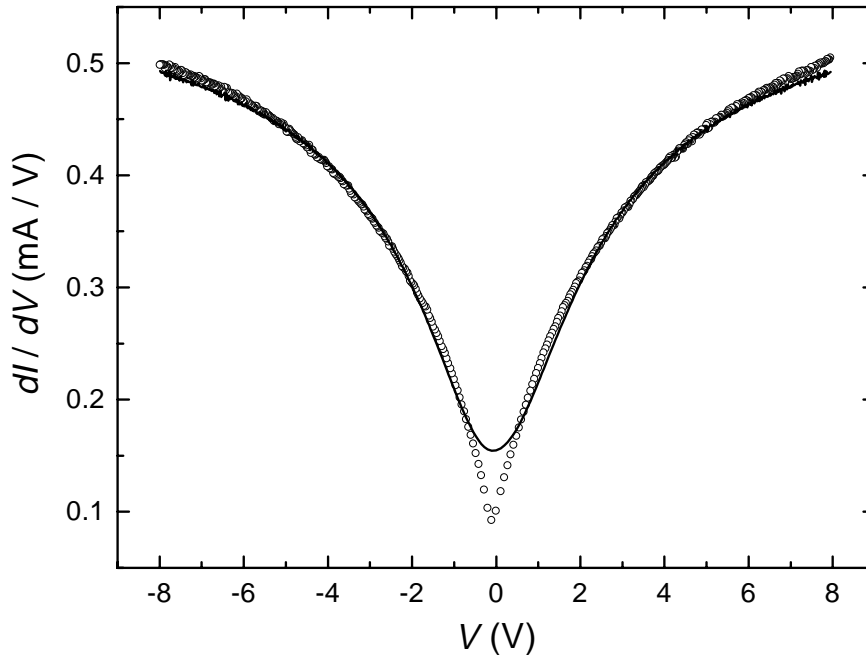


Figure 3.11: Measured (symbols) and calculated (line) differential conductivity of GB meander. The calculation includes a series resistor and a tunneling element described by the Simmons model in the parabolic approximation.

nearly parabolic behavior of the differential conductivity, as predicted by the Simmons model, was found by Steenbeck *et al.* [114]. However, the inclusion of high bias current data in the measurements results in stronger systematic deviations of the Simmons model from the experimental data at low voltages. The differential conductivity sketched in Fig. 3.11 was calculated in the parabolic approximation. In view of the low barrier energy, this is not appropriate at very high bias currents, which correspond to high bias voltages. But using the more general formulas (Eq. 3.4) given by Simmons will even enhance the deviations.

Klein *et al.* [135] assume direct and multistep tunneling via localized states according to Glazman and Matveev [136]. An evaluation according to this model is not possible due to the large contribution of the longitudinal resistivity. Thus it is unclear if charge transport takes place by GB tunneling.

In addition the observed anisotropy of the MR with respect to the magnetic field direction cannot be easily understood within this framework. Therefore, as an alternative mechanism, Evetts *et al.* [134] proposed that the GB does not

act as a tunneling barrier, but as a mesoscale region with distorted magnetic and transport properties. The resistivity of the GB region is assumed to be a function of the GB magnetization, which depends on the effective field acting in the GB region. This interpretation is in agreement with the observed anisotropy. Also the loss of magnetic order in the mesoscale region can naturally occur well below the bulk T_C and will be responsible for the vanishing low-field MR at higher temperatures. The transport mechanisms proposed up to now in the mesoscale region, however, are essentially thermally activated and ohmic. Therefore they cannot simply account for nonlinear I - V curves.

A dependence of the hysteretic low-field MR on the current strength, which is presented in the following, a priori is not expected in either a tunneling model or in a mesoscale transport model.

The dependence of the low-field MR on the transport current on a meander which shows a maximum value MR_{max} of 22% at $T = 4.2$ K was investigated. The applied current range spanned six decades, from 10 nA to 10 mA. It is shown in

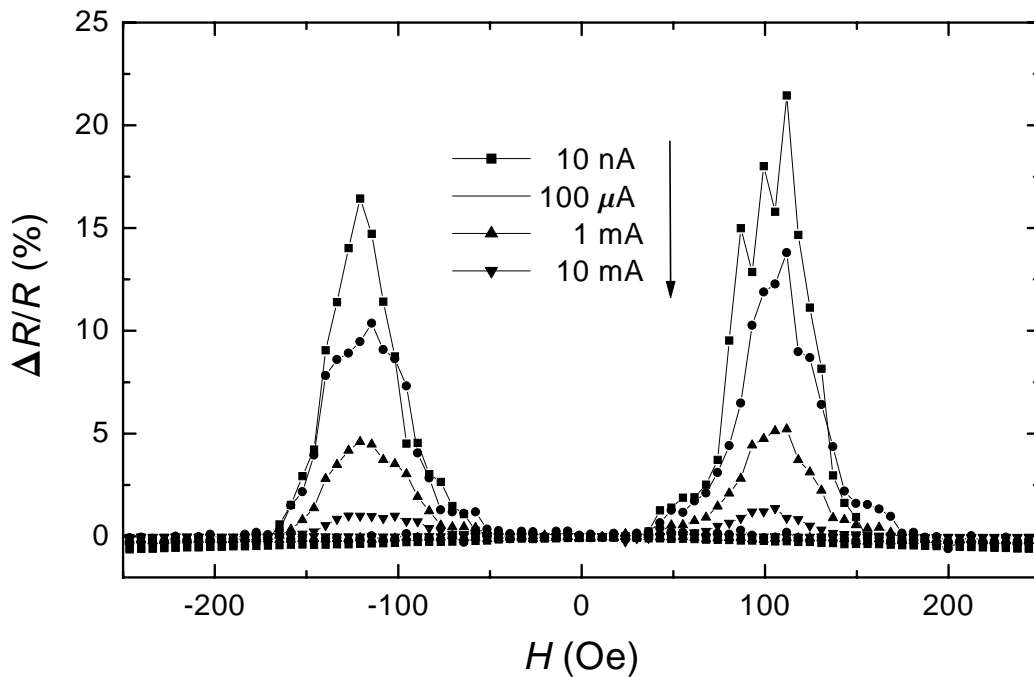


Figure 3.12: *Hysteresis loops of the low-field MR measured with bias currents from 10 nA to 10 mA. For clarity not all measured curves are shown.*

Fig. 3.12 that the width of the hysteresis loops is current independent, while there is a strong current dependence of the height of the MR peaks. The suppression of the MR with current is shown in Fig. 3.13 for bias currents from $\text{MR}_{\text{max}} = 22\%$ for 10 nA to $\text{MR}_{\text{max}} = 1.4\%$ for 10 mA.

A close inspection of the data shows that a current dependence exists also for magnetic field strengths well above the hysteretic region. The decrease of

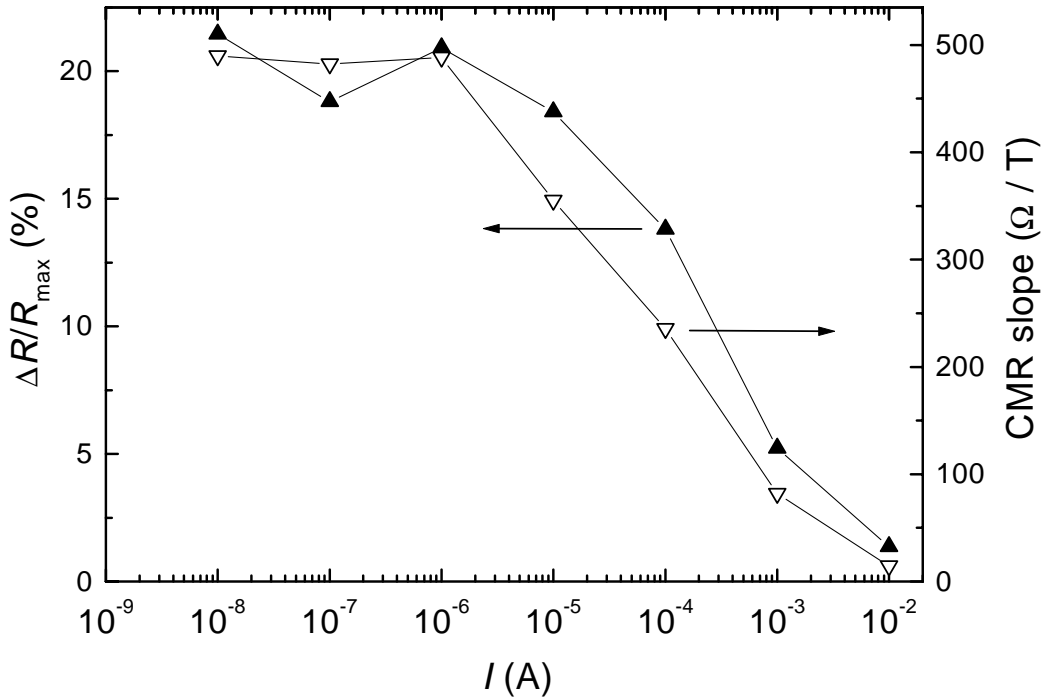


Figure 3.13: Decrease of the low-field MR at the GB with increasing applied current (left axis) and of the respective negative linear high-field CMR slope $dR/d(\mu_0 H)$ (right axis).

this negative CMR of the GB meander with increasing current is shown in an enlarged scale in Fig. 3.14. On the reference meander, no current dependence of the resistivity is observed. The negative linear CMR slope $dR/d(\mu_0 H)$ as function of the current was measured up to 10 T and is also plotted in Fig. 3.13. The close correlation between the CMR suppression and the low-field MR peak suppression with current indicates the same physical origin for both effects in the GB region. Since high bias currents correspond to high bias voltages one possible explanation is, that at high bias voltages a new spin independent channel for charge transport opens. This alternative interpretation of the decrease of the low-field MR with increasing applied voltage was proposed by Gross *et al.* [137, 138] taking into account an increase of inelastic tunneling processes. The inelastic tunneling current does not conserve the spin polarization and hence does not contribute to the MR.

However, due to the intimate relationship between ferromagnetism and spin polarized charge transport in the manganites a different scenario is possible: Due to double exchange, a polarized charge-carrier from the undisturbed region will induce a spin polarization in the distorted region during its transition, i.e. the carrier leaves a trail of localized spins behind, which are more than usually aligned. Each manganese ion will encounter the passage of up to 10^8 polarized carriers per second for the current values used in the experiment. If the spin relaxation

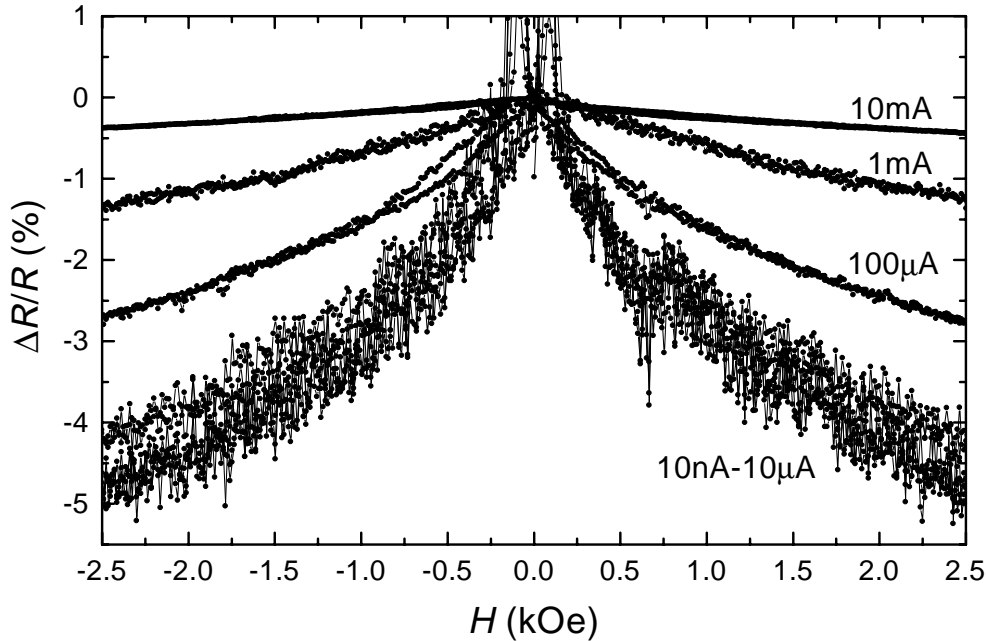


Figure 3.14: *Reversible colossal magnetoresistance of the GB meander as function of applied field. The curves are measured with bias currents from 10 nA to 10 mA. The stronger positive low-field MR shown in Fig. 3.12 leads to the apparent divergence of the data near $H = 0$ in the scaling used here.*

time is much longer than 10^{-8} s then the magnetization induced by charge transport will be nonzero in the average time and a second carrier can use this spin polarized path before the spin relaxation has destroyed the induced order. The existence of electron spin resonance measurements at microwave frequencies in the manganites [139], shows that the relaxation time is longer than $(10 \text{ GHz})^{-1}$, and hence this scenario is imaginable. In the limit of full magnetization of the distorted region, the GB meander resistivity will be indistinguishable from that of the reference meander. This interpretation does not depend on the details of the transport of the charge-carriers from one manganese ion to the next in the mesoscale region, but requires only a hopping probability depending on the respective spin alignment as proposed by several authors [106, 140, 141].

3.4 Summary

In summary spin dependent electron transport in $\text{La}_{0.67}\text{Ca}_{0.33}\text{MnO}_3$ bicrystal devices was successfully demonstrated. Large low-field magnetoresistivities have been achieved and a phenomenological model for the current dependence has been proposed. At the moment the debate concerning the mechanism of the charge transport through the grain boundary is not settled. The GB can act as a tunneling barrier or a mesoscale region. In view of applications, the com-

monly observed strong reduction of the low field MR with temperature is an obstacle. The field sensitivity of the MR is sufficient but due to the increase in spin fluctuations on approaching the Curie temperature the applicability of the $La_{1-x}(Ca,Sr,Ba)_xMnO_3$ compounds at room temperature as magnetic field sensors is questionable.

With conventional ferromagnet-insulator-ferromagnet tunnel junctions, e.g. the trilayer tunnel junctions $Co/Al_2O_3/Ni_{80}Fe_{20}$, values of MR_{max} of more than 20% at ambient temperature have been obtained [142]. Therefore, the design of new materials which are highly spin polarized *and* have a high Curie temperature well above room temperature is required to give an alternative to common materials. Potential materials in the class of oxide compounds are the double-perovskites $A_2BB'O_6$. Recently it was shown by Kobayashi *et al.* [7] that Sr_2FeMoO_6 fulfills the qualifications to be used as a part in new sensors. The preparation of this compound as an epitaxial thin film will be the subject of the following chapter.

Chapter 4

Epitaxial double-perovskite $\text{Sr}_2\text{FeMoO}_6$ thin films

Recently, a large room temperature magnetoresistance (MR) was found by Kobayashi *et al.* [7] in $\text{Sr}_2\text{FeMoO}_6$, an oxide material already investigated in the 1960s [143, 144, 145, 146]. It belongs to the class of double-perovskites ($AA'BB'O_6$) [147]. By band structure calculations it was proposed that this material is half-metallic with an electronic structure where only minority spins are present at the Fermi level. Its advantage compared to the manganites is the higher Curie temperature of 410 K – 450 K. Therefore, a practical device working at ambient temperature can exploit the spin polarization of the carriers as shown in the previous chapter. The goal was to find the parameters to prepare epitaxial $\text{Sr}_2\text{FeMoO}_6$ thin films in the desired quality, i.e. high Curie temperature, metallic transport, high MR and high spin polarization.

4.1 Thin film fabrication

Epitaxial $\text{Sr}_2\text{FeMoO}_6$ thin films were prepared by pulsed laser ablation (Excimer Laser¹, $\lambda = 248$ nm) in an oxygen partial pressure of 10^{-5} Pa – 10^1 Pa or in an argon atmosphere of 10 Pa from a stoichiometric target. The preparation parameters are tabulated in the appendix. A similar second preparation system built up for high-temperature superconducting materials was used which is described in detail in Ref. [148]. The films were grown on (100) SrTiO_3 , (100) MgO , and (10 $\bar{1}$ 2) Al_2O_3 substrates. During deposition the substrate temperature T_D was kept constant with values covering the range from 300°C to 950°C. It strongly influences the crystal structure of the grown thin films. The samples cooled after deposition in a constant background gas pressure. The chemical composition of the films presented here was identical to the nominal composition of the target

¹Lambda Physik LPX301i.

($\text{Sr}_2\text{FeMoO}_{6\pm\delta}$) as measured by energy-dispersive X-ray analysis and Rutherford backscattering on a reference sample on MgO. The film thicknesses were determined with X-ray reflectometry or with a Mireau interferometer [86].

4.2 Half-metallic ground state

Kobayashi *et al.* [7] calculated the electronic structure for $\text{Sr}_2\text{FeMoO}_6$ using the density functional method. In Fig. 4.1 the densities of states for the two spin directions are drawn. The calculation shows that the occupied spin up band mainly consists of Fe 3d electrons hybridized with oxygen 2p states below the Fermi energy. The Mo t_{2g} and e_{2g} spin up bands are found to be above the

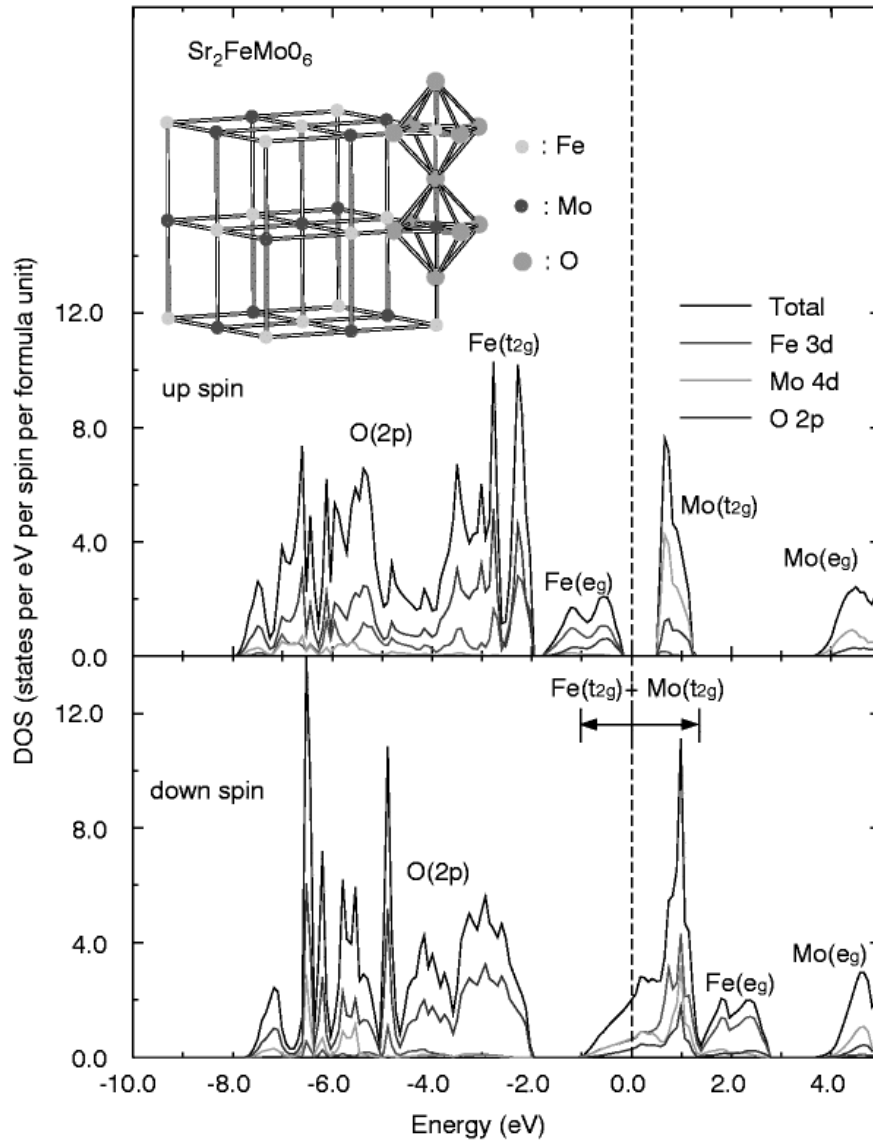


Figure 4.1: Density of states of $\text{Sr}_2\text{FeMoO}_6$ [7].

Fermi level. By contrast, the spin down band consists of occupied oxygen $2p$ states and around the Fermi level a composition of Fe t_{2g} and Mo t_{2g} electrons is visible. This half-metallic nature, i.e. only for one spin direction states exist at the Fermi energy, leads to 100% spin polarization in $\text{Sr}_2\text{FeMoO}_6$. The difference to the nearly half-metallic manganites is that in the case of $\text{Sr}_2\text{FeMoO}_6$ only charge-carriers with spin down in the ground state exist [43]. Recently, a direct experimental evidence for the half-metallic nature in $\text{Sr}_2\text{FeMoO}_6$ was achieved with point contact spectroscopy [149].

4.3 Crystal structure

In the ideal perovskite unit cell ABO_3 (e.g. SrFeO_3), as shown in the first chapter, the large A cation is in the center, the corners are occupied by the smaller B cations, and in the center of the edges the oxygen anions are positioned. The B

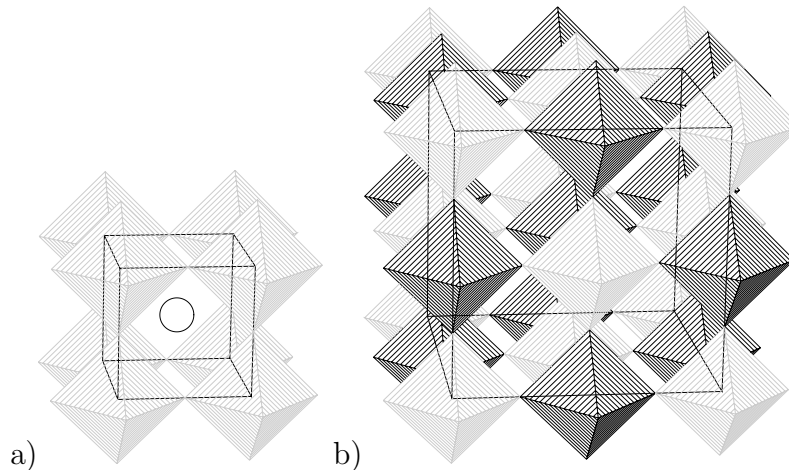


Figure 4.2: a) Corner shared BO_6 octahedra in the simple perovskite ABO_3 . b) Rock-salt arrangement of the BO_6 (black) and $\text{B}'\text{O}_6$ (grey) octahedra in the double-perovskite $\text{A}_2\text{BB}'\text{O}_6$.

cation is octahedrally coordinated as can be seen by the polyhedral representation in Fig. 4.2a. In the double-perovskite compound $\text{A}_2\text{BB}'\text{O}_6$, there are two different atoms B and B' at the corners of the simple perovskite cell. Depending on the metal ion radius, the B and B' ions arrange in a random or ordered fashion. For the latter a layered or rock-salt structure exists. In the case of $\text{Sr}_2\text{FeMoO}_6$ a rock-salt structure is observed as shown in Fig. 4.2b by two different coloured octahedra (FeO_6 and MoO_6).

The crystallographic unit cell is tetragonal $\sqrt{2}a_0 \times \sqrt{2}a_0 \times 2a_0$, where a_0 is the lattice parameter for a single ABO_3 perovskite ($a_0 \approx 4 \text{ \AA}$). A segregation into clusters of compositions SrMoO_3 ($2a_0 = 7.950 \text{ \AA}$) [150] and SrFeO_3 ($2a_0 = 7.738 \text{ \AA}$) [151] should be visible in X-ray diffraction either as severe peak broadening for

small clusters or as peak splitting for large clusters. Neither effect was observed in the prepared thin films. Both deposition temperature T_D and oxygen partial pressure play a crucial role for phase formation and epitaxy. Growth of $\text{Sr}_2\text{FeMoO}_6$ films at oxygen partial pressures above 10 Pa was not possible irrespective of the substrate temperature, but a polycrystalline, yellow, and insulating phase formed. This yellow phase could not be simply identified. Lower oxygen partial pressure during deposition stabilizes the formation of the $\text{Sr}_2\text{FeMoO}_6$ phase. In the following the influence of the substrate temperature on phase formation and epitaxy for a series of films deposited at a very low oxygen partial pressure is reported. This was realized either in flow of pure oxygen at a pressure of 10^{-3} Pa or in flow of pure argon (99.996%) at a total pressure of 10 Pa. At $T_D = 320^\circ\text{C}$ there is a sharp phase boundary for epitaxial thin film growth. For lower temperatures, the same insulating yellow phase was observed. From 320°C up to the highest temperatures achievable with the used heater of 950°C , the samples are single phase, black, and a high degree of $a = b$ and c axis orientation is achieved. The films have a (00 l) orientation perpendicular to the SrTiO_3 (100) plane as can be seen in Fig. 4.3. Annealing these samples in an oxygen partial pressure of more than 10 Pa resulted again in the polycrystalline yellow phase. Already at 320°C perfect epitaxial growth is obtained with rocking curve width $\Delta\omega$ of

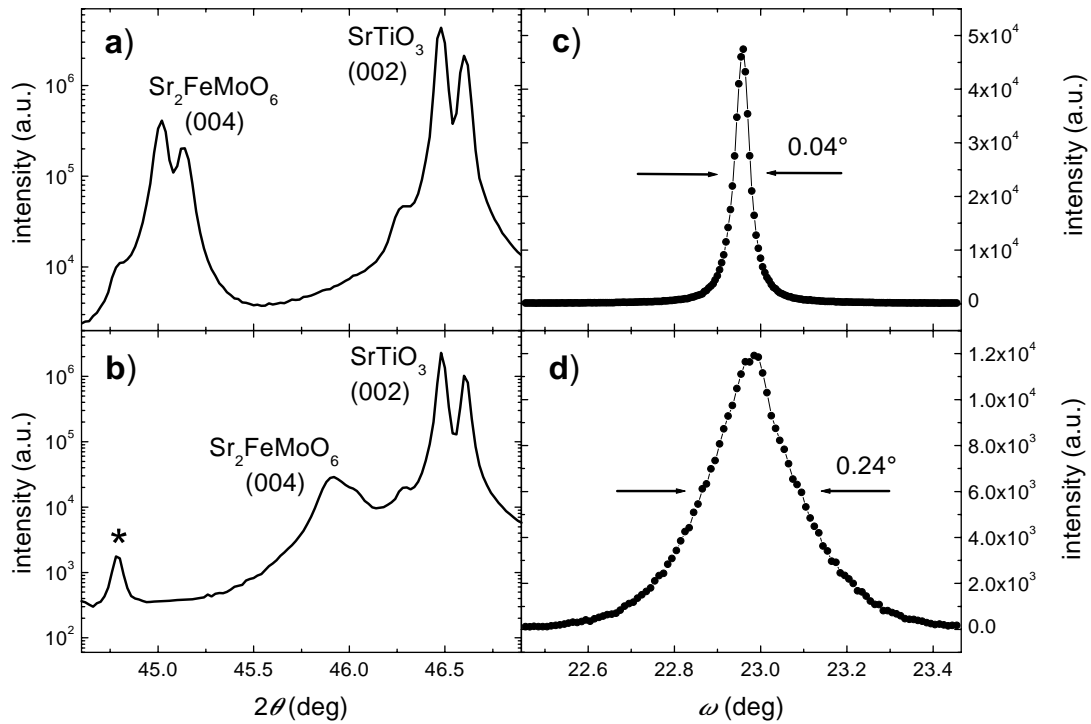


Figure 4.3: a,b) $\theta/2\theta$ -scans showing the (004) reflection peak (Cu $K\alpha$ doublet) of two $\text{Sr}_2\text{FeMoO}_6$ films deposited at low (320°C) and high (950°C) temperatures on SrTiO_3 substrates. The '*' marks a reflection due to the tungsten filament ($L\alpha_2$). c,d) Rocking curves of the appropriate (004) reflections.

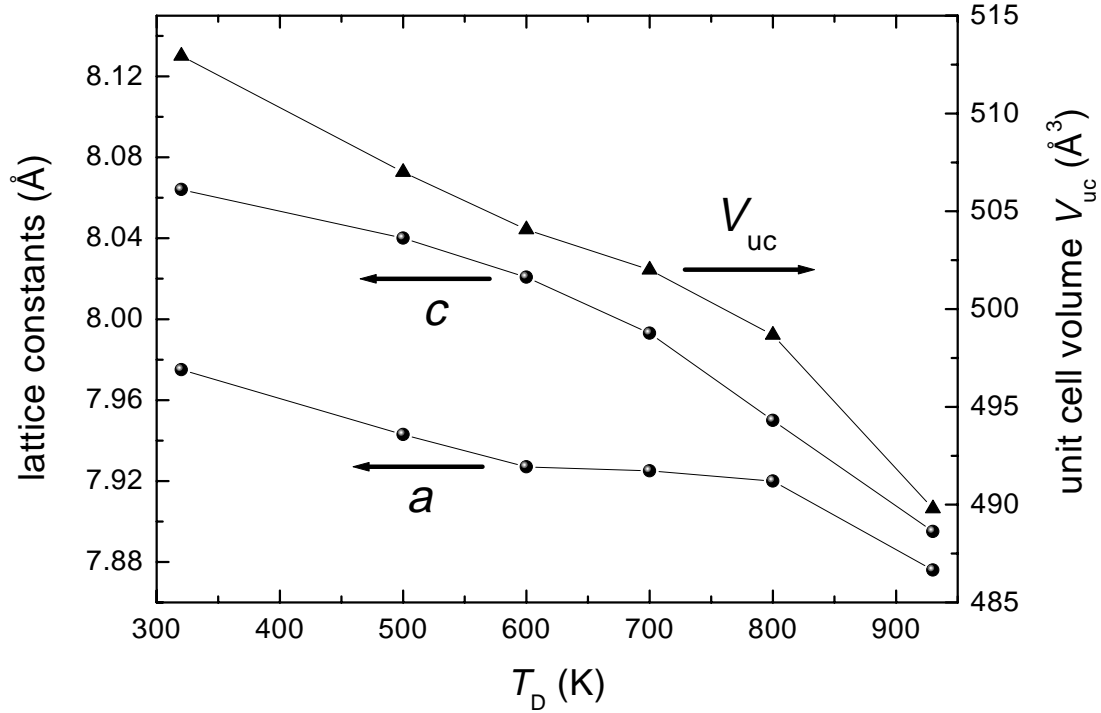


Figure 4.4: Dependence of the lattice constants a and c as well as the unit cell volume V_{uc} on the temperature T_D during deposition.

the (004) reflections below 0.04° . Compared to results gained on other related perovskites as manganites or high-temperature superconductors, this is an astonishingly sharp crossover and low epitaxy temperature. A lowering of the epitaxy temperature will be expected for a perfect in-plane lattice match between film and substrate. However, this is not the case here. The bulk material is cubic with a doubled perovskite unit cell. It was refined in the space group $Fm\bar{3}m$ with a lattice constant of 7.897 \AA [152]. For sample A, prepared at $T_D = 320^\circ\text{C}$, all axes, $a = b$ and c , are elongated to 7.972 \AA and 8.057 \AA , respectively². The lattice mismatch between film and substrate is 2%. The rocking curves remain constant for deposition temperatures up to 900°C . For higher temperatures they broaden to a mosaic spread of 0.23° at 930°C . A detailed investigation together with the temperature dependence of the resistivity will be given in the following section. At $T_D = 930^\circ\text{C}$ one obtains an in-plane lattice constant of 7.876 \AA and an out-of-plane lattice constant of 7.896 \AA . Therefore the unit cell volume V_{uc} of sample B (489.8 \AA^3) is decreased significantly by 4.5% compared to sample A (512.0 \AA^3) and hence is roughly the same as the bulk value (492.5 \AA^3). The detailed dependence of the unit cell volume on temperature during deposition is shown in Fig. 4.4. With a higher T_D the a axis and c axis lengths and therewith

²Although the dimension of the crystallographic unit cell is $\sqrt{2}a_0 \times \sqrt{2}a_0 \times 2a_0$, where a_0 is the lattice parameter for a single ABO_3 perovskite ($a_0 \approx 4 \text{ \AA}$), the larger cell doubled in all directions is used to underline the symmetry of the B, B' rock-salt arrangement.

the unit cell volume decrease continuously.

Investigations of the reciprocal lattice show clear differences in the $\{hkl\}$ reflections (h , k , and l odd) of the two films. They are *present* in sample B, but *absent* in sample A. Intensity in these reflections is generated by the Fe,Mo ordered rock-salt arrangement. The intensity ratio of the (111) and (004) reflection in sample B is close to the estimated value in the tetragonal $I4/mmm$ structure

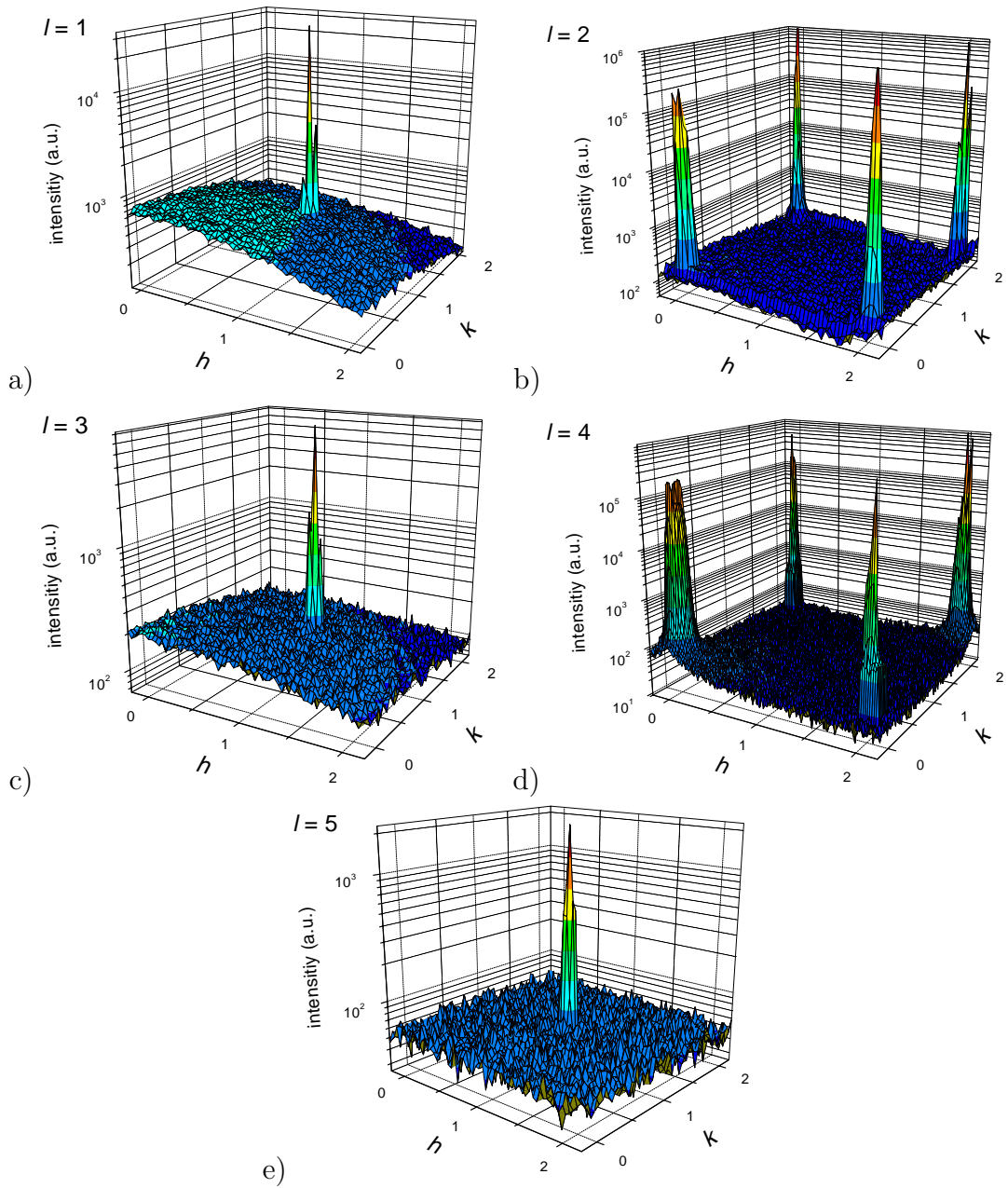
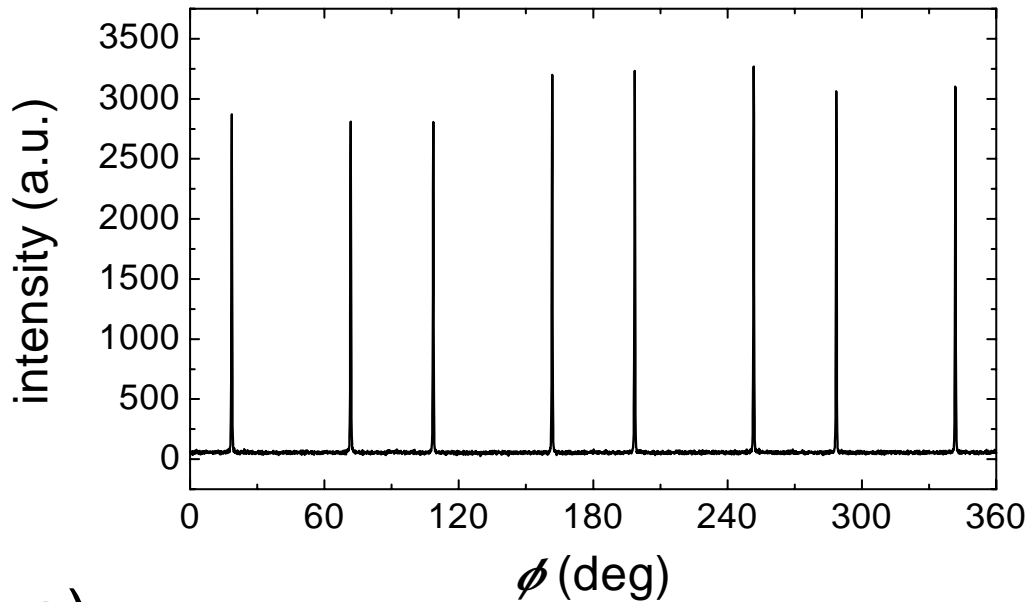
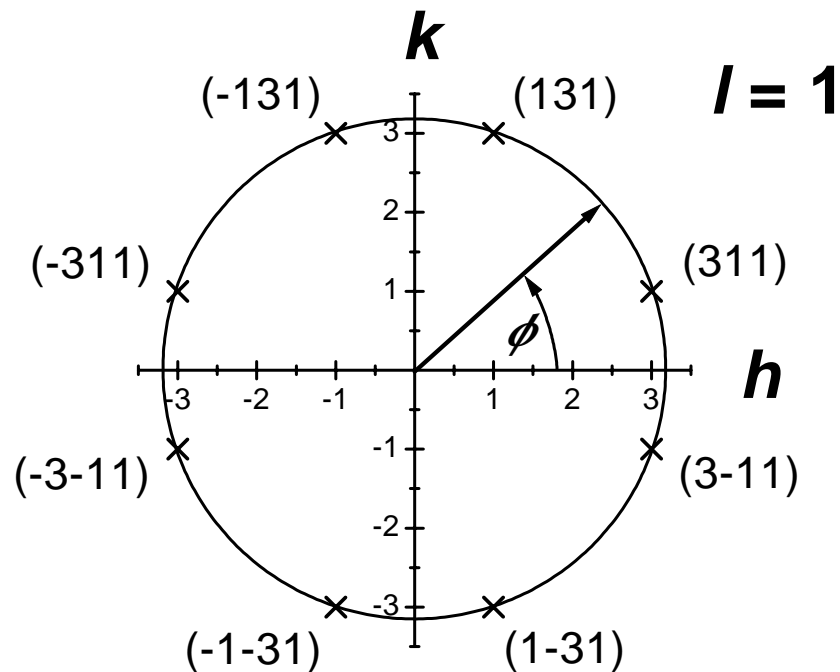


Figure 4.5: hk scans for constant l values of 1,2,3,4, and 5. The reflections with h, k and l odd are due to the rock-salt arrangement of the B, B' ions in the film deposited at 930°C .

found for a $\text{Sr}_2\text{FeMoO}_6$ single crystal [153]. In Fig. 4.5 hk scans (sample B) for constant l values of 1,2,3,4, and 5 are shown. Clearly the (hkl) reflections with h , k , and l odd are visible. In contrast the absence of these reflections in sam-



a)



b)

Figure 4.6: ϕ -scan of the $\text{Sr}_2\text{FeMoO}_6$ $\{311\}$ reflections. Eight reflections leading to a fourfold in-plane symmetry are visible.

ple A indicates random B, B' site occupation accompanied by an enlarged cell volume. The in-plane orientation was further checked by ϕ -scans of the symmetry equivalent $\{111\}$, $\{311\}$, and $\{511\}$ reflections. As expected, the film with perovskite structure grows cube on cube on the SrTiO_3 perovskite substrate with an in-plane angular spread of 0.4° . Due to the fact that h is unequal to k , eight reflections were observed: (311) , (131) , $(\bar{1}31)$, $(\bar{3}11)$, $(\bar{3}\bar{1}1)$, $(\bar{1}\bar{3}1)$, $(1\bar{3}1)$, and $(3\bar{1}1)$ at ϕ values (h direction is $\phi = 0$) of 18.4° , 71.6° , 108.4° , 161.6° , 198.4° , 251.6° , 288.4° , and 341.6° , respectively. The ϕ -scan is shown in Fig. 4.6. The tetragonal symmetry $a = b$ leads to angles between the reflections of 36.8° and 53.2° .

The detailed dependence of the (111) intensity reflection on the substrate temperature during deposition will be discussed in the following section together with the magnetotransport including Hall effect. There it is shown that the differences in the crystal structure come along with respective differences in the transport properties, i.e. a clear structure-property relationship in the double-perovskite $\text{Sr}_2\text{FeMoO}_6$ will be revealed.

To avoid the time-consuming measurements of the (111) reflection with the four-axis X-ray diffractometer thin films of $\text{Sr}_2\text{FeMoO}_6$ were also deposited on SrTiO_3 (111) substrates. As expected $\text{Sr}_2\text{FeMoO}_6$ grows as well (111) oriented and therefore, the (111) intensity reflections could be rapidly investigated with the two-axis X-ray diffractometer in Bragg-Brentano geometry. However, a lower degree of epitaxy compared to the samples on SrTiO_3 (100) was obtained [86] which may arise from the large oxygen diffusion on the SrTiO_3 (111) surface [154]. The rocking curve consists of two components, superimposed is a broad component of 0.31° and a narrow component of 0.04° .

The reference sample on cubic MgO (100) which has a large lattice mismatch grows with two preferred orientations, (001) and (100), i.e. one orientation has the long c axis lying out-of-plane as in the samples on SrTiO_3 and the other orientation has the short a axis perpendicular to the MgO (100) plane (here the tetragonal unit cell $\sqrt{2}a_0 \times \sqrt{2}a_0 \times 2a_0$ is used). Lower epitaxial degree with a mosaic spread of 1° was found. The lattice constants of the a and c axis are 7.95 \AA and 7.97 \AA , respectively.

Depositing the samples on r plane (10 $\bar{1}2$) Al_2O_3 substrates with a hexagonal symmetry, a different growth behavior could be observed. The thin film is twinned with the long c axis lying in-plane and with the short a axis being out-of-plane as for one orientation in the samples on MgO (here the tetragonal unit cell $\sqrt{2}a_0 \times \sqrt{2}a_0 \times 2a_0$ is used). To each other the twins are aligned perpendicular. Therefore, the two twins, T1 and T2 with a twofold symmetry pretend a fourfold in-plane symmetry. A kl scan with $h = 2$ is shown in Fig. 4.7a. Due to the larger lattice mismatch each twin has a broad in-plane angular spread of 9° as can be seen by the ϕ -scan in Fig. 4.7b.

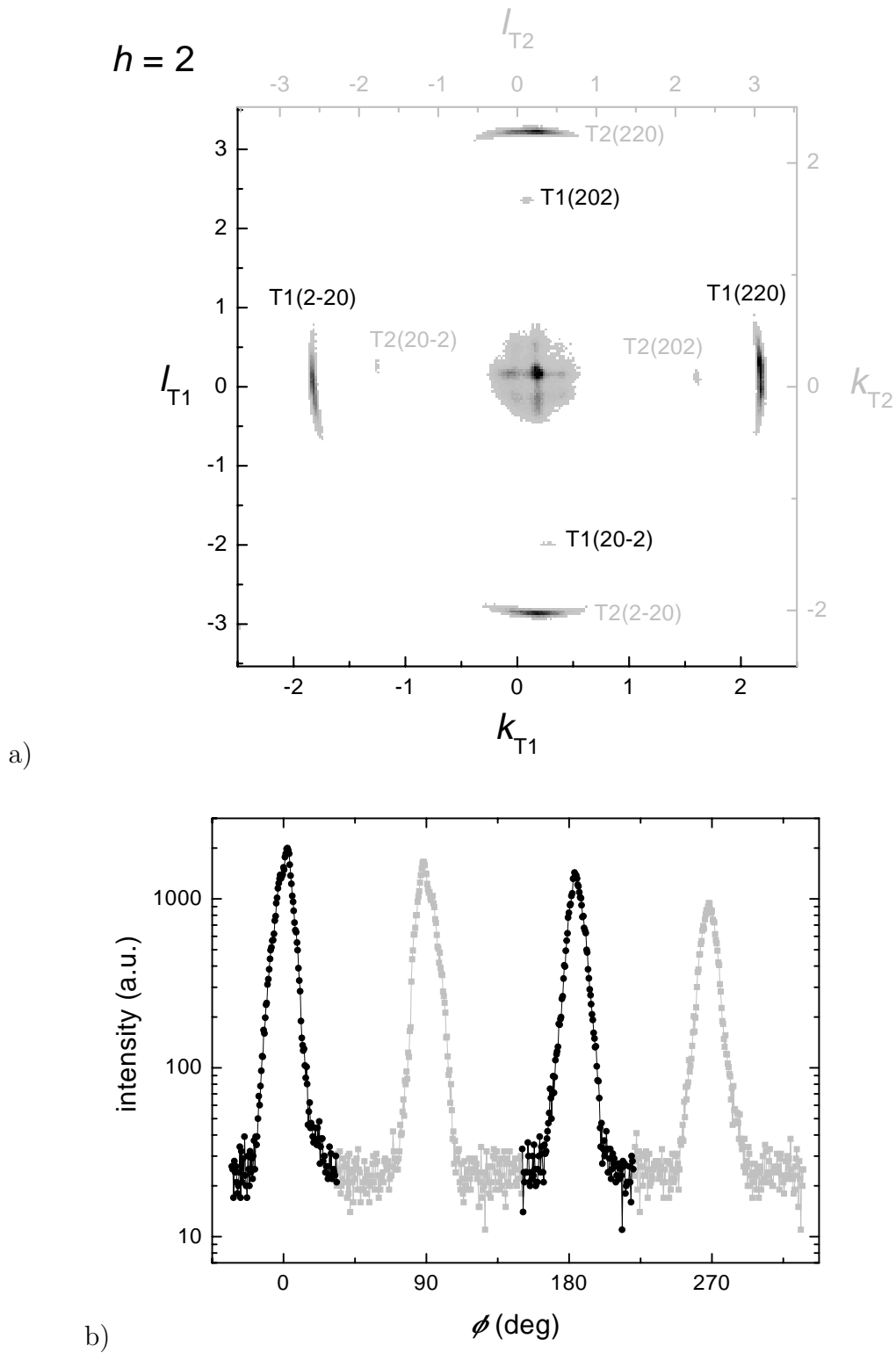


Figure 4.7: a) kl scans for a constant h value of 2. The two twins pretend a fourfold in-plane symmetry. b) ϕ -scan of the $\text{Sr}_2\text{FeMoO}_6$ $\{220\}$ reflections of the two twins, showing a broad mosaic spread.

4.4 Morphology

The surface morphology was studied using scanning electron microscopy (SEM). The difference in crystal structure and in magnetotransport between the samples

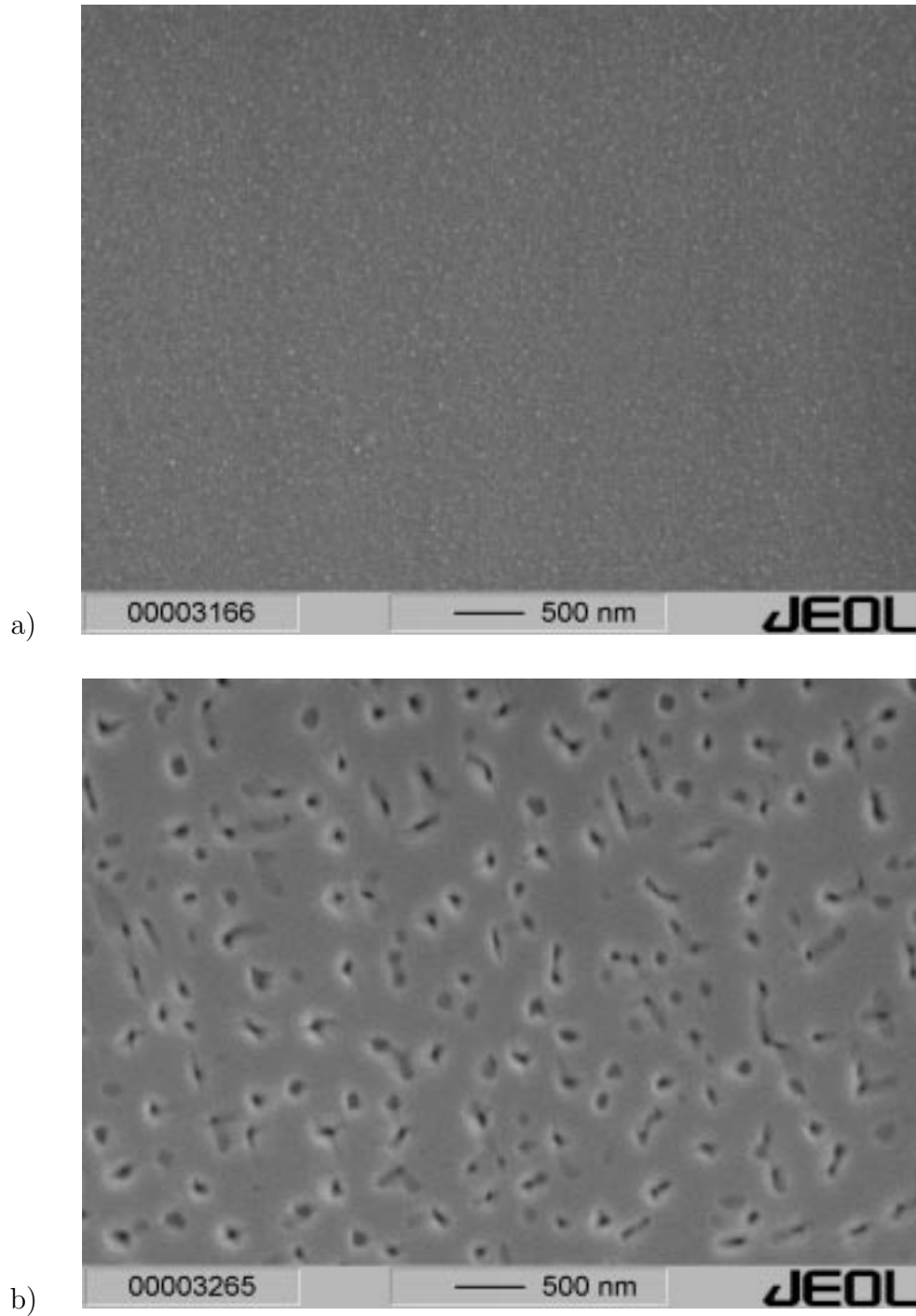


Figure 4.8: a) SEM area scan of sample A ($T_D = 320^\circ\text{C}$). b) SEM area scan of sample B ($T_D = 930^\circ\text{C}$).

deposited at ‘low’ temperatures ($320 \leq T_D \leq 920^\circ\text{C}$) and the samples deposited at ‘high’ temperatures ($T_D = 930^\circ\text{C}$) is also visible in the composition of the surface. Sample A ($T_D = 320^\circ\text{C}$) has a very homogeneous surface with small sizes of the clusters below 20 nm (Fig. 4.8a), whereas sample B ($T_D = 930^\circ\text{C}$) exhibits large clusters with sizes of 100 nm – 250 nm (Fig. 4.8b). This observation is identical to the results of Asano *et al.* [155]. In their publication the large clusters were investigated with energy dispersive X-ray analysis. They are highly strontium deficient with an added degree of deficiency of molybdenum.

4.5 Magnetotransport

By standard photolithographic technique the samples were patterned. With the developer containing water, the films were directly etched because they are not resistant against water. Details of the procedure are tabulated in the appendix.

4.5.1 Longitudinal resistivity

Temperature dependence of the longitudinal resistivity

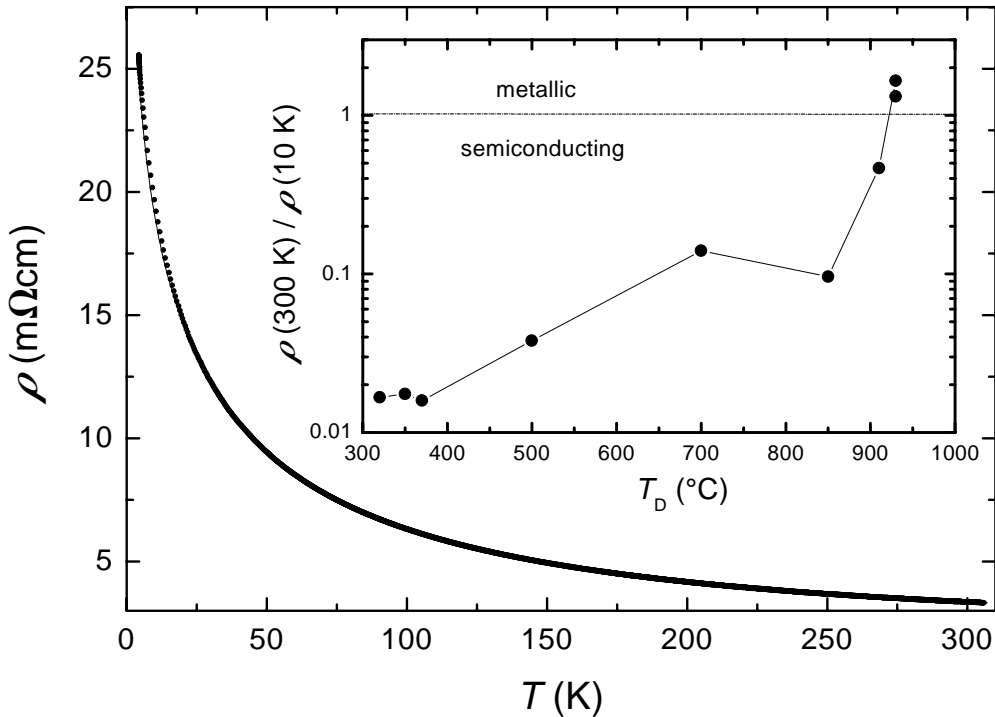


Figure 4.9: Temperature dependence of the resistivity ρ_{xx} in zero field for a sample deposited at $T_D = 700^\circ\text{C}$. The dependence of resistance ratio $\rho(300\text{ K})/\rho(10\text{ K})$ on substrate temperature during deposition is shown in the inset.

The temperature coefficient of the resistivity depends on deposition conditions. For deposition temperatures $320^\circ\text{C} \leq T_D \leq 920^\circ\text{C}$ the temperature coefficient is negative over the whole temperature range, i.e. there is a semiconductorlike behavior³. The zero field resistivity for a sample deposited at $T_D = 700^\circ\text{C}$ is presented in Fig. 4.9. No significant MR was observed in the semiconducting samples. A closer inspection of the temperature dependence of the resistivity reveals a change in conduction mechanism. Below 30 K the resistivity increases strictly logarithmic with falling temperature as shown in Fig. 4.10. This behavior

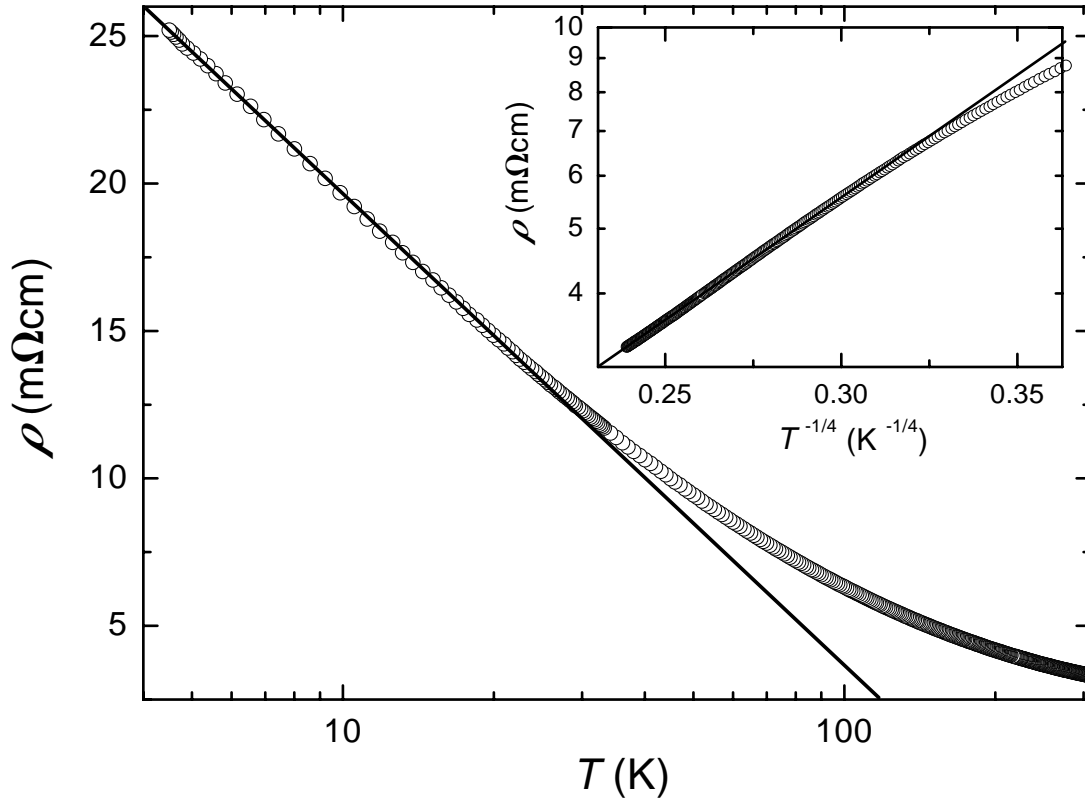


Figure 4.10: Temperature dependence of the resistivity ρ_{xx} in zero field. Below 30 K the resistivity increases logarithmic with falling temperature. The variable range hopping model in the inset describes the data above 100 K. The lines are in both cases a guide to the eye.

is known from Kondo systems, where it results from carrier scattering at uncorrelated magnetic impurities [156]. Above 100 K the temperature dependence of the resistivity is variable range hopping like, described by $\rho \propto \exp((T_0/T)^{0.25})$ with $T_0 = 4900$ K. Using the density of states $N(E_F)$ calculated by Kobayashi *et al.* [7] for $\text{Sr}_2\text{FeMoO}_6$ and the variable range hopping relation $k_B T_0 = 18/(l_0^3 N(E_F))$ for the localization length l_0 an unphysically small value of the temperature de-

³In the following, samples showing a negative temperature coefficient are named semiconducting, neglecting the detailed temperature dependence and the different physics.

pendent hopping length

$$R = \left(\frac{9l_0}{8\pi N(E)k_B T} \right)^{\frac{1}{4}}, \quad (4.1)$$

smaller than the unit cell dimensions, would result [157].

With increasing deposition temperatures, the ratios between the room temperature resistivities and the respective low temperature resistivities ($T = 10$ K) increase, as is shown in the inset of Fig. 4.9. Finally at $T_D = 930^\circ\text{C}$ the ratio is larger than unity, i.e. a metallic behavior occurs. Figure 4.11 presents the resistivity (left axis) of the metallic sample as a function of temperature in zero field and in high magnetic field of 8 T. A positive temperature coefficient exists in

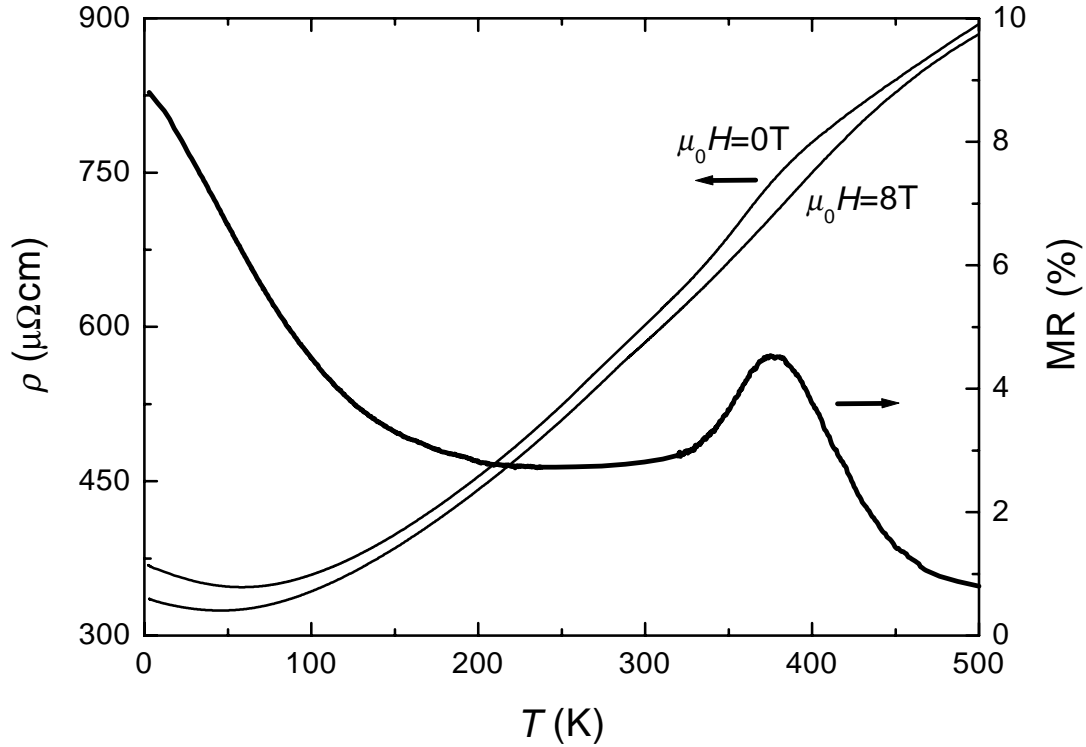


Figure 4.11: Temperature dependent resistivity in zero field and in 8 T magnetic field (left axis) and temperature dependence of negative magnetoresistance defined by $MR = [\rho_0 - \rho(\mu_0 H = 8 \text{ T})]/\rho_0$ (right axis).

the temperature range from 50 K to 500 K. Between 100 K and 300 K, the data can be fitted as in the case of manganites by Eq. 2.1. A negligible weight of the second term was found. This is in agreement with the interpretation that due to the smaller gap between spin up and spin down states in $\text{Sr}_2\text{FeMoO}_6$ than in manganites the electron-magnon scattering ($\propto T^{4.5}$) is less important. Here the emission and absorption of magnons (first term Eq. 2.1) result in the quadratic temperature dependence of the resistivity. Below 50 K, a small increase can be observed with a residual resistivity at 4 K of $360 \mu\Omega\text{cm}$. The magnetic ordering

shows up in the temperature dependence of the resistivity as a small anomaly in the zero field curve near the Curie temperature T_C . The anomaly vanishes by applying a high magnetic field. This temperature dependence is similar to the Sr-doped manganites which have the highest T_C within the manganites as shown in the second chapter.

Magnetoresistance

Two different regimes with a high magnetoresistance MR, here defined by

$$\text{MR} = \frac{\rho_0 - \rho(H)}{\rho_0} \quad (4.2)$$

(right axis in Fig. 4.11) can be distinguished. At very low temperatures, the MR increases supposedly due to grain boundary effects [158]. The peak at 380 K in the neighborhood of the Curie temperature T_C is probably due to the suppression of spin fluctuations by the external magnetic field. These results are similar to those of polycrystalline manganites [73]. The magnetic field dependence of the resistivity below and above (multiplied by a factor 10) T_C is shown in Fig. 4.12. Both curves have opposite curvatures like in Fig. 2.4. The MR is for small fields proportional to H^2 for $T > T_C$ while for $T < T_C$ a nearly linear dependence is found in agreement with the symmetry considerations for the manganites by

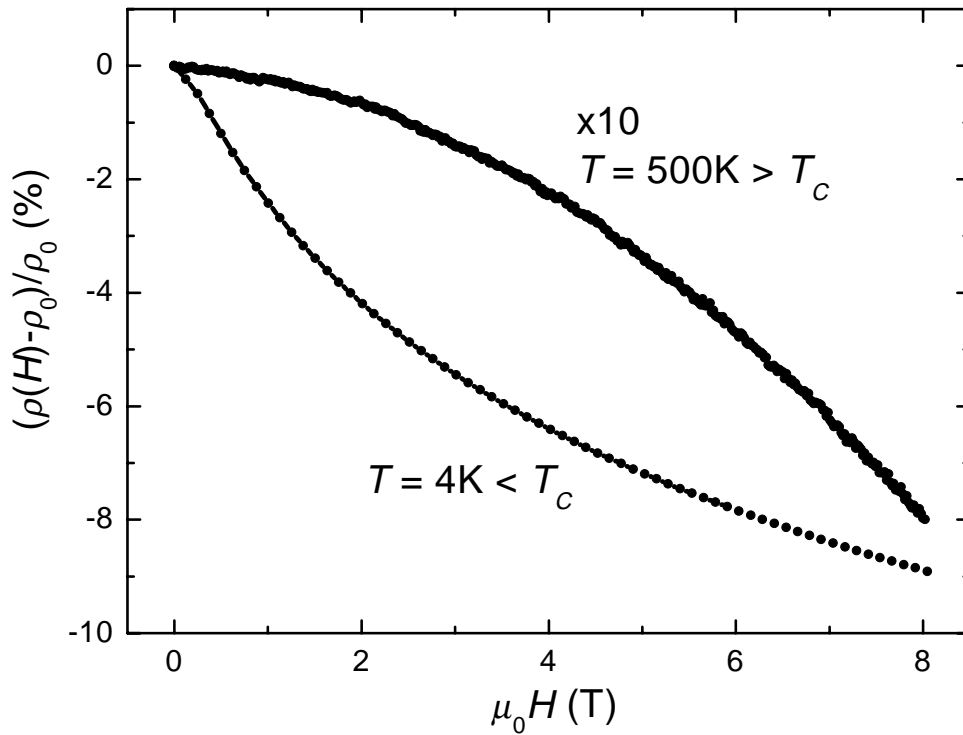


Figure 4.12: High field magnetoresistance below and above (multiplied by a factor 10) the Curie temperature. Both curves have opposite curvatures.

Snyder *et al.* [90]. The absolute value of 8% at 4 K in a field of 8 T is comparable with thin film [159] and single crystal data [153], but much smaller than the values of nearly 40% found in polycrystalline powder [160].

Beside the larger magnitude a sharper low-field response at low temperatures was found in polycrystalline powder. This is an indication that tunneling through grain boundaries increases the MR, the same differences between a single crystal and its polycrystalline counterpart was observed for manganites [110]. The sharp low-field response decreases with increasing temperature, but is still present at room temperature, i.e. a remaining spin polarization exists at room temperature which can be used in real-life device applications.

Structure-property relationship

The transition from a semiconducting behavior to a metallic behavior takes place in a small range of the deposition temperature T_D between 910°C and 930°C. For a sample prepared at $T_D = 910^\circ\text{C}$ in an oxygen partial pressure of 10^{-5} Pa the standard semiconducting behavior is visible, whereas for a thin film deposited at 920°C an anomaly in the temperature dependence of the resistivity between 50 K and 100 K is observed. At 930°C a negative temperature coefficient occurs only down to 200 K again with an anomaly between 50 K and 100 K. An almost fully metallic behavior, a slight upturn in the temperature dependence of the resistivity below 50 K remains, was obtained for the highest temperature achievable of 930°C only in an argon atmosphere of 10 Pa. The temperature dependence of the normalized resistivities for the samples prepared at different substrate temperatures is shown in Fig. 4.13a.

This transition from semiconducting behavior to metallic behavior is simultaneously a transition from disorder to order in the Fe,Mo sublattice, i.e. a clear structure-property relationship exists. The intensity of the rock-salt order reflection (111) normalized to the (004) perovskite reflection which does not depend on the sublattice order increases in the small deposition temperature range from 910°C to 930°C by more than an order of magnitude as can be seen in Fig. 4.13b. At $T_D = 900^\circ\text{C}$ the (111) reflection vanishes.

In summary the deposition temperature strongly influences crystal structure, epitaxial degree, morphology, and magnetotransport. In Fig. 4.14 the dependence of the rocking curve width on T_D , indicating the different regions, is displayed. Below 320°C a yellow, polycrystalline, and insulating phase is formed. At higher deposition temperatures between 320°C and 920°C the prepared samples are black with a high degree of epitaxy. They are semiconducting and exhibit no MR. The Fe,Mo sublattice is disordered. Finally at 930°C the thin films are metallic with a distinctive MR and have a rock-salt Fe,Mo sublattice. In contrast the rocking curve is broadened and on the surface large islands can be observed.

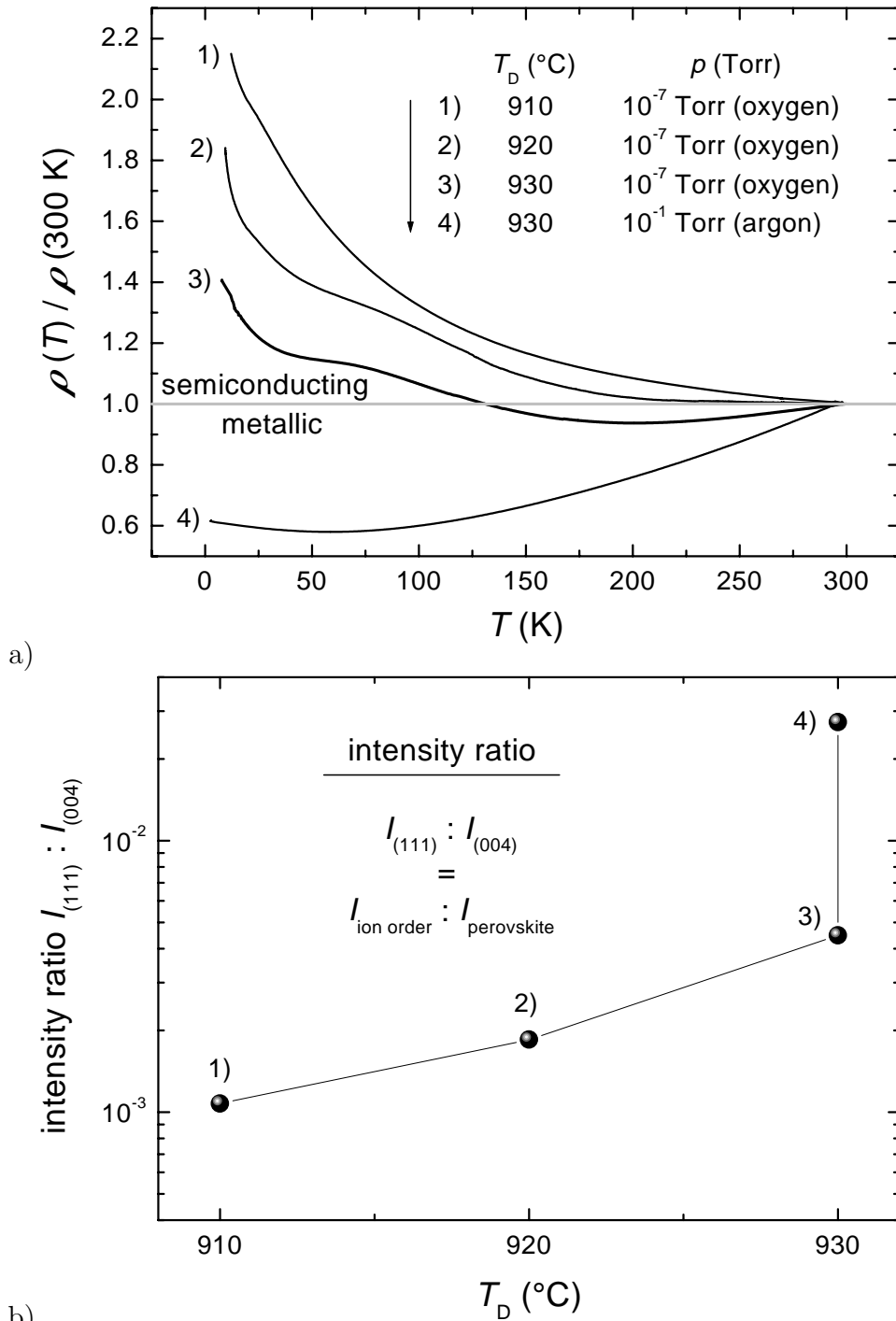


Figure 4.13: a) Temperature dependent resistivity normalized to the room temperature value in zero field from 4 K up to 300 K. In a small range of the deposition temperature T_D the sign of the temperature coefficient of the resistivity changes. Only the sample prepared in an argon atmosphere of 10 Pa exhibits an almost fully metallic behavior.

b) Dependence of the rock-salt order reflection (111) normalized to the (004) perovskite reflection on substrate temperature during deposition. The metallic sample shows the highest intensity for the order reflection.

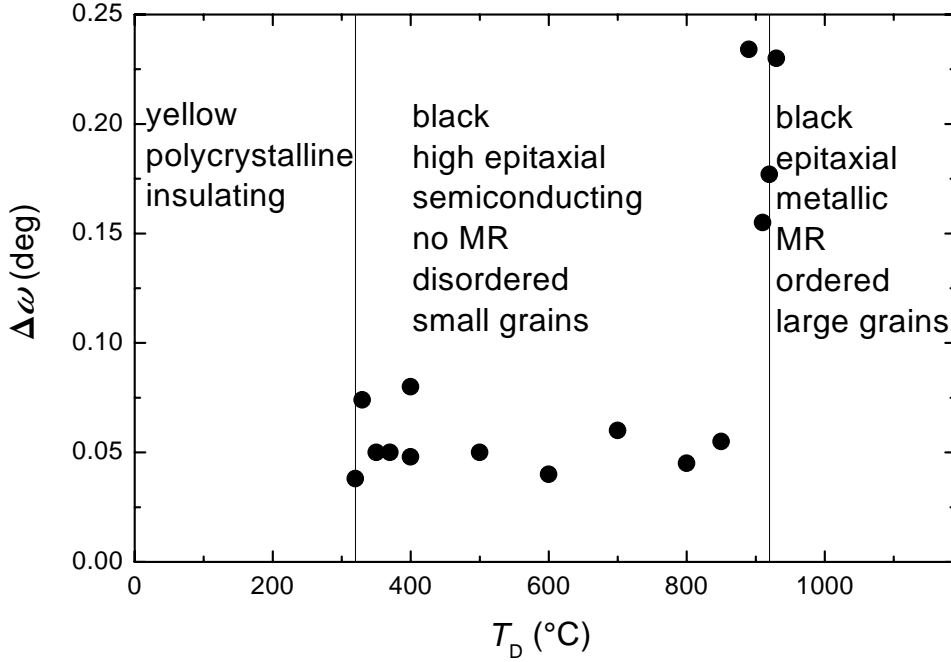
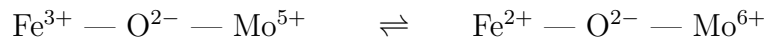


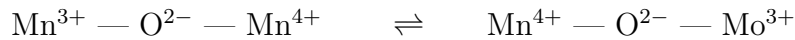
Figure 4.14: Dependence of the rocking curve width $\Delta\omega$ on the substrate temperature during deposition T_D . The different growth regions with its properties are displayed.

4.5.2 Double-exchange-like mechanism

By Mössbauer measurements the valence state of the Fe cation in polycrystalline powder of $\text{Sr}_2\text{FeMoO}_6$ was revealed to be Fe^{3+} [145]. As an intuitive picture for the electronic state, the outer-shell electrons of Fe^{3+} ($S = 5/2, 3d^5, \uparrow, t_{2g}^3 e_g^2$) and Mo^{5+} ($S = 1/2, 4d^1, \downarrow, t_{2g}^1$) cations may be considered as localized or itinerant, respectively. Neutron diffraction studies support the itinerant character of the t_{2g} Mo electron, giving no local magnetic moment at the Mo sites [152]. Recently, evidence for valence fluctuation in $\text{Sr}_2\text{FeMoO}_6$ denoted as $\text{Fe}^{2.5+}$ was found [161]. A charge transfer



similar to the double-exchange mechanism in manganites



through hopping via the oxygen is imaginable. The Fe^{3+} cation contains already five d electrons with spin up and thus hopping of a spin down electron is energetically favoured. Like in the manganites, a strong coupling exists between charge transfer of spin down electrons and ferrimagnetism in $\text{Sr}_2\text{FeMoO}_6$. Therefore, a pronounced MR peak occurs at the Curie temperature due to suppression of spin disorder.

4.5.3 Hall effect

For measuring the Hall effect the same procedure as described in the second chapter in the case of $\text{La}_{0.67}\text{Ca}_{0.33}\text{MnO}_3$ and $\text{La}_{0.67}\text{Sr}_{0.33}\text{MnO}_3$ thin films was applied. The error in the data is smaller than the symbol size. A compilation

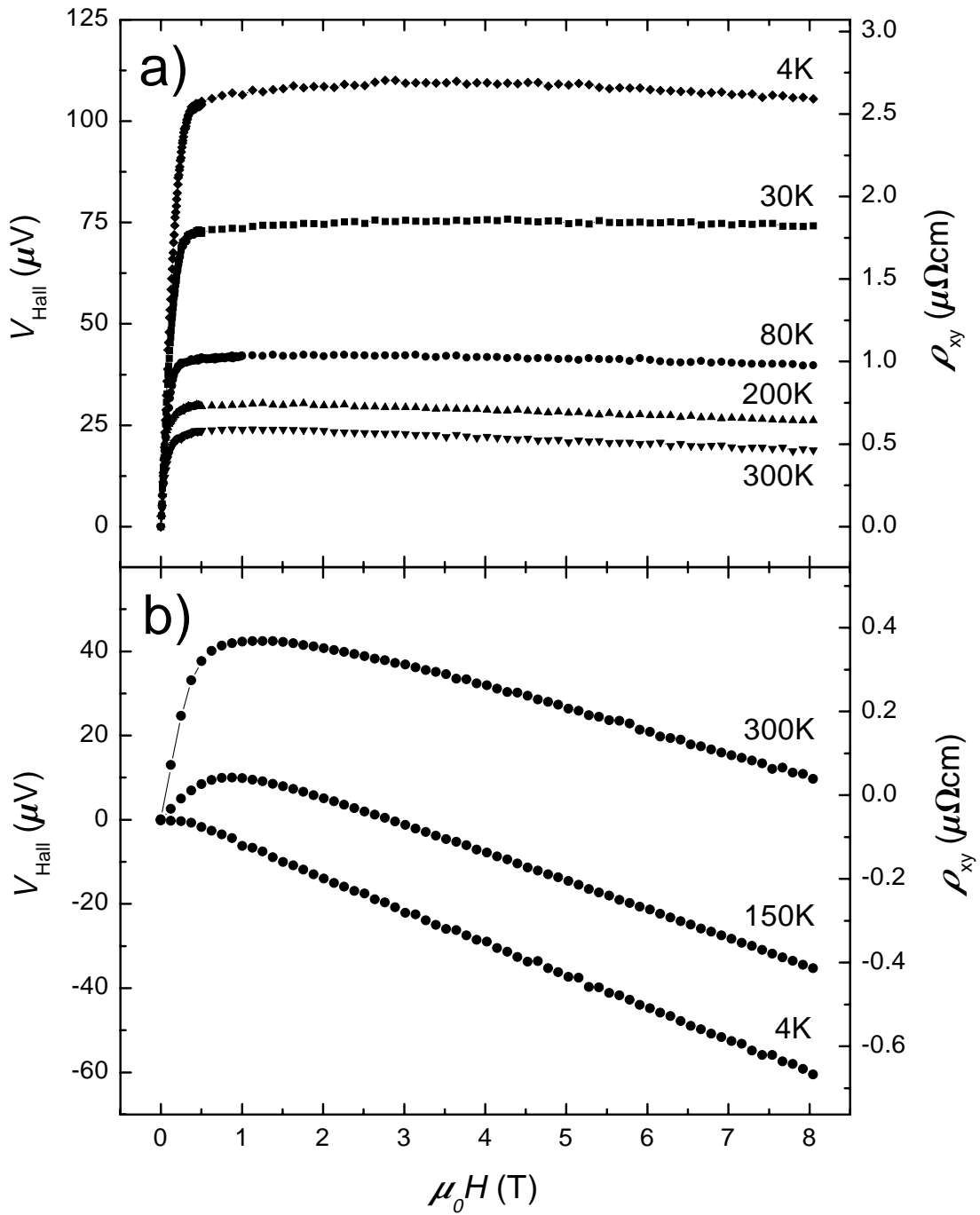


Figure 4.15: Hall voltages V_{Hall} (left axis) and Hall resistivities ρ_{xy} (right axis) as functions of magnetic field at several constant temperatures for a semiconducting sample (part a) and a metallic sample (part b).

of the Hall voltage data $V_{\text{Hall}}(\mu_0 H)$ at several constant temperatures between 4 K and 300 K for a semiconducting sample with $t = 250$ nm (see Fig. 4.9) and a metallic sample with $t = 109$ nm (see Fig. 4.11) is shown in Fig. 4.15a and Fig. 4.15b, respectively.

Semiconducting film

The low magnetoresistivity of the semiconducting samples facilitates at high temperatures the elimination of the parasitic longitudinal part of the Hall voltage and a quantitative analysis of R_A and R_H at constant temperatures. Due to the increasing resistance with decreasing temperature the measurement current was reduced from 1 mA to 100 μA (to avoid heating effects) for the data taken at $T = 4$ K, leading to a worse signal to noise ratio. In low fields, a steep increase of V_{Hall} with increasing field is seen. This part, where the magnetization of the sample changes, is dominated by the anomalous Hall contribution. In the case of $\text{Sr}_2\text{FeMoO}_6$ the anomalous Hall coefficient R_A is holelike, in contrast to the manganites as shown in the second chapter. At 1 T a maximum occurs and at higher fields the data show a linear negative slope. In this high field regime the magnetization of the sample is constant and therefore, according to Eq. 1.5, the ordinary Hall effect becomes visible. This behavior, positive R_A and negative R_H , was also observed in iron and ferromagnetic iron alloys [162]. The linear negative slope $d\rho_{xy}/dB$ indicates an electronlike charge-carrier concentration. The ordinary Hall coefficient⁴ at 300 K is $-1.87 \times 10^{-10} \text{ m}^3/\text{As}$. The value of R_H increases with decreasing temperature to $-1.15 \times 10^{-10} \text{ m}^3/\text{As}$ at 80 K. Because of the worse signal to noise ratio at lower temperatures, an evaluation of the Hall constant was no longer possible. If one assumes that there exists a residual magnetization increase in the high-field regime its anomalous contribution is holelike. Therefore, it will lead to an underestimation of the ordinary Hall coefficient R_H , but *not* to a sign reversal.

Compared to the manganites in the ferromagnetic regime, the temperature coefficients of the resistivity of $\text{Sr}_2\text{FeMoO}_6$ have opposite sign. Due to the fact that longitudinal and transverse resistivity are generated by the same scattering processes the anomalous Hall coefficient increases for $\text{Sr}_2\text{FeMoO}_6$ with decreasing temperature whereas in the metallic manganites the anomalous Hall effect vanishes for very low temperatures. The resistivities ρ_{xx} versus ρ_{xy}^* in a double logarithmic plot show according to Eq. 1.10 a linear slope with $n = 0.77$, indicating skew scattering in the case of $\text{Sr}_2\text{FeMoO}_6$. In manganites, on the other hand, a value of $n = 1.50$ was observed [29].

⁴The Hall coefficient yields in a single band model a charge-carrier concentration of 4.1 electrons per Fe,Mo pair showing that a single band model is not appropriate for this compound and band structure effects dominate the Hall effect.

Metallic film

The Hall voltage V_{Hall} was measured with a current of 1 mA at constant temperatures $T = 4$ K, 150 K, and 300 K in magnetic fields up to 8 T. In comparison to the semiconducting samples the metallic films show the same behavior, electronlike ordinary and holelike anomalous Hall effect, but with one important difference. At low temperatures the anomalous Hall effect nearly vanishes due to the fact that ρ_{xy}^* scales with ρ_{xx} and in these samples the temperature coefficient of the resistivity is positive.

At room temperature an ordinary Hall coefficient of $-6.01 \times 10^{-10} \text{ m}^3/\text{As}$, corresponding to $n_e = 1.3$ electrons per B, B' pair in a single-band model was found. In a simplified picture this is a quite reasonable value taking into consideration that only one itinerant d electron exists, i.e. the d band is nearly empty. With decreasing temperature n_e decreases slightly to 0.9 electrons per formula unit (f.u.) at 4 K. A second metallic sample has almost the same charge-carrier concentration. The zero field mobility at 4 K and 300 K is calculated with these values of the charge-carrier density to $232 \text{ mm}^2/\text{Vs}$ and $100 \text{ mm}^2/\text{Vs}$, respectively. With n and ρ_{xx} one can calculate the mean free path l [163]:

$$l = v_F \cdot \tau = \left(\frac{\hbar (n3\pi^2)^{\frac{1}{3}}}{m} \right) \cdot \left(\frac{m}{ne^2\rho_{xx}} \right) = \frac{\hbar (3\pi^2)^{\frac{1}{3}}}{n^{\frac{2}{3}}e^2\rho_{xx}}. \quad (4.3)$$

With respect to the one band model, reasonable values of 11.1 \AA and 4.6 \AA were found for the mean free path at 4 K and 300 K, respectively. The values gained from the metallic sample are similar to single crystal data by Tomioka *et al.* [153].

At room temperature an anomalous Hall coefficient of $R_A = 1.56 \times 10^{-8} \text{ m}^3/\text{As}$ was found which nearly vanishes for the metallic $\text{Sr}_2\text{FeMoO}_6$ thin films at very low temperatures ($R_A(T = 4\text{K}) = 3.69 \times 10^{-10} \text{ m}^3/\text{As}$). If one assumes magnetic scattering to be important at low temperatures, the vanishing (nonvanishing) anomalous Hall effect may be an indication to an undistorted (distorted) ferrimagnetic state in the metallic (semiconducting) films [164, 165].

4.6 Magnetization

The differences in crystal structure and magnetotransport should also be visible in the magnetic properties. As mentioned before, different Mössbauer measurements were reported by several groups [145, 161, 166]. Valence states of the Fe cation of Fe^{3+} and a mixture of Fe^{2+} and Fe^{3+} were detected. In an ideal ferrimagnetic structure of $\text{Fe}^{3+}\text{Mo}^{5+}$ and $\text{Fe}^{2+}\text{Mo}^{6+}$ occupying in an alternating way the B sites (...Fe — O — Mo — O — Fe — O — Mo — O...) a magnetic moment M_{Sat} of $4 \mu_B/\text{f.u.}$ is expected in both cases, i.e. magnetization measurements alone cannot distinguish the $\text{Fe}^{3+}\text{Mo}^{5+}$ configuration from the $\text{Fe}^{2+}\text{Mo}^{6+}$ configuration.

With a SQUID magnetometer, the magnetic properties were determined. The sample deposited at $T_D = 320^\circ\text{C}$ shows a reduced saturation magnetization of $1 \mu_B/\text{f.u.}$ in comparison to the ideal value as can be seen by the hysteresis curve measured at $T = 10 \text{ K}$ in Fig. 4.16a. Since antiferromagnetic Fe — O — Fe bonds

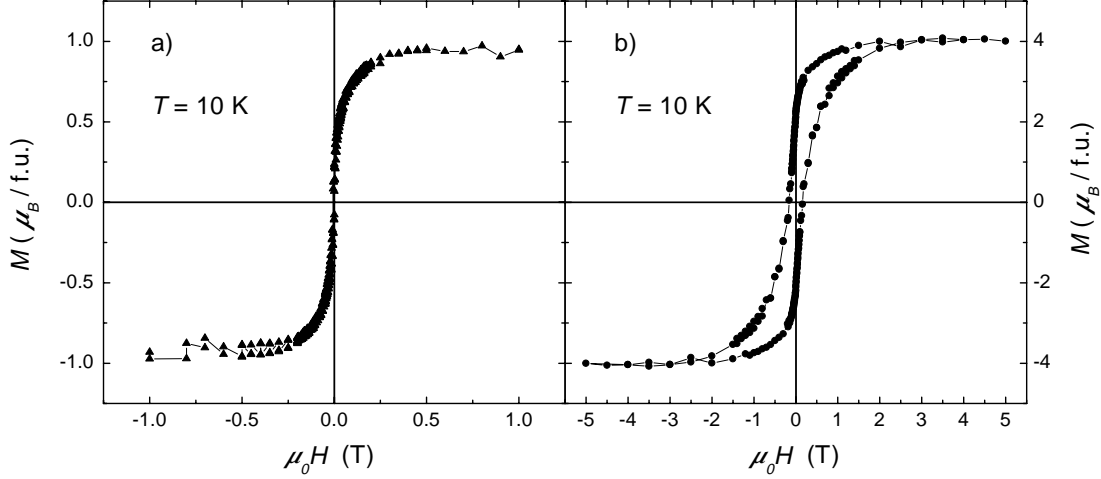


Figure 4.16: Magnetic hysteresis loops for $\text{Sr}_2\text{FeMoO}_6$ thin films. a) from -1 T to 1 T at 10 K for the semiconducting sample deposited at low temperatures. b) from -5 T to 5 T at 10 K for the metallic sample deposited at high temperatures. The saturation magnetization M_{Sat} in the semiconducting sample is strongly reduced in comparison to the metallic sample which exhibits a value of M_{Sat} of $4 \mu_B/\text{f.u.}$ expected from theory. In both figures a linear diamagnetic background from the substrate was subtracted from the raw data.

reduce the magnetic moment of the films [167], the reduced magnetic moment is in conformity with the X-ray diffraction measurements. They revealed a random sublattice, i.e. adjacent Fe cations directly connected via oxygen exist (see p. 67).

The metallic single crystal investigated by Tomioka *et al.* [153] has as well a reduced magnetic moment of $3.2 \mu_B/\text{f.u.}$ and a similar temperature dependence of the resistivity in comparison to the metallic thin films. However, only in the metallic thin films the expected value for the magnetic moment of $4 \mu_B/\text{f.u.}$ was found as shown in Fig. 4.16b. The residual resistivities of the single crystal ($280 \mu\Omega\text{cm}$) and the metallic thin film ($360 \mu\Omega\text{cm}$) are comparable whereas the anomalous Hall coefficients differ by two orders of magnitude, $R_A(T=5 \text{ K}) = 1.20 \times 10^{-8} \text{ m}^3/\text{As}$ and $R_A(T=4 \text{ K}) = 3.69 \times 10^{-10} \text{ m}^3/\text{As}$ for the single crystal and the thin film, respectively.

This result clearly shows that a *distorted* ferrimagnetic state exists only in the $\text{Sr}_2\text{FeMoO}_6$ single crystal [164]. The $\text{Sr}_2\text{FeMoO}_6$ thin film exhibits an *undistorted* ferrimagnetic state, corroborated by the ideal saturation magnetization in accordance with X-ray diffraction on the one hand (see Fig. 4.5) and by the nearly vanishing anomalous Hall effect on the other hand (see Fig. 4.15b).

The effect of disorder in $\text{Sr}_2\text{FeMoO}_6$ was also observed in Mössbauer spectra [160]. Recently, identical hysteresis curves with $M_{\text{Sat}} = 4 \mu_{\text{B}}/\text{f.u.}$ were measured for metallic thin films prepared by off-axis magnetron sputtering [168].

4.7 Summary

In summary epitaxial $\text{Sr}_2\text{FeMoO}_6$ thin films were prepared by pulsed laser deposition. The influence of the substrate temperature during deposition T_{D} on crystal structure and magnetotransport was investigated in detail. Already for $T_{\text{D}} = 320^\circ\text{C}$ epitaxial growth is achieved. Depending on T_{D} a strong variation in cell volume and degree of order of the B, B' site occupation, resulting in metallic or semiconducting behavior of the resistivity, was found.

Disorder in the sublattice of the semiconducting sample is expected to be detrimental to the half-metallic nature, giving rise to finite spin up and spin down densities at the Fermi energy, destroying the half-metallic state. No magnetoresistance was observed. For the metallic samples, on the other hand, a negative magnetoresistance with a maximum in the neighborhood of the Curie temperature was observed. The magnetic moment of the samples prepared in this work is for the first time equal to the expected value for a ferrimagnetic arrangement of the Fe and Mo cations. A long-range ordering of FeO_6 and MoO_6 octahedra exists.

At low temperatures the anomalous Hall effect vanishes, indicating a low

Table 4.1: *Differences in physical properties of sample A (semiconducting) and sample B (metallic).*

Sample	A	B
T_{D} ($^\circ\text{C}$)	320	930
a, b axes (\AA)	7.972	7.876
c axis (\AA)	8.057	7.896
cell volume (\AA^3)	512.045	489.800
(111) reflection	absent	present
surface	clusters absent	clusters present
$\rho(300 \text{ K})/\rho(10 \text{ K})$	$\ll 1$	> 1
negative MR	absent	present
$R_H(300 \text{ K})$ ($10^{-10} \text{ m}^3/\text{As}$)	-1.87	-6.01
$R_A(4 \text{ K})$ ($10^{-10} \text{ m}^3/\text{As}$)	156	3.69
$M_{\text{Sat}}^{\text{exp}}/M_{\text{Sat}}^{\text{theo}}$	0.25	1

degree of magnetic and nonmagnetic scattering. This was up to now not realized in epitaxial thin films and single crystals. The ordinary and anomalous Hall coefficients are negative and positive, respectively. Both coefficients have reversed sign compared to the colossal magnetoresistive manganites. A charge-carrier concentration of 1.3 electrons per f.u. at room temperature was obtained in the metallic sample.

In table 4.1 crystal structure, magnetotransport, and magnetization data of the samples A and B are listed to emphasize the differences between low temperature deposited $\text{Sr}_2\text{FeMoO}_6$ thin films and their high temperature deposited counterparts.

The next goal for the future is to exploit the remaining spin polarization at ambient temperature in a device. It is worth mentioning that a direct experimental proof of a high spin polarization in the $\text{Sr}_2\text{FeMoO}_6$ thin films prepared in this work was achieved [149]. The integration of $\text{Sr}_2\text{FeMoO}_6$ in a tunnel junction or deposition of $\text{Sr}_2\text{FeMoO}_6$ on bicrystal substrates is very promising and is under current investigations in the research group. Due to the higher Curie temperature above room temperature the device should exhibit a large MR in low fields even at ambient temperature. In the following chapter it will be shown that within the class of the double-perovskites there exist compounds with still higher Curie temperatures above 500 K.

Chapter 5

Investigation of double-perovskite $\text{Ca}_2\text{FeReO}_6$

High Curie temperatures are required if magnetic tunnel junction devices which rely on spin polarized tunneling in half-metallic oxides are to operate at ambient temperature. Up to now the Curie temperature T_C is below 400 K which is a drawback for many device applications where an operating temperature range of about 230 K – 400 K (-40°C – 120°C) is required. No combination of cation substitution and nonstoichiometry has succeeded in raising T_C for the mixed-valence manganites above 390 K, and there are no reports that the Curie point of CrO_2 can be raised above 400 K.

More than 300 compounds with double-perovskite structures have been synthesized up to now [147]. Among them, $A_2\text{FeMoO}_6$ and $A_2\text{FeReO}_6$ ($A = \text{Ca}, \text{Sr},$ and Ba) are known to be ferrimagnetic [169]. They are the most prospective candidates for utilization as electrodes for spin valve and magnetic tunnel junction devices due to their high Curie temperatures of more than 400 K for $\text{Sr}_2\text{FeMoO}_6$ (discussed in the previous chapter) and more than 500 K for $\text{Ca}_2\text{FeReO}_6$. Their properties must be understood before these materials can be used with confidence in applications. The double-perovskite $\text{Ca}_2\text{FeReO}_6$ was characterized already more than 30 years ago [170], but only the crystal structure and the Curie temperature were determined at that time.

In this chapter a detailed study of the compound $\text{Ca}_2\text{FeReO}_6$ by X-ray diffraction, neutron diffraction, Mössbauer, magnetotransport, and magnetization measurements will be given.

5.1 Powder preparation and experiment

The compound $\text{Ca}_2\text{FeReO}_6$ was synthesized by a solid-state reaction from CaO (Alfa, 99.95%), ReO_3 (Alfa, 99.9%), Fe (Alfa, 99.998%) and Fe_2O_3 (Alfa, 99.99%)

using the stoichiometric ratio of $2:1:\frac{1}{3}:\frac{1}{3}$ respectively and batches of an overall mass of 2 g. The well grained and mixed educts were transferred into a corundum container and sealed in an evacuated quartz tube ($p = 5 \times 10^{-3}$ Pa). The tube was heated to 1173 K at a rate of 1 K/min and held at this temperature for 48 hours. After cooling the sample to room temperature at a rate of 5 K/min the sample was reground and resealed. The resealed sample was annealed at 1173 K for 14 days and then quenched with liquid nitrogen. This method yielded a black polycrystalline product.

X-ray diffraction was performed at room temperature using a Philips X'Pert MPD diffractometer in Bragg-Brentano geometry. The instrument works with Cu $K\alpha$ radiation ($\lambda = 1.5418$ Å).

At the Institut Laue Langevin in Grenoble the neutron powder diffraction data were collected on the high-resolution two-axis diffractometer D2B (see p. 17) with the powder sample (10 g) placed in a cylindrical vanadium can inside a cryofurnace ($T = 1.5$ K – 600 K). A wavelength of $\lambda = 1.594$ Å over an angular range from 0° to 162° and collimators of 10' were used. The measurements were performed on warming at several fixed temperatures of 2 K, 100 K, 200 K, 300 K, 400 K, 444 K, 524 K, and 548 K. The X-ray and neutron diffraction patterns were refined by the Rietveld method using the program FULLPROF [72]. For the line shape a pseudo-Voigt function was selected. All Bragg peaks could be identified and therefore no regions were excluded in the refinement. The following parameters were refined: zero point error, background coefficients, atomic coordinates, isotropic temperature factors, profile shape parameter, half-width parameters, asymmetry parameters, scale factors, lattice constants, β angle, and magnitudes of the Fe and Re magnetic moments. Further details are presented in the appendix.

The magnetic properties as AC magnetic susceptibility and DC magnetic moment were determined with a Lake Shore 7000 magnetometer and a S.H.E. SQUID magnetometer, respectively.

Mössbauer spectra were recorded at 4.2 K and 293 K in two different apparatuses.¹ Each spectrum has been taken for one week. With a constant acceleration spectrometer, using a 1024 channel analyser in the time mode, Mössbauer transmission spectra were taken. For the 4.2 K measurement a Na(Tl)I scintillator was used while the 293 K measurement was done with a proportional counter. A 50 mCi ^{57}Co source in a rhodium matrix at room temperature was used in both cases. The Fe spectra were fitted with the Mössbauer analysis program *effi* [171].

By the standard four-point technique the temperature dependence of the resistivity was measured in a standard cryostat with variable temperature insert. The applied magnetic field was generated by a 15 T superconducting magnet.

¹The measurements were performed in the department of chemistry in the research group of Prof. Gütlich by Markus Waldeck and Franz Renz.

5.2 Crystal structure

5.2.1 Neutron diffraction

Over 300 compounds are known in the class of double-perovskites ($AA'BB'O_6$) [147]. The B, B' ions arrange in three different manners, rock-salt, random and in rare cases layered as sketched in Fig. 5.1 by black and grey octahedra indicating

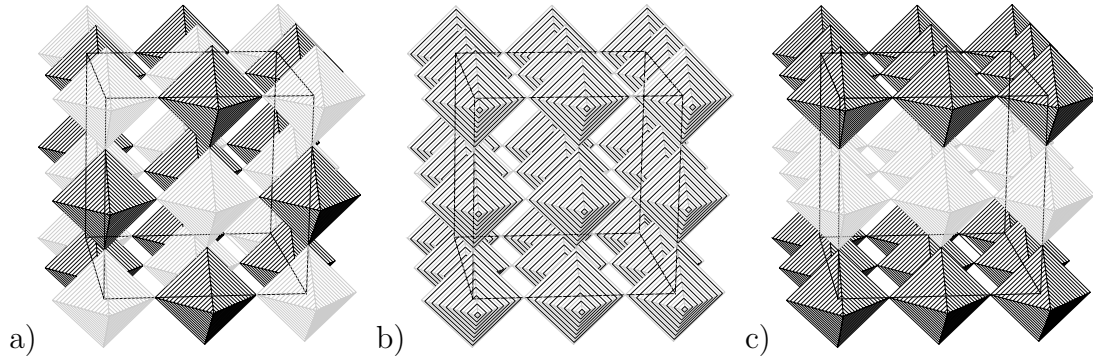


Figure 5.1: The BO_6 (black) and $B'O_6$ (grey) corner-shared octahedra in a double-perovskite $AA'BB'O_6$ arrange in three different manners: (a) rock-salt, (b) random and (c) layered. The two possible occupations in the random structure are indicated by black and grey striped octahedra.

different occupations B and B' , respectively. Which type of configuration exists, depends on the charge, size, electronic configuration, and B/B' size ratio of the involved ions. In the case of $\text{Ca}_2\text{FeReO}_6$ the charge difference is $2e$ (Fe^{3+} , Re^{5+} , see Mössbauer measurements below) and the ionic radius difference Δr is 0.065 \AA ($r(\text{Fe}^{3+}) = 0.785 \text{ \AA}$, $r(\text{Re}^{5+}) = 0.72 \text{ \AA}$) leading to a rock-salt B, B' sublattice [172]. The unit cell for rock-salt arrangement can be derived either from a cubic $2a_0$ or a monoclinic ($\sqrt{2}a_0 \times \sqrt{2}a_0 \times 2a_0$) cell, where a_0 is the lattice parameter for the standard cubic perovskite ABO_3 ($a_0 \approx 4 \text{ \AA}$). The monoclinic cell is favoured if the tolerance factor t defined in Eq. 5.1 (see also Eq. 1.1) is less than unity.

$$t = \frac{\frac{r_A + r_{A'}}{2} + r_O}{\sqrt{2} \left(\frac{r_B + r_{B'}}{2} + r_O \right)} \quad (5.1)$$

The cation order is revealed in the cubic case by the presence of (hkl) reflections with $h, k, l = 2n + 1$ or in the monoclinic case by $(0kl)$ reflections with $k = 2n + 1$, respectively [147]. For $\text{Ca}_2\text{FeReO}_6$ due to the low tolerance factor of $t = 0.97$ a monoclinic unit cell is expected (ionic radii² from Ref. [172]). A similar compound $\text{Ca}_2\text{FeMoO}_6$ as well a ferrimagnetic oxide with $t = 0.96$ ($r(\text{Mo}^{5+}) = 0.75 \text{ \AA}$) was found recently to have a monoclinic unit cell [173].

²You have to take the coordination number into account.

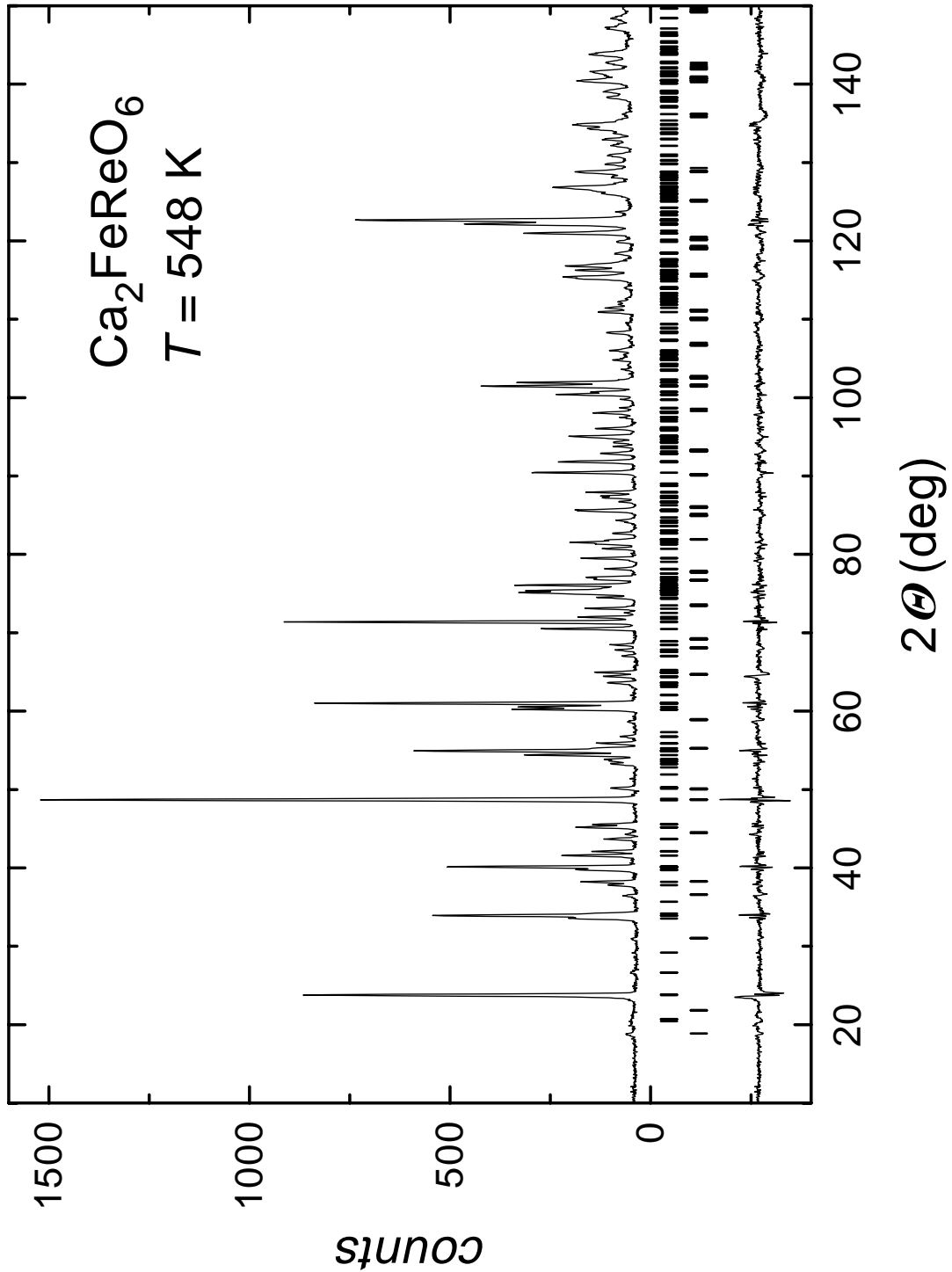


Figure 5.2: Observed neutron diffraction pattern for double-perovskite $\text{Ca}_2\text{FeReO}_6$ at $T = 548 \text{ K}$ above T_C . Due to the strongly distorted perovskite structure the pattern shows a large number of Bragg peaks. The difference pattern (bottom) arises from a refinement including the monolinic $\text{Ca}_2\text{FeReO}_6$ phase and the magnetite impurity phase (2.4%). The reflection positions of both phases are marked by bars.

In Fig. 5.2 the neutron diffraction pattern above T_C at $T = 548$ K recorded at D2B is shown. A slight impurity phase of 2.4% of Fe_3O_4 due to the reaction



could be detected at all temperatures [174]. Omitting this phase had negligible influence on the refinement of the main phase, which was refined in the monoclinic space group³ $P2_1/n$. The monoclinic unit cell results from rotations of the BO_6 , $\text{B}'\text{O}_6$ octahedra. The symmetry is strongly reduced to the unique axis b

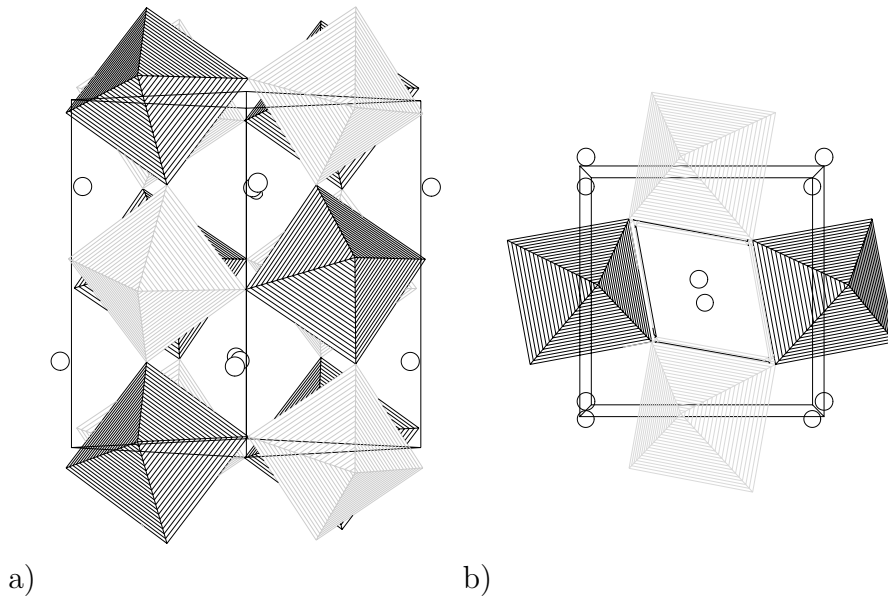


Figure 5.3: a) View of the unit cell along the crystallographic (110) direction corresponding to a pseudocubic a or b axis. The monoclinic rock-salt arrangement of the Fe (black) and Re (grey) ions with opposite rotations of the octahedra along viewing direction can be seen. b) View along the crystallographic (001) direction showing in phase rotations. The positions of the A atom Ca is pictured by circles.

with a twofold screw axis with screw vector $\frac{1}{2}\vec{b}$ and a diagonal glide plane with glide vector $\frac{1}{2}(\vec{a} + \vec{c})$. These symmetries are shown in the appendix. The reflection positions of the $\text{Ca}_2\text{FeReO}_6$ phase and the magnetite impurity phase are marked by bars each in a row below the pattern. Below the reflection positions the difference pattern is presented. The refinement with a R -Bragg factor (see appendix) of 4.4% leads to the following cell parameters for $\text{Ca}_2\text{FeReO}_6$: $a = 5.4366(5)$ Å, $b = 5.5393(5)$ Å, $c = 7.7344(5)$ Å, and $\beta = 90.044(4)^\circ$.

Fe and Re are indistinguishable for neutrons in the paramagnetic regime due to the small difference in the nuclear coherent scattering lengths (see Eq. 1.16) of 9.45 fm and 9.20 fm, respectively [176, 177]. However, in the ferromagnetic regime

³Here, the setting unique axis b and cell choice 2, leading to $P 1 2_1/n 1$, was chosen [175].

Table 5.1: Positional and thermal parameters of $\text{Ca}_2\text{FeReO}_6$ (space group $P2_1/n$) at 548 K. The R -Bragg factor is 4.4%. The ideal positions in the case of a nondistorted perovskite structure are indicated by fractions. As expected, the heavy Re ions exhibit a lower root-mean square thermal displacement from their equilibrium position.

Atom	Site	x	y	z	B (\AA^2)
Ca	4e	0.0128(7)	0.0432(7)	0.7484(7)	1.11(8)
		0	0	$\frac{3}{4}$	
Fe	2d	$\frac{1}{2}$	0	0	0.63(5)
Re	2c	0	$\frac{1}{2}$	0	0.15(3)
O1	4e	0.2914(7)	0.2940(7)	0.9591(7)	0.69(7)
		$\frac{1}{4}$	$\frac{1}{4}$	1	
O2	4e	0.2996(7)	0.2918(7)	0.5389(7)	1.22(8)
		$\frac{1}{4}$	$\frac{1}{4}$	$\frac{1}{2}$	
O3	4e	0.9206(7)	0.4791(7)	0.7514(7)	0.94(7)
		1	$\frac{1}{2}$	$\frac{3}{4}$	

they can be discerned due to the interaction of the neutron with the magnetic moment of the electron shells.

Additionally, the structure was checked with X-ray diffraction (see below). The refinements show that the Fe atoms occupy the 2d position with coordinates $(\frac{1}{2}, 0, 0)$; $(0, \frac{1}{2}, \frac{1}{2})$ and Re the 2c position with coordinates $(0, \frac{1}{2}, 0)$; $(\frac{1}{2}, 0, \frac{1}{2})$, i.e. there exists an ordered rock-salt arrangement. The positions of the A atom and the three oxygen atoms could be revealed by neutron diffraction. They occupy different 4e positions with coordinates (x, y, z) ; $(\bar{x} + \frac{1}{2}, y + \frac{1}{2}, \bar{z} + \frac{1}{2})$; $(\bar{x}, \bar{y}, \bar{z})$; $(x + \frac{1}{2}, \bar{y} + \frac{1}{2}, z + \frac{1}{2})$. The monoclinic unit cell with tilts of the octahedra is shown in Fig. 5.3. The FeO_6 octahedra and ReO_6 octahedra are sketched black and grey, respectively. The positions of the A atom Ca is pictured by circles. According to Glazers notation the distortion is $u^-u^-v^+$ [178, 179]. The parameters u and v denote rotation angles of the octahedra about the respective pseudocubic axes. The superscripts indicate that neighboring octahedra along the corresponding axis rotate in the same (+) or opposite (-) direction. The view in Fig. 5.3a is along the pseudocubic a or b axis (view along the crystallographic (110) direction) and shows octahedra rotations with opposite sign. Part b of the figure presents the view along the crystallographic c axis showing the in-phase rotation of the octahedra along this axis.

The positional and thermal parameters are listed in table 5.1. As mentioned in the first chapter, increasing temperature decreases the intensity of a Bragg

reflection. The atomic scattering factor (see Eq. 1.12) has to be corrected with the Debye-Waller factor of atom j given by

$$\exp[-M_j] = \exp\left[-8\pi^2\overline{u_{s,j}^2}\left(\frac{\sin(\theta)}{\lambda}\right)^2\right] \quad (5.2)$$

where $\overline{u_{s,j}^2}$ is the root-mean square thermal displacement perpendicular to the involved net plane [180]. Values of $0 \text{ \AA}^2 - 2 \text{ \AA}^2$ were found as shown in table 5.1. As expected the heavy Re ions exhibit a lower root-mean square thermal displacement from their equilibrium positions as the light oxygen atoms.

With decreasing temperature one observes an unusual peak broadening and finally a *peak splitting* of selective nuclear Bragg reflections with a large momentum transfer along the unique b axis. An unusual broadening of peaks, which has a large component along the unique axis, was also observed in perovskite manganites $\text{Nd}_{1-x}\text{Sr}_x\text{MnO}_3$ which belong to the same space group [181]. Although

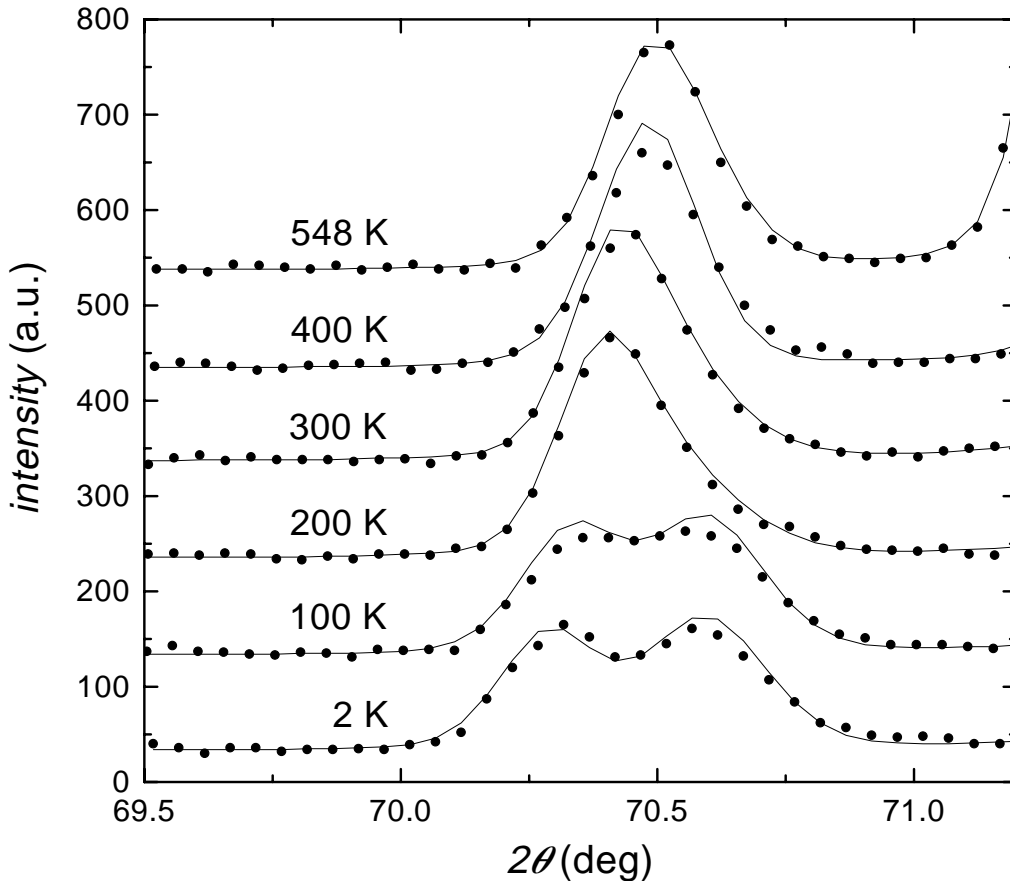


Figure 5.4: Temperature dependence of the (040) $\text{Ca}_2\text{FeReO}_6$ reflection peak. With decreasing temperature this peak with a large momentum transfer along the unique b axis broadens and finally splits into two reflections. Lines are from refinements including two crystallographic phases as described in the text.

Table 5.2: Lattice constants and β angles as a function of temperature of the two phases. Above 300 K the two phases merge to a single phase.

Phase 1				
T (K)	a (Å)	b (Å)	c (Å)	β (deg)
2	5.4043(5)	5.5303(7)	7.6923(5)	90.225(4)
100	5.4060(5)	5.5297(7)	7.6942(5)	90.216(4)
200	5.4091(5)	5.5341(7)	7.6997(5)	90.077(4)
300	5.4167(5)	5.5342(7)	7.7091(5)	90.047(4)
400	5.4222(5)	5.5382(5)	7.7136(5)	90.059(4)
444	5.4267(5)	5.5385(5)	7.7199(5)	90.053(4)
490	5.4312(5)	5.5380(5)	7.7264(5)	90.047(4)
524	5.4342(5)	5.5387(5)	7.7311(5)	90.044(4)
548	5.4366(5)	5.5393(5)	7.7344(5)	90.044(4)
Phase 2				
2	5.3949(5)	5.5515(7)	7.6812(5)	90.085(4)
100	5.3992(5)	5.5480(7)	7.6853(5)	90.112(4)
200	5.4059(5)	5.5444(7)	7.6913(5)	90.081(4)
300	5.4142(5)	5.5428(7)	7.7021(5)	90.077(4)

the best refinement was achieved in this case using two distinct phases the origin of the peak broadening has been attributed to the existence of strain effects. Here the clear splitting of the (040) reflection visible in the diffraction pattern as shown in Fig. 5.4, however, cannot originate from strain effects and obviously two distinct phases are required. Therefore, in the refinement two distinct crystallographic phases were used. Since the symmetry of a magnetic unit cell can be lower than the symmetry of the corresponding nonmagnetic unit cell, nuclear and magnetic scattering are described with distinct phases. All atom positions of the respective nuclear and magnetic phases are identical in the refinement. Only *two* additional free parameters for the magnetic moment of the Fe and Mo atoms, respectively, are required for each magnetic phase. Allowing more degrees of freedom for the magnetic phases did not improve the refinements. The intensities of the low angle peaks (011) and (101) are mainly magnetic due to the fact that the same scattering lengths of Fe and Re result in an extinction of the low angle reflections. Therefore, the magnetic contributions are well separable from the nuclear scattering contribution. In addition a small contribution from an impurity phase of 2.4% of magnetite was included. The diffraction pattern taken at $T = 2$ K is presented in Fig. 5.5. The reflection positions of the five phases are sketched by bars in five rows. The two phases of $\text{Ca}_2\text{FeReO}_6$ differ mostly in the values of the

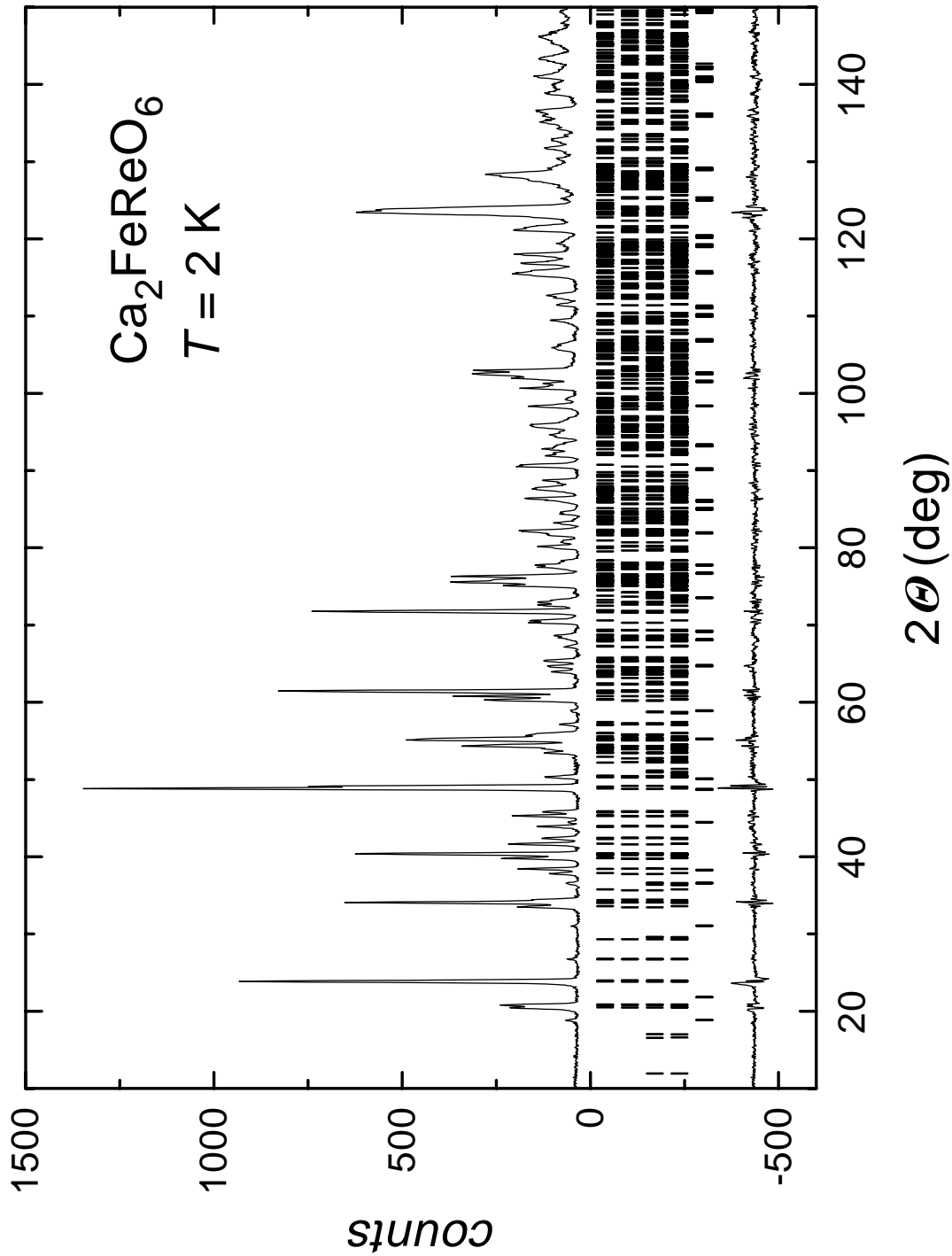


Figure 5.5: Observed neutron diffraction pattern for double-perovskite $\text{Ca}_2\text{FeReO}_6$ at $T = 2 \text{ K}$. The difference pattern (bottom) arises from a refinement including the two crystallographic and magnetic monoclinic $\text{Ca}_2\text{FeReO}_6$ phases as well as the magnetite impurity phase (2.4%). The reflection positions of the five phases are marked by bars in five rows. At $2\theta = 20.5^\circ$ the magnetic peaks which were absent in the pattern above T_C (see Fig. 5.2) are now visible.

Table 5.3: Positional and thermal parameters of double-perovskite $\text{Ca}_2\text{FeReO}_6$ (space group $P2_1/n$) at 2 K. The R -Bragg factor for the two phases are 4.1% and 3.6%, respectively.

Phase	Atom	Site	x	y	z	B (\AA^2)
1	Ca	4e	0.0078(5)	0.0482(5)	0.7485(5)	0.14(5)
	Fe	2d	$\frac{1}{2}$	0	0	0.05(3)
	Re	2c	0	$\frac{1}{2}$	0	0.00(1)
	O1	4e	0.2931(5)	0.2928(5)	0.9564(4)	0.45(4)
	O2	4e	0.3025(5)	0.2951(5)	0.5414(4)	0.37(4)
	O3	4e	0.9148(5)	0.4748(5)	0.7516(4)	0.35(4)
2	Ca	4e	0.0158(5)	0.0503(5)	0.7517(4)	0.22(5)
	Fe	2d	$\frac{1}{2}$	0	0	0.06(3)
	Re	2c	0	$\frac{1}{2}$	0	0.00(1)
	O1	4e	0.2990(5)	0.2993(5)	0.9531(4)	0.33(4)
	O2	4e	0.2944(5)	0.2917(5)	0.5439(4)	0.38(4)
	O3	4e	0.9171(5)	0.4749(5)	0.7516(4)	0.35(4)

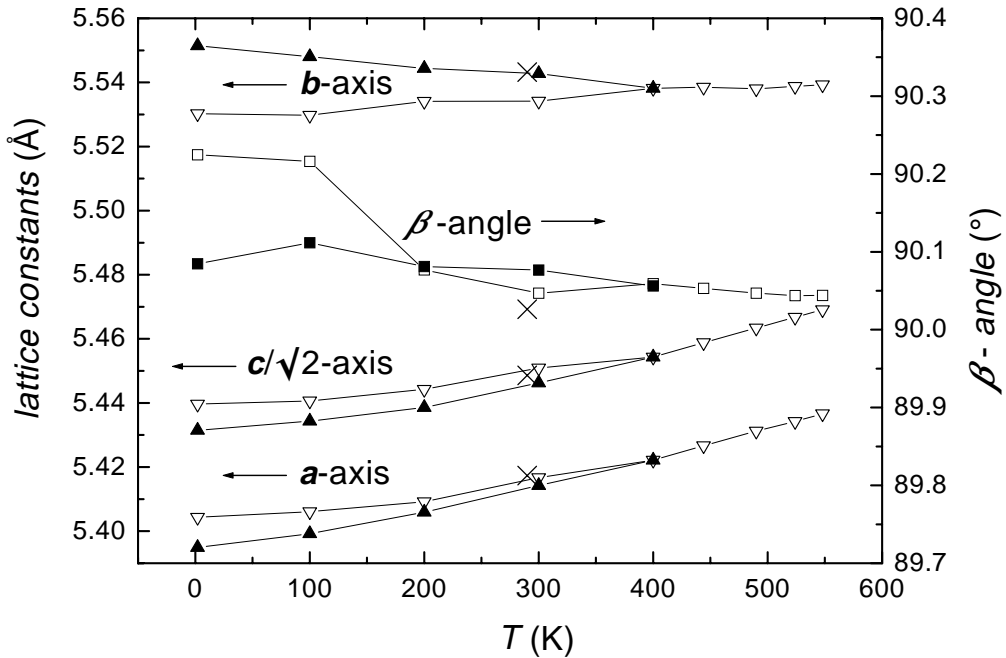


Figure 5.6: Temperature dependence of the lattice constants (triangles) and the β angle (squares) of the two different $\text{Ca}_2\text{FeReO}_6$ phases measured by neutron diffraction. The two phases merge to a single phase above room temperature. The results from X-ray diffraction (only one phase refined) at 290 K are shown by crosses.

Table 5.4: Main bond lengths (\AA) and selected angles (deg) for monoclinic $\text{Ca}_2\text{FeReO}_6$ determined from neutron powder diffraction data at 2 K and 548 K.

Temperature	2 K		548 K
Phase	1	2	
Main bond lengths of FeO_6 octahedra (\AA)			
Fe—O1	1.9955	2.0163	2.0094
Fe—O2	2.0134	1.9930	2.0181
Fe—O3	1.9960	1.9892	1.9954
Main bond lengths of ReO_6 octahedra (\AA)			
Re—O1	1.9846	1.9937	1.9781
Re—O2	1.9765	1.9918	1.9725
Re—O3	1.9686	1.9640	1.9737
Bond angles (deg)			
Fe—O1—Re ($\times 2$)	152.524	149.691	153.423
Fe—O2—Re ($\times 2$)	151.383	152.490	153.046
Fe—O3—Re ($\times 2$)	151.909	152.581	153.970
Short bond lengths Ca—O (\AA)			
Ca—O1	2.3770	2.3279	2.3700
Ca—O1	2.5972	2.5751	2.6222
Ca—O1	2.6735	2.7052	2.6953
Ca—O2	2.3684	2.3600	2.3840
Ca—O2	2.6379	2.5710	2.6376
Ca—O2	2.6604	2.6910	2.6891
Ca—O3	2.3196	2.3728	2.3828
Ca—O3	2.4123	2.4166	2.4662

b axes and the β angles but have almost the same unit cell volume. The results for the lattice constants and the β angles of all refinements are listed in table 5.2 and presented in Fig. 5.6. From 2 K up to 300 K the two phases have almost the same weight in the refinement but the difference in lattice parameters between the two phases decreases with increasing temperature. At temperatures of 400 K and higher the $(0k0)$ reflections are symmetric, which is depicted in Fig. 5.4, and Rietveld refinement shows a single phase. It is unresolved if the two phases are just similar and can no longer be crystallographically distinguished or whether a true phase separation of a single high temperature phase takes place below 400 K. In table 5.3 the positional and thermal parameters of the two phases are shown. The bond length and bond angles are presented in table 5.4 corroborating again the distorted perovskite structure of $\text{Ca}_2\text{FeReO}_6$.

5.2.2 X-ray diffraction

The X-ray powder diffraction pattern of $\text{Ca}_2\text{FeReO}_6$ was taken at room temperature. The data are shown in Fig. 5.7. The 2.4% impurity phase of magnetite

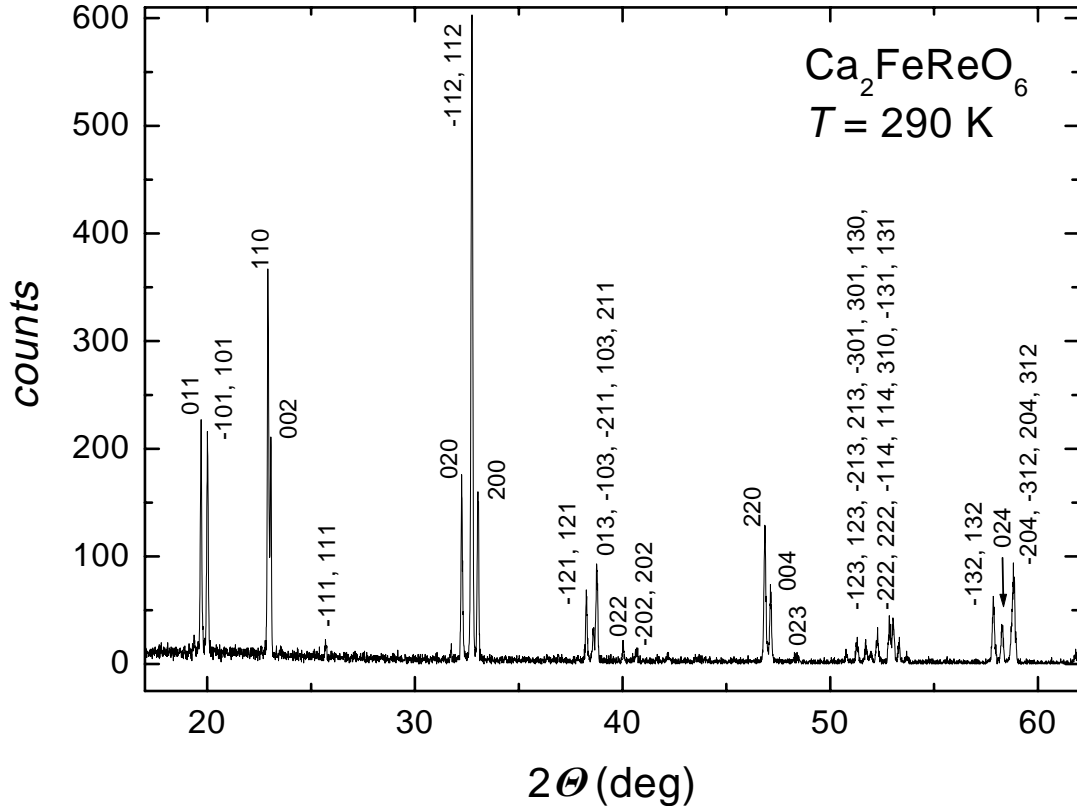


Figure 5.7: X-ray powder diffraction pattern for $\text{Ca}_2\text{FeReO}_6$ taken at ambient temperature. The Bragg peaks are indexed in a monoclinic unit cell with $a = 5.417(2)$ Å, $b = 5.543(2)$ Å, $c = 7.706(2)$ Å, and $\beta = 90.03(3)^\circ$ (space group $P2_1/n$).

could not be detected in the X-ray experiment. The lattice constants, extracted from the X-ray peak positions, are in agreement with the data gained by neutron diffraction. Due to the high absorption of X-rays in the Re compound, an accurate refinement of the full X-ray profile was not possible as it depended on the absorption correction introduced. In neutron scattering experiments absorption can be neglected. The main intention of the X-ray refinement was to gain information on the Fe,Re sublattice ordering, which have very different atomic scattering factors, while their nuclear coherent neutron scattering lengths are nearly identical. The high intensity of the (011) and $(\bar{1}01)$, (101) reflections indicate the rock-salt arrangement of the Fe,Re sublattice. Due to the lower intensity of higher angle reflections in X-ray experiments only one phase could be refined. The refined cell parameters of $a = 5.417(2)$ Å, $b = 5.543(2)$ Å, $c = 7.706(2)$ Å, and $\beta = 90.03(3)^\circ$ are shown in Fig. 5.6 by crosses.

5.3 Magnetic properties

A Curie temperature of 540 K for $\text{Ca}_2\text{FeReO}_6$ was found in 1961 by Longo and Ward [170]. However, a detailed investigation of the magnetic properties is still missing. Hence, AC susceptibility, overall, and local magnetic moment, as well as magnetic hysteresis were measured.

5.3.1 Magnetic susceptibility

In Fig. 5.8 the AC susceptibility versus temperature is shown. Beside the ferro(i)-magnetic transition at 540 K in the inset, there are two additional anomalies. There is a slight temperature dependence of χ' from room temperature down to 125 K. At this temperature the susceptibility becomes temperature independent and there is a small anomaly also in the loss component χ'' . A clear magnetic phase transition exists at 50 K showing up as a sharp decrease of χ' and a sharp maximum in χ'' . These anomalies are frequency independent (the measurement taken at 7 Hz not presented in Fig. 5.8 shows the same anomalies) but they do not show up in the temperature dependence of the DC magnetic moment.

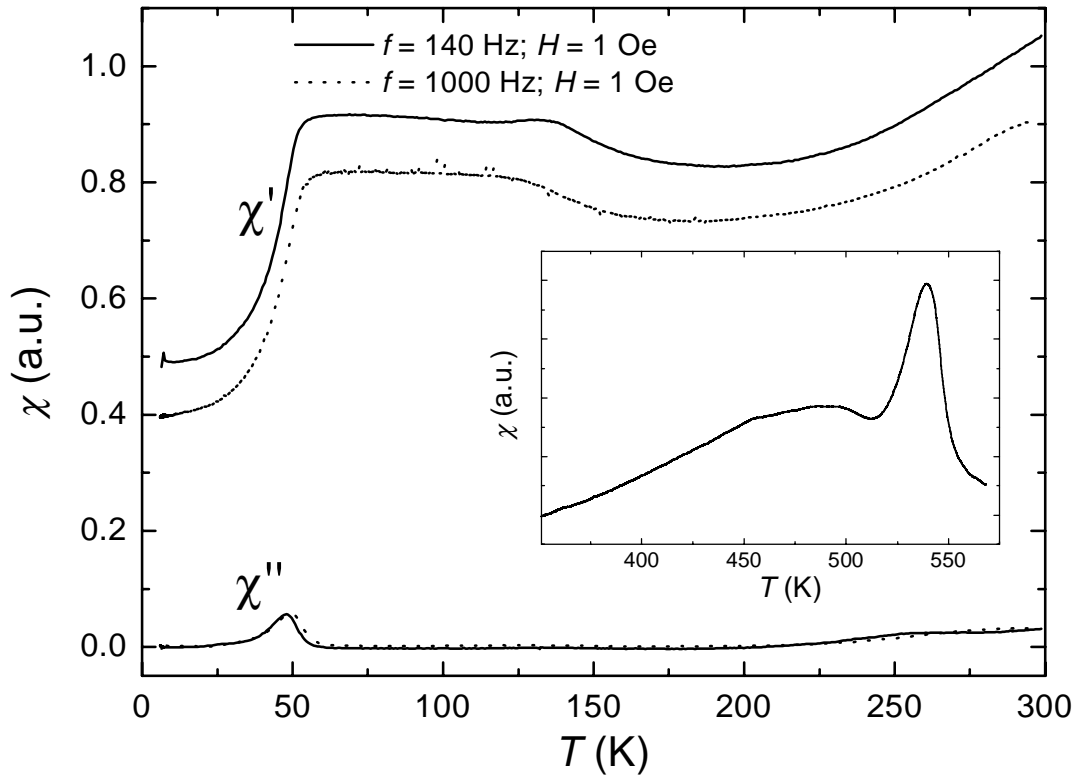


Figure 5.8: Temperature dependence of the AC susceptibility of $\text{Ca}_2\text{FeReO}_6$ from 4 K up to 300 K. The inset shows the AC susceptibility above room temperature. Clearly a peak at the Curie temperature of 540 K can be seen.

5.3.2 DC magnetization

Measurements of the DC magnetization show magnetic hysteresis loops. A full saturation of the magnetic moment at low temperatures is not achieved in fields of $\mu_0 H = 1$ T. The unusual shape of the low temperature hysteresis curves can be understood by a superposition of two magnetic phases with high and low coercivity, respectively. They both contribute approximately equal to the total magnetic moment as it is sketched in Fig. 5.9. These two phases were attributed

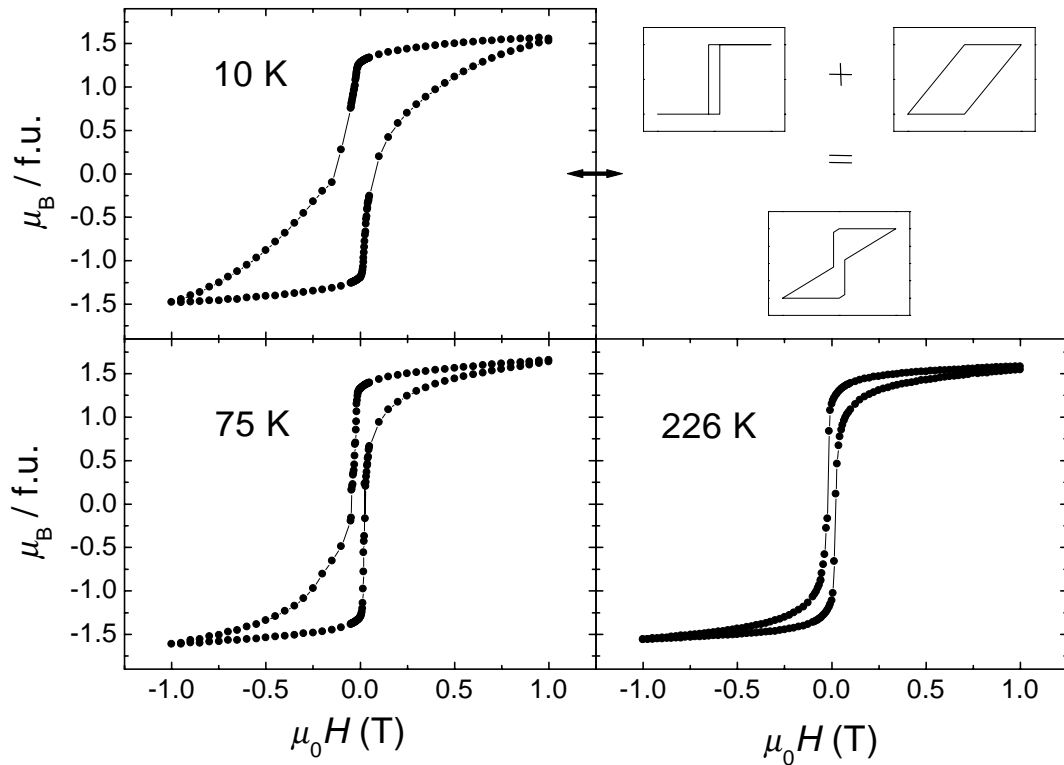


Figure 5.9: Hysteresis loops of $\text{Ca}_2\text{FeReO}_6$ at constant temperatures of 10 K, 75 K, and 226 K, measured in magnetic fields from -1 T to 1 T. The unusual shape of the low temperature hysteresis curve results from two magnetic phases with high and low coercivity, as it is sketched in the figure.

to the two different crystallographic phases which possess different anisotropy energies. With increasing temperature the magnetic phase of high coercivity becomes ‘softer’ and the hysteresis curves of both phases merge to a nearly normal ferromagnetic hysteresis loop. The remnant magnetic moment of $1.3 \mu_B/\text{f.u.}$ is temperature independent below 250 K while the total coercivity increases from 11 mT at 250 K to 0.13 T at 4 K. The observed saturation magnetic moment is lower than the ideal value of $3 \mu_B/\text{f.u.}$ in the case of a perfect ferrimagnetic ordering of Fe^{3+} ($3d^5$) and Re^{5+} ($5d^2$) on the B, B' positions. As described in the preceding chapter, this discrepancy between theory and experiment could be a hint to disorder in the Fe,Re sublattice.

5.3.3 Magnetic structure from neutron scattering

Due to the different number of d electrons in the shells Fe and Re are distinguishable magnetically for neutrons in the ferromagnetic regime. Large magnetic contributions to the (011) and (101) Bragg peaks are visible around 20.5° at low temperatures. The nuclear contribution to these peaks is negligibly small. Due

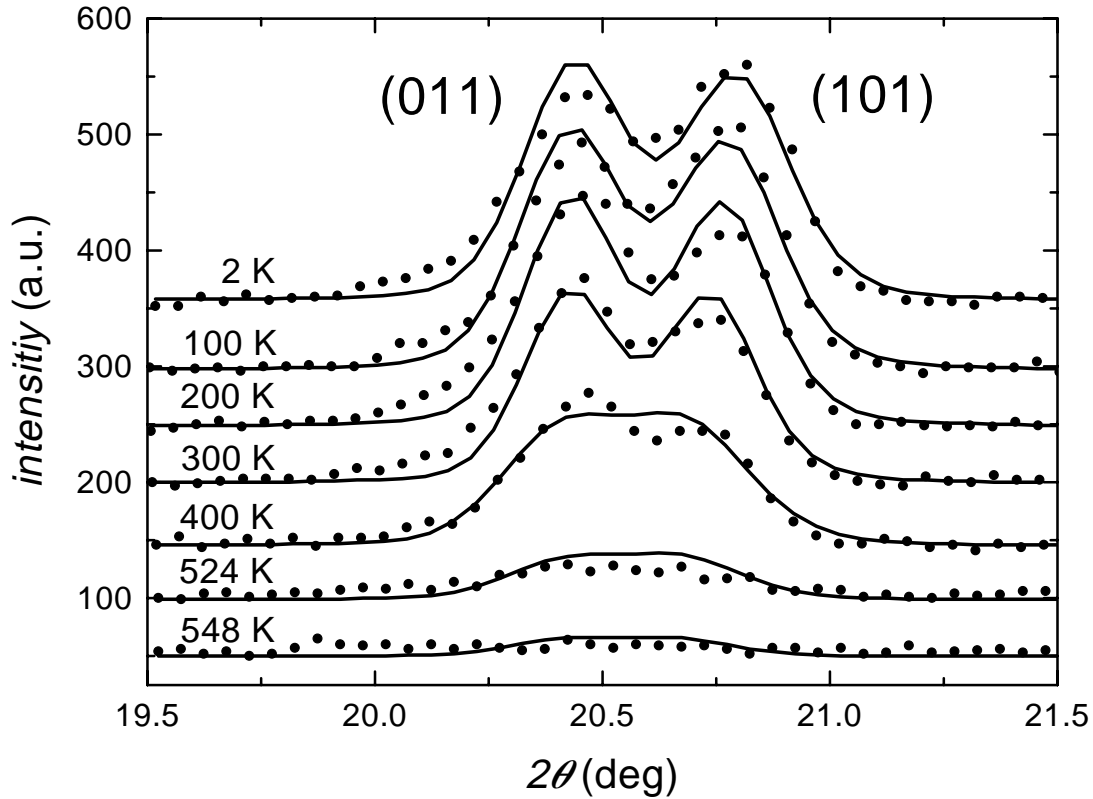


Figure 5.10: *Temperature dependence of the (011) and (101) Bragg peaks which are only visible in the ferromagnetic regime due to their magnetic origin.*

to the fact that the magnetic form factor of Re^{5+} is unknown, it is approximated using the values for Mo^{3+} [182]. Within this approximation the best refinements were obtained with a ferrimagnetic arrangement of the Fe and Re spins for one phase and a ferromagnetic alignment of the Fe spins for the other phase. The magnetic moments at the Fe and Re positions are $4.0(2) \mu_B$ and $-0.81(6) \mu_B$, respectively for phase **1** and $4.2(2) \mu_B$ and $-0.1(6) \mu_B$, respectively for phase **2**. In both phases best refinements were achieved for spin orientations along the [110] direction. At 2 K R -Bragg factors of 4.7% and 4.2% for the two phases were obtained. The temperature dependence of the (011) and (101) Bragg peaks is shown in Fig. 5.10. The magnetic contribution decreases with increasing temperature and vanishes at T_C . The magnitude of the refined magnetic moment disagrees with the DC magnetization result. In a magnetic field of $\mu_0 H = 1$ T one should reach in DC magnetization a value close to saturation, while one obtains only

$M_{\text{Sat}} \approx 1.5 \mu_{\text{B}}/\text{f.u.}$ in the experiment. The approximative use of the magnetic form factor is not expected to be responsible for this discrepancy and since the temperature dependence of the low angle peaks confirms their magnetic origin, the neutron result is considered more reliable. Further investigations such as solving the spin structure of $\text{Ca}_2\text{FeReO}_6$ are necessary to elucidate this problem.

5.4 ^{57}Fe -Mössbauer measurements

To gain further information on the valence and the electronic state of the iron in the $\text{Ca}_2\text{FeReO}_6$ compound ^{57}Fe -Mössbauer measurements were performed. Natural iron was used for preparation of the sample which contains only 2.2% ^{57}Fe . The presence of rhenium in the sample caused some difficulties because of its strong absorption for γ rays. The L -I, L -II, and L -III absorption edges of rhenium have an energy slightly below the 14.4 keV γ quanta, which are used for ^{57}Fe -Mössbauer measurements. Therefore the resulting spectra have a low relative transmission and are difficult to fit.

The Mössbauer data are listed in table 5.5 and shown in Fig. 5.11. For both temperatures a six-line pattern, which is typical for magnetically long range ordered systems, was obtained [183]. At 293 K, Mössbauer spectroscopy revealed four iron sites which is understood, knowing the presence of two phases at 300 K from neutron diffraction measurements with two different iron sites for each phase. Both spectra were fitted with natural line width. In each phase, the isomer shift δ and the quadrupole splitting ΔE_{Q} were taken correlated, while the magnetic splitting B_{hf} appeared to be different for all four sites. At 4.2 K, the difference

Table 5.5: Mössbauer parameters: δ isomer shift, B_{hf} hyperfine field, and ΔE_{Q} quadrupole splitting.

T (K)	Iron Site	δ (mm/s)	B_{hf} (T)	ΔE_{Q} (mm/s)	Ratio
293	1 a	0.477(6) ^a	44.32(5)	-0.16(1) ^a	0.494(5) ^a
	1 b	0.477(6)	42.11(5)	-0.16(1)	0.494(5)
	2 a	0.401(5) ^b	43.22(5)	+0.03(1) ^b	0.506(5) ^b
	2 b	0.401(5)	41.10(5)	+0.03(1)	0.506(5)
4.2	1	0.495(7)	48.27(4)	-0.20(1)	0.494(5) ^c
	2	0.524(6)	48.39(4)	+0.15(1)	0.506(5) ^c

^acorrelated with Fe site 1 b

^bcorrelated with Fe site 2 b

^cratio taken from ambient temperature spectrum

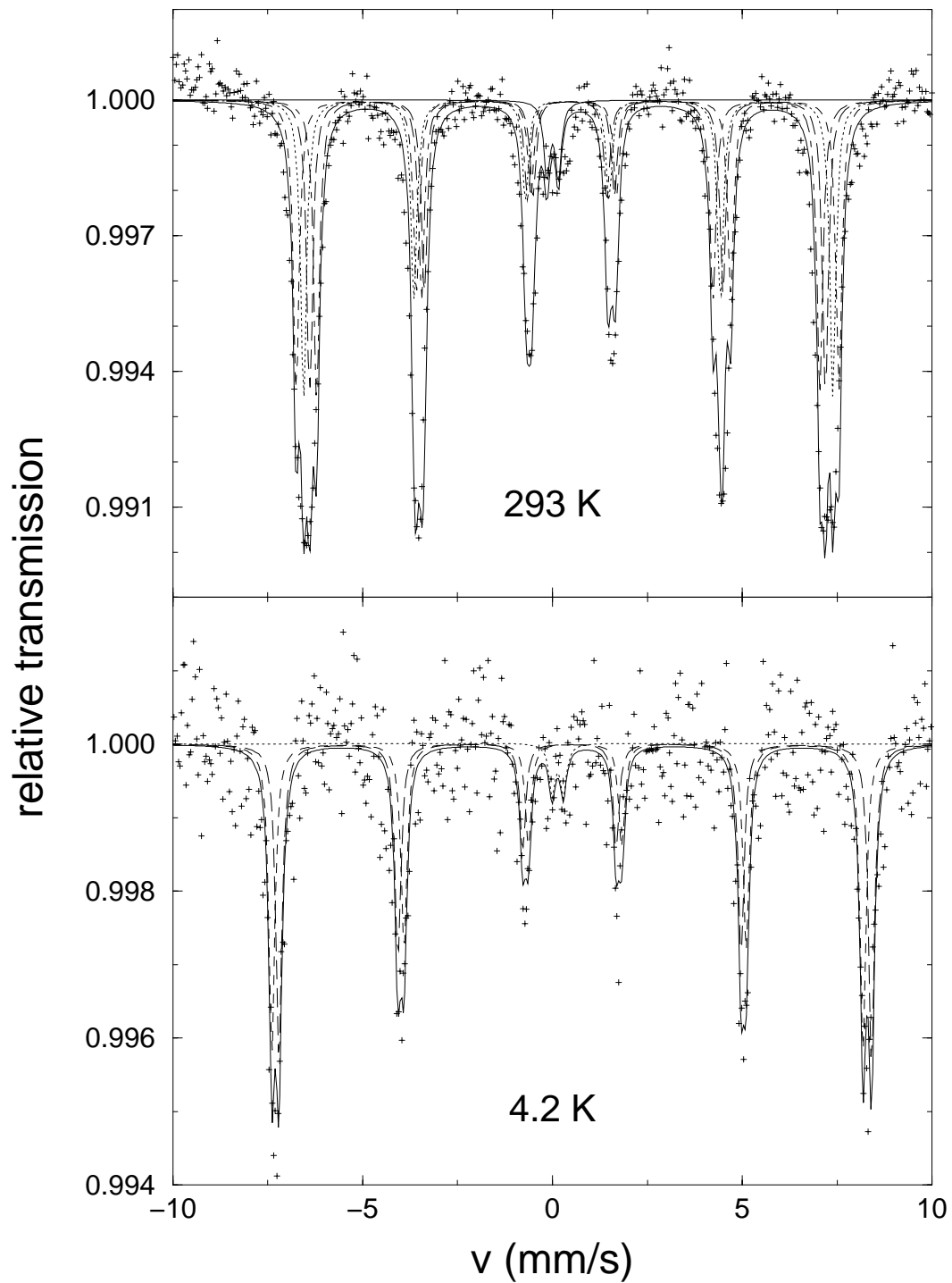


Figure 5.11: ^{57}Fe -Mössbauer spectra of $\text{Ca}_2\text{FeReO}_6$ recorded at 4.2 K and 293 K. The total fit curve (solid line) is composed of a superpositioning of the lines for phase 1 (dotted and dotted-dashed) and for phase 2 (dashed and long dashed).

in the magnetic splitting diminished, so that two sites in each phase appear almost indistinguishable, even though neutron diffraction clearly identifies at this temperature two different crystallographic phases. Such a behavior is typical for magnetic systems approaching magnetic saturation.

The subspectrum with an isomer shift $\delta = 0.004(5)$ mm/s relative to $\alpha\text{-Fe}$ at ambient temperature and $\delta = 0.139(6)$ mm/s at 4.2 K results from an Fe^{3+} impurity in the beryllium window of the proportional counter.

The hyperfine fields for $\text{Ca}_2\text{FeReO}_6$ are similar to the values of 43.7 T and 45.6 T at 77 K found in the analogous Ba compound $\text{Ba}_2\text{FeReO}_6$ [184, 185]. A larger hyperfine field of 53.4 T was found for $\text{Ca}_2\text{FeReO}_6$ at 77 K by Gopalakrishnan *et al.* [185]. Further, in a recent study on the Mo counterpart $\text{Ca}_2\text{FeMoO}_6$ the values for the magnetic fields are almost the same [166]. At 4.2 K a ratio of 0.44 : 0.56 was found for the two iron sites. However, no satisfying conclusion can be drawn on whether the iron ions are in two phases with one site or in one phase with two sites.

In $\text{Ca}_2\text{FeReO}_6$ the absolute values for quadrupole splitting show a small increase with decreasing temperature, which is typical for Fe^{3+} high spin in octahedral site [186]. Additionally the shifts, quadrupole splittings, and hyperfine fields are in the range of a typical Fe^{3+} in the high spin state in nearly octahedral environment [183].

5.5 Transport properties

In Fig. 5.12 the temperature dependence of the longitudinal resistivity of the double-perovskite $\text{Ca}_2\text{FeReO}_6$ is shown. The room temperature value of 17 m Ωcm is comparable with other reported results [187]. The temperature dependence shows a thermally activated behavior. Lowering the temperature to 4 K the resistivity increases more than three orders of magnitude to 53 Ωcm at 2.7 K. The transfer integral t_{ij}^0 (see Eq. 1.3) is strongly reduced due to the distorted Fe — O — Re bond angles. Even in magnetic fields of $\mu_0 H = 8$ T no magnetoresistance was observed over the whole temperature range. This is in contrast to the similar compound $\text{Ca}_2\text{FeMoO}_6$ which shows a metallic behavior and a large magnetoresistance [173]. Closer inspection of data reveals a change in the conduction mechanism. Below 20 K the resistivity increases strictly logarithmically with decreasing temperature, as shown in Fig. 5.12 in the inset. Above 110 K the temperature dependence of the resistivity is variable range hopping like, $\rho \propto \exp((T_0/T)^{0.25})$ with $T_0 = 2.5 \cdot 10^6$ K. This value is given in order to parametrize the temperature dependence of the sample resistivity, only. A similar behavior of the resistivity was found in doped manganites [157] and in disordered $\text{Sr}_2\text{FeMoO}_6$ thin films as shown in the precedent chapter. Using the density of

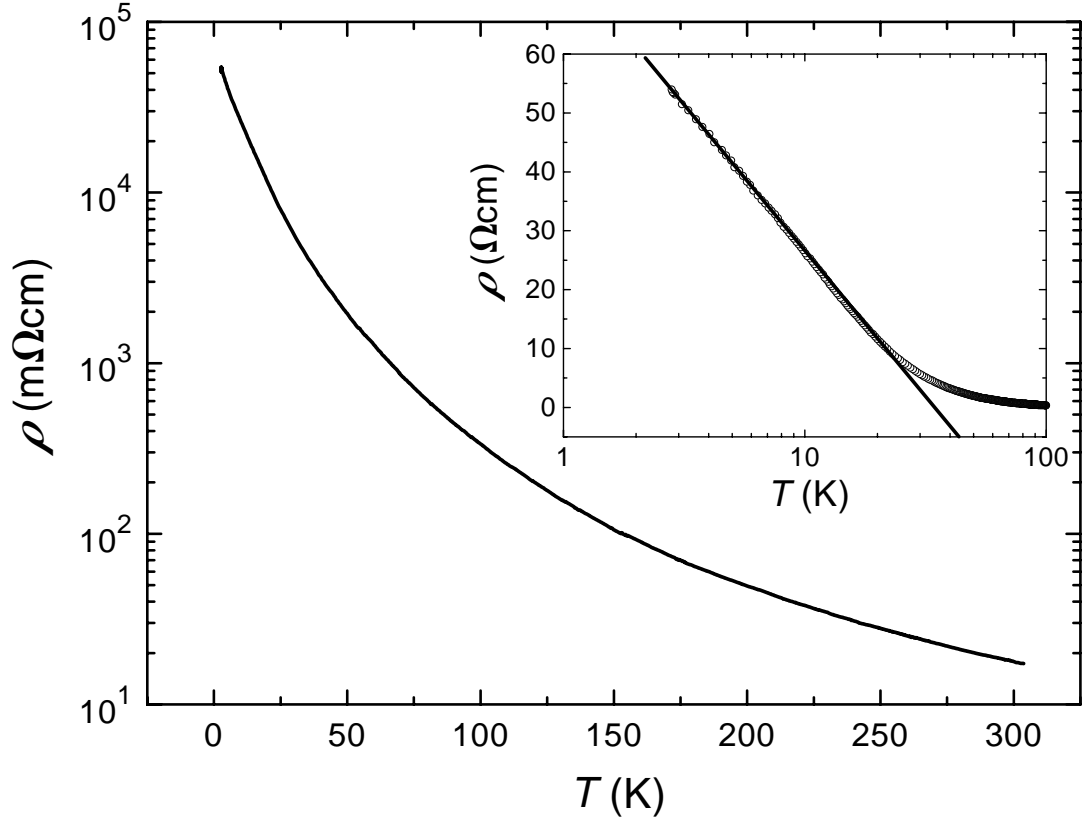


Figure 5.12: Temperature dependence of the longitudinal resistivity. Above 110 K the resistivity is described by a variable range hopping like model. Below 20 K the resistivity increases logarithmically with decreasing temperature as can be seen in the inset.

states $N(E_F)$ calculated by Kobayashi *et al.* [7] for $\text{Sr}_2\text{FeMoO}_6$ and the variable range hopping relation $k_B T_0 = 18/(l_0^3 N(E_F))$ for the localization length l_0 an unphysically small value of the temperature dependent hopping length R , smaller than the unit cell dimensions, would result [157]. Assuming a small density of states at the Fermi edge $N(E_F) = 0.05/(\text{eV}\cdot\text{f.u.})$, more reasonable values for the localization length $l_0 = 0.46$ nm and the average hopping length $R = 2.1$ nm, i.e. several unit cells, at 200 K are calculated. This points out that a deeper knowledge of the electronic structure of this compound is required to reach definite conclusions.

5.6 Conclusion

Concluding, the crystal structure, the transport and magnetic properties of polycrystalline double-perovskite $\text{Ca}_2\text{FeReO}_6$ were investigated. A monoclinic unit cell with rock-salt order of the Fe and Re ions was revealed by neutron diffraction. The compound has the highest Curie temperature of $T_C = 540$ K up to

now reported for magnetic perovskites. By Mössbauer measurements a typical Fe^{3+} state was revealed. For temperatures below 400 K a phase separation into two monoclinic phases with identical cell volumes is observed in neutron scattering experiments. The two crystallographic phases possess different magnetic structure and coercivity.

The temperature dependence of the resistivity exhibits a thermally activated behavior and shows no magnetoresistance over the whole temperature range. This transport behavior of $\text{Ca}_2\text{FeReO}_6$ is in contrast to the Mo counterpart $\text{Ca}_2\text{FeMoO}_6$, whereas for $A = \text{Ba}, \text{Sr}$ similar properties for the Mo and Re series A_2FeMoO_6 and A_2FeReO_6 were found as shown in table 5.6. By changing the

Table 5.6: Comparison of the series A_2FeMoO_6 and A_2FeReO_6 ($A = \text{Ba}, \text{Sr},$ and Ca). They have the same crystal structures (due to the same tolerance factor t) and transport properties. The sole exception is $\text{Ca}_2\text{FeReO}_6$, which is semiconducting (sc) in contrast to all other samples which are metallic (m).

Compound	A	t	Crystal Structure	$R(T)$	T_C (K)	References
A_2FeMoO_6	Ba	1.05	cubic ($Fm\bar{3}m$)	m	370	[144, 158, 188]
	Sr	0.99	tetragonal ($I4/mmm^1$)	m	430	[7, 144, 153]
	Ca	0.96	monoclinic ($P2_1/n$)	m	380	[144, 166, 188]
A_2FeReO_6	Ba	1.06	cubic ($Fm\bar{3}m$)	m	320	[170, 187, 189]
	Sr	1.00	tetragonal ($I4/mmm$)	m	400	[170, 190, 189]
	Ca	0.97	monoclinic ($P2_1/n$)	sc	540	[170, 173, 187]

A site cation with ion radius r from Ba ($r = 1.75 \text{ \AA}$) to Sr ($r = 1.58 \text{ \AA}$) to Ca ($r = 1.48 \text{ \AA}$) the unit cell volume decreases and a metal-insulator transition takes place for the Re series only. It is worth mentioning that the conduction band filling is not altered, but this transition is accompanied by a change in the crystal structure. Due to the different ion radii r of the A atom the compounds containing Ba and Sr are cubic and tetragonal, respectively. Preliminary X-ray measurements of the Re series are presented in Fig. 5.13.

Diffraction measurements on a single crystal are necessary to identify the origin of the phase separation in $\text{Ca}_2\text{FeReO}_6$. Further, the investigation of the

¹Recently, another tetragonal space group $P4_2/m$ was found with neutron powder diffraction measurements [191].

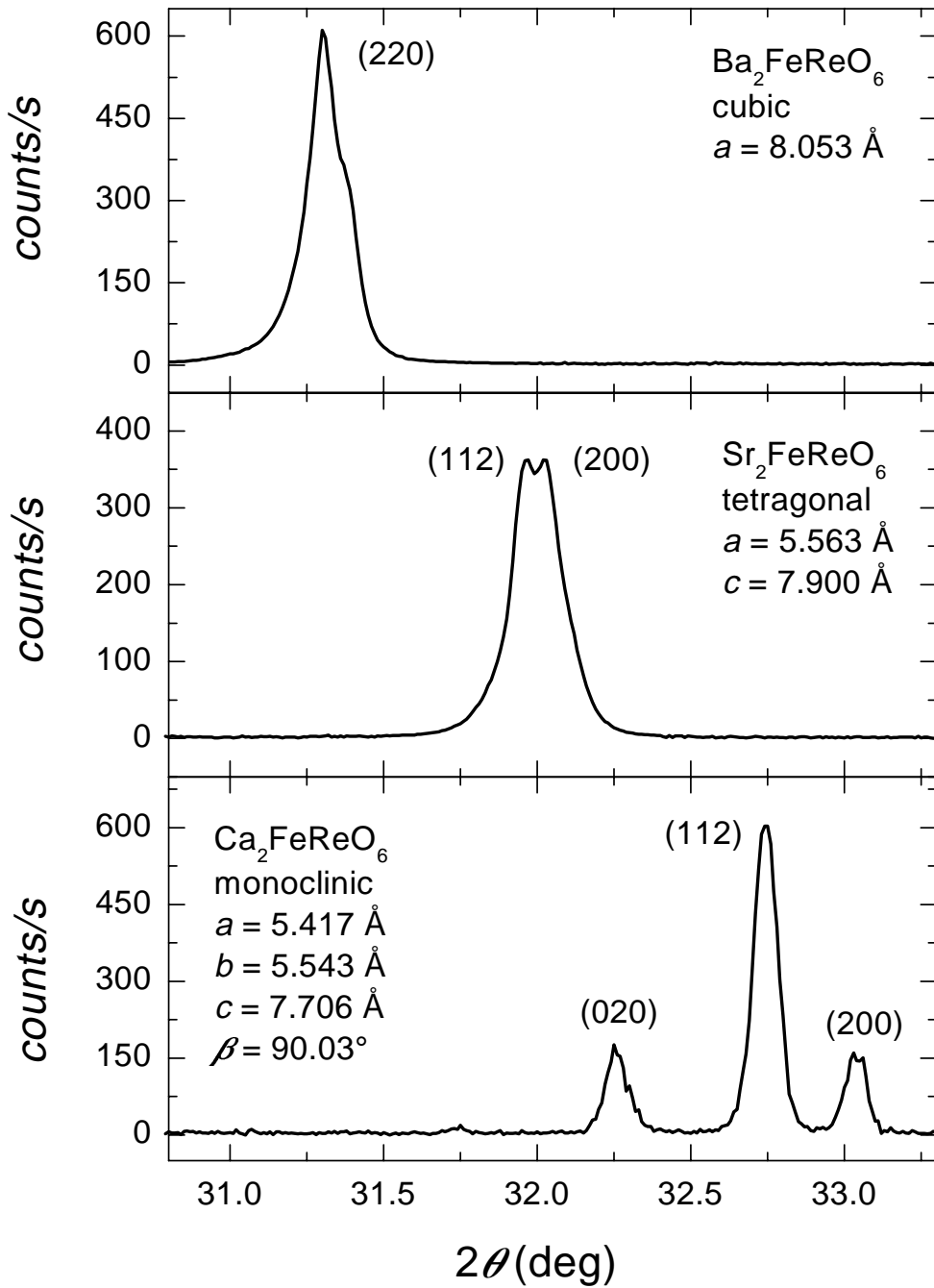


Figure 5.13: $\theta/2\theta$ -scans of $A_2\text{FeReO}_6$ ($A = \text{Ba}, \text{Sr}, \text{and Ca}$). The reflections shift to higher angles because of the decreasing unit cell volume. Moreover the crystal structure changes from cubic ($\text{Ba}_2\text{FeReO}_6$) to tetragonal ($\text{Sr}_2\text{FeReO}_6$) and finally to monoclinic ($\text{Ca}_2\text{FeReO}_6$) visible in the splitting up of the reflections.

influence of the rock-salt order on the magnetotransport properties for $\text{Ca}_2\text{FeReO}_6$ is needed to reveal the origin of the thermally activated behavior of the resistivity. Perhaps a fully ordered sample or an epitaxial thin film under strain exhibits again

a metallic behavior. This would be important for applications if $\text{Ca}_2\text{FeReO}_6$ with $T_C = 540$ K is as well highly spin polarized. The whole series $A_2\text{FeReO}_6$ ($A = \text{Ba}, \text{Sr}, \text{and Ca}$) is currently investigated in the research group [189].

Summary

In the present work mixed-valence manganites and double-perovskites were investigated. This thesis owes much to the high-temperature superconductor boom which preceded it. At the beginning the expertise was partly available and resources were in place to prepare epitaxial thin films and ceramics of these oxides and to characterize the crystallographic, electronic, and magnetic properties thoroughly with a wide range of techniques.

In the early stages little was known about the real origin of the magnetoresistance, metallic transport and the metal-insulator transition in manganites. Therefore, one aim of this work was to get more insight in the transport mechanism through Hall effect measurements in very high magnetic fields, available at the High Field Magnet Laboratory in Nijmegen. A further goal was to find a magnetic oxide usable for practical applications in memory devices, i.e. a high magnetoresistance in low fields at ambient temperature, to deposit it as an epitaxial thin film, to investigate its crystal structure and its magnetotransport properties, and to integrate it in a device. One promising candidate $\text{Sr}_2\text{FeMoO}_6$ was for the first time successfully prepared in form of an epitaxial thin film with the desired properties. Its integration in a device remains a task for the future.

Epitaxial thin films of $\text{La}_{0.67}\text{Ca}_{0.33}\text{MnO}_3$ and $\text{La}_{0.67}\text{Sr}_{0.33}\text{MnO}_3$ were grown in (100) orientation on several single crystalline substrates using magnetron sputtering and pulsed laser deposition, respectively. For the latter case a higher degree of epitaxy was obtained. With Sr doping instead of Ca doping the Curie temperature could be shifted above room temperature. The longitudinal and transverse resistivities were measured below and above the Curie temperature in magnetic fields up to 20 T. The field sensitivity of the resistivity $d\rho/dB$ at room temperature could be increased by changing the dopant atom from Ca to Sr, but for applications it is still too insensitive at low magnetic fields. In the low temperature range, where the charge-carrier density n is constant, an electron-magnon scattering in the longitudinal resistivity was identified. Further, at the ferromagnetic transition temperature a charge-carrier density collapse was observed for both compounds. In the case of $\text{La}_{0.67}\text{Ca}_{0.33}\text{MnO}_3$, n decreases from 1.3 holes per unit cell below T_C to 0.6 holes per unit cell above T_C . The data indicate a simultaneous structural, magnetic, and electronic phase transition in doped manganite

thin films.

The high spin polarization in half-metallic manganites was exploited in tunneling experiments in order to enhance the field sensitivity of the resistivity. For this purpose, biepitaxial $\text{La}_{0.67}\text{Ca}_{0.33}\text{MnO}_3$ thin films were prepared on SrTiO_3 bicrystal substrates by pulsed laser deposition. Special emphasis was placed on the examination of the low- and high-field tunneling magnetoresistance as a function of magnetic field, temperature, and current. Due to spin polarized tunneling a large hysteretic magnetoresistance of 70% was observed at 4 K in low magnetic fields of 120 Oe. An obstacle for possible applications is the fact that the tunneling magnetoresistance decreases with increasing temperature because of spin fluctuations. Already at $T_C/2$ no significant low-field tunneling magnetoresistance remains, i.e. with manganites it is not possible to realize a sensor based on a bicrystal device which works at ambient temperature. Moreover, a nonohmic behavior of the current-voltage characteristics, which results in a nearly complete suppression of the tunneling magnetoresistance effect at high bias currents, was observed. A phenomenological model for the current dependence has been proposed, but at the moment the debate concerning the mechanism of the charge transfer through the grain boundary, tunneling or mesoscale transport, is not settled.

After understanding that the manganites with their low Curie temperatures would hardly be the ideal material as part in practical devices which have to work at room temperature, the work was focused on the preparation of the half-metallic double-perovskite $\text{Sr}_2\text{FeMoO}_6$ with a Curie temperature above 400 K. In comparison to the manganites close analogies exist in $\text{Sr}_2\text{FeMoO}_6$, in both systems the charge transport and magnetism between the metal ions are transferred by the oxygen ions.

Using pulsed laser deposition epitaxial thin films of $\text{Sr}_2\text{FeMoO}_6$ have been prepared on (100) SrTiO_3 substrates. Already for a deposition temperature of 320°C epitaxial growth is achieved. The main result of this thesis is the revealing of a structure-property relationship in double-perovskites, i.e. differences in crystal structure come along with differences in transport and magnetic properties. At high (low) deposition temperature the Fe,Mo sublattice has a rock-salt (random) structure and the films exhibit metallic (semiconducting) behavior. Only the metallic samples exhibit a large negative magnetoresistance which peaks at the Curie temperature. Hence disorder is detrimental to the half-metallic state. In agreement with the expected value for an ideal ferrimagnetic arrangement, the magnetic moment was determined to 4 μ_B per formula unit. At 300 K an electronlike charge-carrier density of 1.3 per Fe,Mo pair was found. In the semiconducting films, on the other hand, the magnetic moment is reduced to 1 μ_B per formula unit due to disorder in the Fe,Mo sublattice. At low temperatures

the anomalous Hall effect vanishes for the metallic thin films, indicating a low degree of magnetic and nonmagnetic scattering. This was up to now not obtained in epitaxial thin films and single crystals. The ordinary and anomalous Hall coefficients have reversed sign compared to the hole-doped manganites. They are negative and positive, respectively.

With the know-how and the experimental equipment achieved, it is now feasible to integrate $\text{Sr}_2\text{FeMoO}_6$ in a tunnel junction or to deposit it on bicrystal substrates. This subject is under current investigation in the research group.

A second compound in the class of double-perovskites $\text{Ca}_2\text{FeReO}_6$ was studied in detail. This compound has the highest Curie temperature of $T_C = 540$ K up to now reported for magnetic perovskites and is thus a promising candidate for novel applications in future. Since the preparation, in comparison to other oxides, is very difficult it was synthesized at first in form of polycrystalline powder. A monoclinic unit cell with rock-salt order of the Fe and Re ions was found using Rietveld refinement. The rotations and distortions of the oxygen octahedra in the distorted perovskite structure could be identified with neutron diffraction. By Mössbauer measurements a Fe^{3+} state in $\text{Ca}_2\text{FeReO}_6$ was revealed. Further, for temperatures below 400 K a phase separation in two monoclinic phases with identical cell volume was observed in neutron powder diffraction. The two crystallographic phases possess different magnetic structure and coercivity. In contrast to a similar monoclinic double-perovskite $\text{Ca}_2\text{FeMoO}_6$ a thermally activated behavior of the resistivity was measured. Over the whole temperature range no magnetoresistance could be observed. By changing the *A* site cation from Ba to Sr to Ca the distortion decreases and a metal-insulator transition takes place in the series $A_2\text{FeReO}_6$, even though the conduction band filling is not changed. At present the Ba- and Sr-doped compounds are studied exhaustively in the research group.

There is much work to be done, but it is sufficiently challenging and potentially rewarding in terms of interesting physics and novel magnetoelectronic devices that the subject of magnetic oxides as mixed-valence manganites and double-perovskites will flourish for at least another decade.

Especially the double-perovskite compounds $A_2\text{FeMoO}_6$ and $A_2\text{FeReO}_6$ with cation $A = \text{Ba}, \text{Sr},$ and Ca have a great potential regarding magnetoelectronics but the transport mechanism must be understood before these materials can be used with confidence in applications. Future tasks are the preparation of trilayer junctions $\text{Sr}_2\text{FeMoO}_6/\text{SrTiO}_3/\text{Sr}_2\text{FeMoO}_6$ or bicrystal contacts of $\text{Sr}_2\text{FeMoO}_6$ to obtain a large low-field magnetoresistance at ambient temperature.

Appendix A

Symmetry elements in the monoclinic space group $P2_1/n$

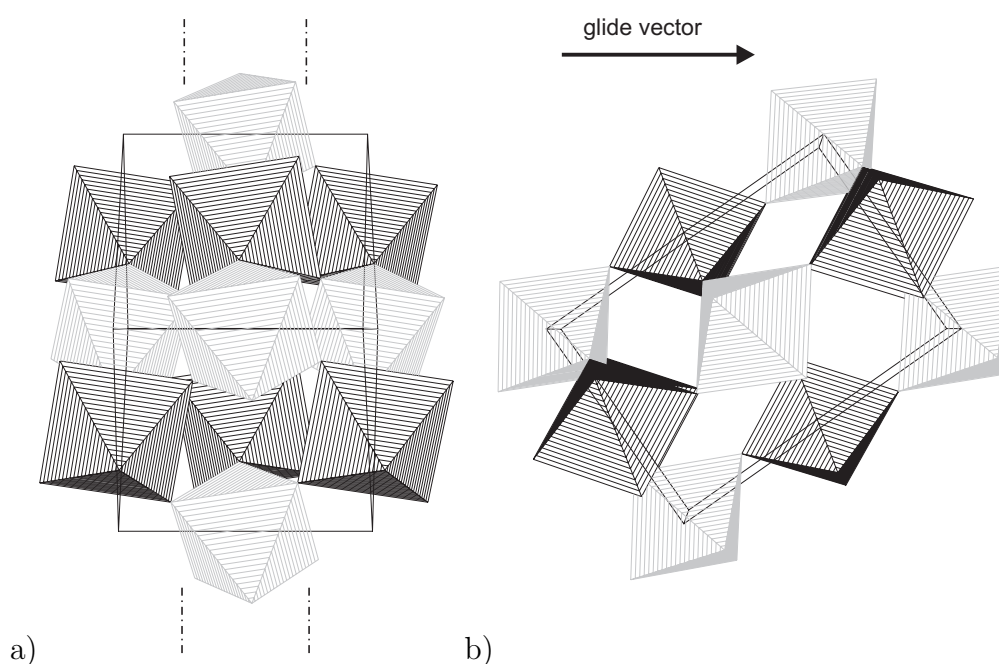


Figure A.1: a) In the monoclinic space group $P2_1/n$ exists a 'diagonal' glide plane marked by the symbol ' n '. The view of the picture is parallel to the glide vector $\frac{1}{2}(\vec{a} + \vec{c})$. The two diagonal glide planes containing the points $\frac{1}{4}\vec{b}$ and $\frac{3}{4}\vec{b}$ are indicated by the dashed-dotted lines. The glide plane symmetry, i.e. the translation of the glide vector followed by the mirror operation at the glide planes, is obvious.

b) In this part of the figure the view is perpendicular to the glide planes, i.e. along the crystallographic b direction or perpendicular to part a of the figure. The translation vector (glide vector) which is half of the face-diagonal is plotted.

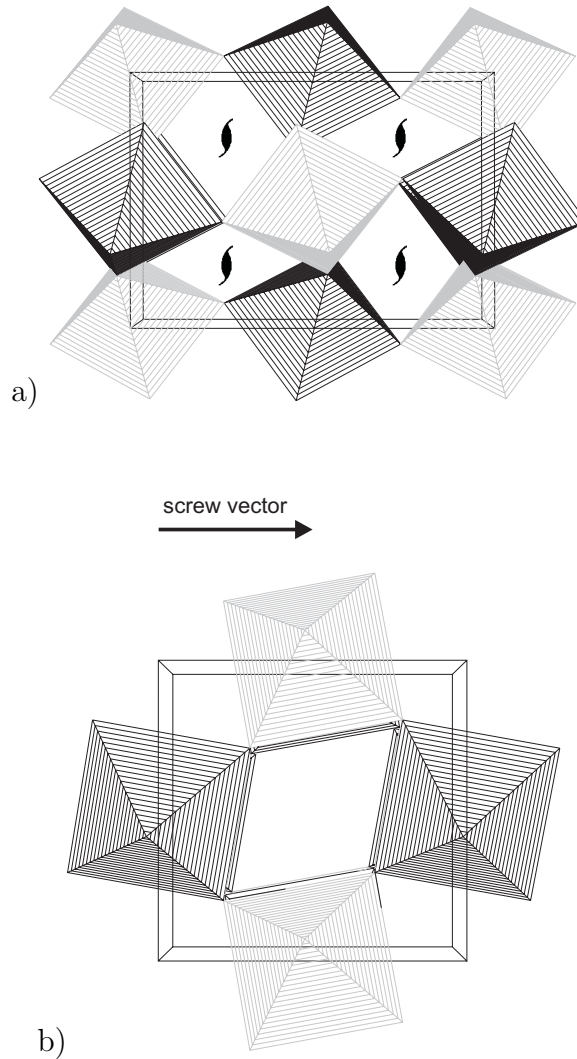


Figure A.2: a) A twofold screw axis $n_m = 2_1$ exists in the monoclinic space group $P2_1/n$. The view is along the crystallographic (010) axis. The four twofold screw axes at the positions $\frac{1}{4}(\vec{a} + \vec{c})$, $\frac{3}{4}(\vec{a} + \vec{c})$, $\frac{1}{4}\vec{a} + \frac{3}{4}\vec{c}$, and $\frac{3}{4}\vec{a} + \frac{1}{4}\vec{c}$ are marked by a graphical symbol. The screw axis symmetry, i.e. the rotation about the b axis by $\frac{360^\circ}{n} = 180^\circ$ followed by a translation parallel to the axis by $\frac{m}{n}\vec{b} = \frac{1}{2}\vec{b}$, is obvious.

b) This figure shows the side view of part a, i.e. the view is along the crystallographic c direction. The translation vector (screw vector) is plotted.

Appendix B

Preparation parameters

Table B.1: *Target preparation procedure for sputtering and laser ablation of the compounds $La_{0.67}Ca_{0.33}MnO_3$ and $La_{0.67}Sr_{0.33}MnO_3$.*

Raw material	Stoichiometric ratio (1:1:3) of La_2O_3 , $CaCO_3$ or $SrCO_3$, $MnCO_3$
Step 1	Grinding
Step 2	Heating with $1^\circ\text{C}/\text{min}$
Step 3	Sintering 12 h at 950°C
Step 4	Cooling with $-5^\circ\text{C}/\text{min}$
Step 5	Regrinding
Step 6	Pressing to disk with 100 kN laser ablation: \varnothing 1 in sputtering: \varnothing 50 mm
Step 7	Heating with $1^\circ\text{C}/\text{min}$
Step 8	Sintering 3 d at 1350°C
Step 9	Cooling with $-5^\circ\text{C}/\text{min}$

Table B.2: *Laser ablation parameters for the fabrication of epitaxial $La_{0.67}Ca_{0.33}MnO_3$ and $La_{0.67}Sr_{0.33}MnO_3$ thin films.*

Laser parameters	
Laser	Lambda Physik COMPEX301
Laser energy	100 mJ
	measured outside vacuum chamber
Energy density	2 J/cm ²
Frequency	3 Hz
Parameters during deposition	
Temperature	950°C
Pressure (O ₂)	14 Pa
Distance	32 mm – 38 mm
Aperture	8 × 8 mm ²
Deposition rate	0.3 Å/pulse
Mirror scan range	Center + 400 Steps
Parameters after deposition	
$La_{0.67}Ca_{0.33}MnO_3$	Cooling in 500 hPa O ₂
$La_{0.67}Sr_{0.33}MnO_3$	Annealing at 900°C for 1 h in 600 hPa O ₂

Table B.3: *Sputtering parameters for the fabrication of epitaxial $La_{0.67}Ca_{0.33}MnO_3$ thin films.*

Sputter parameters	
Method	DC sputtering
Voltage	250 V
Current	150 mA
Parameters during deposition	
Temperature	800°C
Process gas	Ar : O ₂ = 4 : 1
Flow	120 sccm
Pressure	300 Pa
Deposition rate	14 Å/min
Parameters after deposition	
$La_{0.67}Ca_{0.33}MnO_3$	Cooling in 600 hPa O ₂

Table B.4: Target preparation procedure for laser ablation of the double-perovskite compound $\text{Sr}_2\text{FeMoO}_6$.

Raw material	Stoichiometric ratio (4:1:2) of SrCO_3 , Fe_2O_3 , MoO_3
Step 1	Grinding
Step 2	Heating with $2^\circ\text{C}/\text{min}$
Step 3	Sintering 12 h at 1200°C
Step 4	Cooling with $-5^\circ\text{C}/\text{min}$
Step 5	Regrinding
Step 6	Pressing to disk (\varnothing 1 in) with 100 kN
Step 7	Heating with $2^\circ\text{C}/\text{min}$
Step 8	Sintering 3 d at 1200°C
Step 9	Cooling with $-5^\circ\text{C}/\text{min}$

Table B.5: Laser ablation parameters for the fabrication of epitaxial double-perovskite $\text{Sr}_2\text{FeMoO}_6$ thin films.

Laser parameters	
Laser	Lambda Physik LPX301i
Laser energy	550 mJ measured with internal energy monitor
Frequency	5 Hz
Parameters during deposition	
Temperature	$300^\circ\text{C} - 950^\circ\text{C}$
Pressure (O_2)	$10^{-5} \text{ Pa} - 10^1 \text{ Pa}$
Deposition rate (10^{-2} Pa O_2)	$0.3 \text{ \AA}/\text{pulse}$
Pressure (Ar)	10 Pa
Deposition rate (10 Pa Ar)	$0.09 \text{ \AA}/\text{pulse}$
Distance	55 mm
Parameters after deposition	
Cooling in the constant background pressure	

Table B.6: *Patterning parameters for epitaxial $\text{La}_{0.67}\text{Ca}_{0.33}\text{MnO}_3$ and $\text{La}_{0.67}\text{Sr}_{0.33}\text{MnO}_3$ thin films.*

Photolithographic parameters	
Photoresist	ma-P 275
Spin coater	30 s, 5000 turns/min
Baking	10 min, 120°C
Exposure time	60 s
Developing agent	ma-D 331
Developing time	≈ 90 s
	under visual examination
Wet chemical etching parameters	
Etching solution	50 H_2O_2 : 1 H_2SO_4 : 1000 H_2O
Etching time	≈ 2 min
	under visual examination

Table B.7: *Patterning parameters for epitaxial double-perovskite $\text{Sr}_2\text{FeMoO}_6$ thin films.*

Photolithographic parameters	
Photoresist	ma-P 275
Spin coater	30 s, 5000 turns/min
Baking	15 min, 100°C
Exposure time	60 s
Developing agent	ma-D 331
Developing time	1 min – 2 min
	under visual examination
Wet chemical etching parameters	
Etching solution	The developing agent contains water and etches directly the thin film which is not resistant against water.

Appendix C

Rietveld refinement with FULLPROF

FULLPROF is a program to simulate and to refine powder diffraction data (X-rays or neutron) [72, 192]. It is a structure refinement method and not a structure solution method, i.e. the starting model must be close to the correct model to find a global minimum. More than 160 parameters, instrumental parameters and crystal parameters, can be fitted simultaneously by a least-squares minimization technique, named the Rietveld method [68, 69]. The most important of them are explained in the following. A complete, but hardly structured explanation is found in Ref. [192].

It is important to have some kinds of indicators reported at each cycle of the Rietveld refinement process so that one can judge whether or not the refinement proceeds satisfactorily. Several so called R factors (reliability factors) which are now commonly used have been developed [193, 194, 195]:

- R -structure factor:

$$R_F = \frac{\sum |I_K(\text{'obs'})^{1/2} - I_K(\text{calc})^{1/2}|}{\sum I_K(\text{'obs'})^{1/2}} \quad (\text{C.1})$$

- R -Bragg factor:

$$R_B = \frac{\sum |I_K(\text{'obs'}) - I_K(\text{calc})|}{\sum I_K(\text{'obs'})} \quad (\text{C.2})$$

- R -pattern factor:

$$R_p = \frac{\sum |y_i(\text{obs}) - y_i(\text{calc})|}{\sum y_i(\text{obs})} \quad (\text{C.3})$$

or

$$R_p = \frac{\sum |y_i(\text{obs}) - y_i(\text{calc})|}{\sum |y_i(\text{obs}) - y_i(\text{bg})|} \quad (\text{C.4})$$

- R -weighted pattern factor:

$$R_{\text{wp}} = \left\{ \frac{\sum w_i (y_i(\text{obs}) - y_i(\text{calc}))^2}{\sum w_i (y_i(\text{obs}))^2} \right\}^{1/2} \quad (\text{C.5})$$

or

$$R_{\text{wp}} = \left\{ \frac{\sum w_i (y_i(\text{obs}) - y_i(\text{calc}))^2}{\sum w_i (y_i(\text{obs}) - y_i(\text{bg}))^2} \right\}^{1/2} \quad (\text{C.6})$$

- R -expected factor:

$$R_{\text{exp}} = \left\{ \frac{N - P}{\sum w_i (y_i(\text{obs}))^2} \right\}^{1/2} \quad (\text{C.7})$$

Here K represents the Miller indices, hkl , for a Bragg reflection, y_i is the intensity at the i th step (obs=observed, calc=calculated, bg=background), and I_K is the intensity assigned to the K th Bragg reflection at the end of the refinement cycles. The weight w_i is given by

$$\frac{1}{w_i} = \sigma_i^2(\text{obs}) + \sigma_i^2(\text{bg}) = y_i(\text{obs}) + y_i(\text{bg}) \quad (\text{C.8})$$

with $\sigma_i(\text{obs})$ and $\sigma_i(\text{bg})$ the respective standard deviations which are based only on counting statistics. The values N and P are the number of data points and refinable parameters, respectively. In the formula ‘obs’ is put in quotation marks because the Bragg intensity I_K is rarely observed directly. Instead the I_K values are obtained from an allocation of the total observed intensity in a large amount of overlapping reflections to the individual reflections, according to the ratios of those reflection intensities in the calculated pattern.

Because the factors R_{F} and R_{B} are based not on actually Bragg intensities but on those deduced with the help of the model, they are biased in favour of the model being used. None the less, they are most comparable to the conventional values R_{F} and R_{B} quoted in literature on single-crystal (sc) structure refinements (F is the structure factor):

- R -structure factor:

$$R_{\text{F}}^{\text{sc}} = \frac{\sum \left| |F(\text{obs})| - |F(\text{calc})| \right|}{\sum |F(\text{obs})|} \quad (\text{C.9})$$

- R -Bragg factor:

$$R_{\text{B}}^{\text{sc}} = \frac{\sum \left| |F(\text{obs})|^2 - |F(\text{calc})|^2 \right|}{\sum |F(\text{obs})|^2} \quad (\text{C.10})$$

From a mathematical point of view, R_{wp} is the most meaningful R -value because the numerator is the residual being minimized (see Eq. 1.17). For the same reason, it best reflects the progress of the refinement. Another useful numerical criterion is the 'goodness-of-fit' $S = R_{wp}/R_{exp}$.

The input/output control file to refine the raw data *FILENAME.pcr* must be prepared by the user with a file editor. It has the following form (emphasized and underlined numbers explaining the meaning of the parameter above are listed after the file):

```

COMM Ca2FeRe06 D2b 548K
! Files => DAT-file: cafer548k, PCR-file: Ph2T548K
! Job Npr Nph Nba Nex Nsc Nor Dum Iwg Ilo Ias Res Ste Nre Cry Uni Cor
  1  5  2  0  2  0  0  0  1  0  0  0  0  0  0  0  0  0  0  0
  1 2 3 4 5 6 7 8 9 10 11 12 13 14 15 16 17
!
! Ipr Ppl Ioc Mat Pcr Ls1 Ls2 Ls3 Syo Prf Ins Rpa Sym Hkl Fou Sho Ana
  0  0  1  0  1  0  0  0  0  0  1  6  1  1  1  1  0  0
  18 19 20 21 22 23 24 25 26 27 28 29 30 31 32 33 34
!
! Lambda1 Lambda2 Ratio Bkpos Wdt Cthm muR AsyLim Rpolarz
1.598000 1.598000 1.0000 90.0000 6.0000 0.0000 0.0000 90.00 0.0000
  35 36 37 38 39 40 41 42 43
!
! NCY Eps R_at R_an R_pr R_gl Thmin Step Thmax PSD Sent0
  2 0.00 0.15 0.15 0.15 0.15 -7.4500 0.0500 162.0000 0.000 0.000
  44 45 46 47 48 49 50 51
!
! Excluded regions (LowT HighT)
  -10.00 10.00
  150.00 160.00
  5b
!
! Additional scattering factors
MM03 0.000 0.000 1
101 102 103 104
-1.92026 2.00000 0.11360 4.02526 2.70283 6.45950 0.0000 0.0000 0.0000
  105
!
  56 !Number of refined parameters
  52
!
! Zero Code Sycos Code Sysin Code Lambda Code MORE
0.0261 291.00 0.0000 0.00 0.0000 0.00 0.000000 0.00 0
  53 P 54 P 55 P 56 P 57
! Background coefficients/codes
41.427 22.717 7.5733 -42.176 5.8657 36.410
  58
21.000 31.000 41.000 51.000 61.000 71.000
  P P P P P P
!-----
! Data for PHASE number: 1 ==> Current R_Bragg: 4.45
!-----
LA nuclear
!
! Nat Dis Mom Pr1 Pr2 Pr3 Jbt Irf Isy Str Furth ATZ Nvk Npr More
  6 0 0 0.0 0.0 1.0 0 0 0 0 0 0.00 0 5 0
  59 60 61 62 63 64 65 66 67 68 69 70 71
!
P 21/N <--Space group symbol

```

```

72
!Atom Typ      X      Y      Z      Biso      Occ      In Fin N_t /Codes
RE RE          0.00000 0.50000 0.00000 -0.04470 0.50000  0  0  0
73 74
          0.00      75      0.00      76      77      78 79 80
          P          P          P          P          P
FE FE          0.50000 0.00000 0.00000 0.43190 0.50000  0  0  0
          0.00      0.00      0.00      241.00  971.00
          P          P          P          P          P
CA CA          0.01282 0.04315 0.74838 0.91190 1.00000  0  0  0
          401.00  411.00  421.00  251.00  0.00
          P          P          P          P          P
O1  0          0.29142 0.29403 0.95906 0.49347 1.00000  0  0  0
          431.00  441.00  451.00  261.00  0.00
          P          P          P          P          P
O2  0          0.29958 0.29175 0.53887 1.02286 1.00000  0  0  0
          461.00  471.00  481.00  271.00  0.00
          P          P          P          P          P
O3  0          0.92061 0.47911 0.75144 0.74110 1.00000  0  0  0
          491.00  501.00  511.00  281.00  0.00
          P          P          P          P          P
! Scale      Shape1      Bov      Str1      Str2      Str3      Strain-Model
0.17360      0.2123      0.2000      0.0000      0.0000      0.0000      0
          81      82      83      84
          11.00000  301.00      0.00      0.00      0.00      0.00
          P          P          P          P          P
!      U      V      W      X      Y      GauSiz      LorSiz      Size-Model
0.03292      -0.06066  0.06891  0.00000  0.00000  0.00000  0.00000  0
          85      86      87      88      89      90
          311.00  321.00  331.00  0.00  0.00  0.00  0.00
          P          P          P          P          P          P
!      a      b      c      alpha      beta      gamma
5.436713  5.539096  7.734533  90.000000  90.041847  90.000000
          106
          341.00000  551.00000  351.00000  0.00000  361.00000  0.00000
          P          P          P          P          P          P
! Pref1 Pref2 Asy1 Asy2 Asy3 Asy4
0.00000 0.00000 0.04941 0.00000 0.00000 0.00000
          7b      42b
          0.00  0.00  81.00  0.00  0.00  0.00
          P          P          P          P          P          P
!-----
! Data for PHASE number:  2 ==> Current R_Bragg:      8.18
!-----
LA magnetic
!
!Nat Dis Mom Pr1 Pr2 Pr3 Jbt Irf Isy Str Furth      ATZ      Nvk Npr More
  4  0  0  0.0  0.0  1.0  1  0  1  0  0      0.00  0  5  0
!
P -1      <--Space group symbol
!Nsym Cen Laue MagMat
  1  1  1  1
  91 92 93 94
!S11 S12 S13      T1      S21 S22 S23      T2      S31 S32 S33      T3
!M11 M12 M13 M21 M22 M23 M31 M32 M33      Ph
  1  0  0  0.000000  0  1  0  0.000000  0  0  1  0.000000
          95
  1  0  0  0  1  0  0  0  1  0.000000
          96
!Atom Typ      Mag Vek      X      Y      Z      Biso      Occ      Rx      Ry      Rz
RE1 MM03  1  0  0.00000 0.50000 0.00000 -0.04470 1.00000 -0.089 -0.089 0.023
          97 98 99
          100

```

```

          0.00  0.00  1.00  231.00  0.00  521.00  521.00  0.00
0.000  0.000  0.000  0.000  0.000  0.000  0.000000
0.00  0.00  0.00  0.00  0.00  0.00  0.00
RE2  MM03  1  0  0.50000  0.00000  0.50000-0.04470  1.00000  -0.089  -0.089  0.023
          0.00  0.00  1.00  231.00  0.00  521.00  521.00  0.00
0.000  0.000  0.000  0.000  0.000  0.000  0.000000
0.00  0.00  0.00  0.00  0.00  0.00  0.00
FE1  MFE3  1  0  0.50000  0.00000  0.00000  0.43190  1.00000  0.997  0.997  0.023
          0.00  0.00  1.00  241.00  0.00  531.00  531.00  0.00
0.000  0.000  0.000  0.000  0.000  0.000  0.000000
0.00  0.00  0.00  0.00  0.00  0.00  0.00
FE2  MFE3  1  0  0.00000  0.50000  0.50000  0.43190  1.00000  0.997  0.997  0.023
          0.00  0.00  1.00  241.00  0.00  531.00  531.00  0.00
0.000  0.000  0.000  0.000  0.000  0.000  0.000000
0.00  0.00  0.00  0.00  0.00  0.00  0.00
!  Scale      Shape1      Bov      Str1      Str2      Str3      Strain-Model
0.17360      0.1858      0.2000      0.0000      0.0000      0.0000      0
      11.00000      301.00      0.00      0.00      0.00      0.00
!  U          V          W          X          Y          GauSiz      LorSiz      Size-Model
0.09861  -0.14266  0.11168  0.00000  0.00000  0.00000  0.00000  0
      311.00      321.00      331.00      0.00      0.00      0.00      0.00
!  a          b          c          alpha      beta          gamma
5.436713  5.539096  7.734533  90.000000  90.041847  90.000000
341.00000  551.00000  351.00000  0.00000  361.00000  0.00000
!  Pref1 Pref2 Asy1 Asy2 Asy3 Asy4
0.00000  0.00000  0.04941  0.00000  0.00000  0.00000
0.00  0.00  81.00  0.00  0.00  0.00

```

The first row and rows beginning with ! are only comments. The current R_B values of each phase are as well listed in these rows. The lines **LA nuclear** and **LA magnetic** signal use of nuclear or magnetic scattering. All values marked with P (omitted in the magnetic phase) below can be refined. The codeword 0.00 means the refinable parameter above will not be fitted whereas the refined parameters are numbered with values below serially in the following form for the codeword: 11.00, 21.00, ..., 561.00(= N1.00, N = 56, parameter 56). The value 1.00 after N influences the modification of this parameter after each cycle, i.e. the computed shift is multiplied by this factor before use (usually one for all parameters). The refinable parameters are explained in the following:

1: Job = 0 X-rays or Job = 1 neutrons (nuclear and magnetic scattering) select the source of the pattern in the refinement. For Job = 2 and Job = 3 a calculated pattern is created with the name *FILENAME.sim* for the respective source.

2: The peak shape is selected, Npr = 0 Gaussian curve G :

$$G = \frac{\sqrt{4 \ln 2}}{H_K \sqrt{\pi}} \exp \left(\frac{-4 \ln 2 (2\theta_i - \theta_K)^2}{H_K^2} \right) \quad (\text{C.11})$$

with H_K the full width at half maximum (FWHM). Npr = 2 Lorentz curve:

$$L = \frac{2}{H_K \pi} \cdot \frac{1}{1 + \frac{4(2\theta_i - \theta_K)^2}{H_K^2}} \quad (\text{C.12})$$

$\text{Npr} = 5$ pseudo-Voigt. The function is a mixture of a Lorentz curve L and a Gaussian curve G :

$$P(2\theta_i - \theta_K) = \eta L + (1 - \eta)G \quad \eta = \eta_0 + X \cdot 2\theta \quad (\text{C.13})$$

with a mixing parameter η which can be refined as a linear function of 2θ with variables η_0 (see [82](#)) and X (see [86](#)).

[3](#): Number of crystallographic and magnetic phases, (max: $\text{Nph} = 8$, here $\text{Nph} = 2$).

[4](#): $\text{Nba} = 0$ refine background with a fifth-order polynomial

$$y_i(\text{bg}) = \sum_{m=0}^5 B_m \left[\frac{2\theta_i}{\text{Bkpos}} - 1 \right]^m \quad (\text{C.14})$$

with B_m the refinable coefficients (see [58](#)) and Bkpos the user-specified origin of the polynomial (see [38](#)). The background intensity may also be obtained from a operator-supplied file or from a linear interpolation between operator-selected points in the pattern [192].

[5](#): $\text{Nex} =$ number of excluded regions during refinement. It is helpful if e.g. a impurity phase is present. The ranges are defined with starting angle and end angle (see [5b](#)).

[6](#): $\text{Nsc} =$ number of scattering sets (zero in most cases, see Ref. [192]).

[7](#): Preferred orientation produces systematic distortions of the reflection intensities (see Eq. 1.18) and therefore corrections can be made for it. $\text{Nor} = 0$ the preferred orientation function is given by

$$P_K = \text{Pref2} + (1 - \text{Pref2}) \exp(-\text{Pref1} \cdot \alpha_K^2) \quad (\text{C.15})$$

with Pref1 and Pref2 are refinable parameters (see [7b](#)) and α_K the angle between the diffraction vector and the preferred axis defined in [62](#) [196]. This function is helpful if the degree of preferred orientation is not large. For higher degrees of preferred orientation the March-Dollase function $\text{Nor} = 1$ is used:

$$P_K = \text{Pref2} + (1 - \text{Pref2}) \left((\text{Pref1} \cdot \cos(\alpha_K))^2 + \frac{1}{\text{Pref1}} \sin^2(\alpha_K) \right)^{-3/2} \quad (\text{C.16})$$

[8](#): Zero in most cases, see Ref. [192].

[9](#): The refinement procedure is selected: $\text{Iwg} = 0$ standard least squares, $\text{Iwg} = 1$ maximum likelihood.

- 10: The parameter describes the used geometry: $I10 = 0$ standard Debye-Scherrer or Bragg-Brentano geometry and $I10 = 2$ transmission geometry.
- 11: Reflections are re-ordered after each cycle (equal to unity in most cases).
- 12: If $Res = 0$ then the resolution function of the instrument is not given. For $Res \neq 0$ the next line contains the file name including the resolution function [192].
- 13: If $Ste > 1$ the number of data points is reduced by the given factor. Only those points corresponding to the new step size $Ste \times Step$ are (see 48) taken into account in the refinement.
- 14: Nre is the number of parameters to be constrained within given limits. The numerator of Eq. C.7 changes to $N - P + Nre$. At the end of the control file a list specifying the number and the limit of each parameter must be given. See also Ref. [195, 192].
- 15: Zero in most cases, see Ref. [192].
- 16: The unit of the scattering variable is selected: $Uni = 0$ means 2θ in degrees, $Uni = 1$ means time-of-flight in microseconds.
- 17: If $Cor \neq 0$ then a file *FILENAME.cor* with intensity corrections is read. The corrections are applied to the integrated intensities as a multiplicative constant [192].
- 18: $Ipr = 1$: The observed and calculated profile intensities are listed in a output file *FILENAME.out*.
- 19: $Pp1 = 2$ generates the background file *FILENAME.bac*.
- 20: If $Ioc = 2$ then the reflections corresponding to second wavelength are also written in the file *FILENAME.out*.
- 21: For $Mat = 1$ the correlation matrix is as well written in the file *FILENAME.out*. With the help of the correlation matrix one can recognize redundant and strongly correlated parameters [197].
- 22: The control file *FILENAME.pcr* is simultaneously an input and output file, i.e. for $Pcr = 1$ it is overwritten with updated parameters. Therefore, it is wise to save a copy of this file with a different name from time to time. Another possibility is to set $Pcr = 2$. Then, a new input file *FILENAME.new* is generated.
- 23: With $Ls1 = 1$ a reflection list is written in the file *FILENAME.out*.

- 24: Zero in most cases, see Ref. [192].
- 25: Zero in most cases, see Ref. [192].
- 26: If the parameter **Syo** = 1 then the symmetry operators are tabulated in the file *FILENAME.out*.
- 27: With the parameter **Prf** different formats of an output file for plot programs as e.g. WINPLOTTR (**Prf** = 1) or KALEIDAGRAPH (**Prf** = 3) can be chosen.
- 28: The parameter **Ins** describes the used format of the data: **Ins** = 6 is the standard D2B format (neutrons) or **Ins** = 10 is a standard X, Y format (2θ , intensity) used e.g. for X-rays. In the latter case the first line begins with the keyword **XYDATA** and then the following 5 lines starting with ! are considered as the heading of the file [192].
- 29: If **Rpa** = 1 then a summary of the refined parameters are listed in an output file *FILENAME.rpa*. If the file already exists the new data are appended at the end.
- 30: An output file *FILENAME.sym* with a list of symmetry operators is created if **Sym** = 1 and **Syo** = 1 (see 26).
- 31: If **Hk1** = 1 then an output file *FILENAME.hkl* is created with a complete list of reflections of each phase.
- 32: If **Fou** = 1 then an output file *FILENAME.fou* is created with a complete list of structure factors.
- 33: With **Sho** = 1 the output from each cycle is suppressed. Only the information from the last cycle is printed.
- 34: If **Ana** = 1 then an analysis of the refinement is printed at the end of the output summary file *FILENAME.sum*.
- 35: **lambda1** = the first wavelength in Ångström.
- 36: **lambda2** = the second wavelength in Ångström (= **lambda1** for monochromatic beam).
- 37: **Ratio** = the intensity (*I*) ratio $I(\text{lambda2})/I(\text{lambda1})$
- 38: The parameter **Bkpos** is the origin in 2θ of the polynomial function for the background (see 4).

39: The width of the calculated profile is determined by the parameter `Wdt` in units of the FWHM H_K (typically 2.5 for Gaussian and 7 for Lorentzian). If the parameter is too small then remaining intensities will be taken into account by the background function. If the parameter is too large, on the other hand, then the refinement procedure becomes too long due to a large amount of overlapping reflections.

40: `Cthm` = the coefficient for monochromator polarization correction in Bragg-Brentano or Debye-Scherrer geometry [198]. The Lorentz polarization factor L_P is given by

$$L_P = \frac{1 - \text{Rpolarz} + \text{Rpolarz} \cdot \cos^2(2\theta_M) \cos^2(2\theta)}{2 \sin^2(\theta) \cos(\theta)} \quad (\text{C.17})$$

with $\text{Cthm} = \cos^2(2\theta_M)$. With a graphite monochromator the parameter `Cthm` is 0.8351 and 0.7998 for Cu $K\beta$ and Cu $K\alpha$, respectively. The parameter `Rpolarz` (see 43) is used only for synchrotron data (for neutrons `Rpolarz` = 0 and for characteristic X-ray radiation `Rpolarz` = 0.5). For transmission flat-plate geometry see [192].

41: `muR` = the absorption correction coefficient for Debye-Scherrer data which is the product of the linear absorption coefficient and the radius of the cylindrical sample [192, 198]. For flat plates in transmission geometry or for corrections in Bragg-Brentano geometry see Ref. [192].

42: The shape of the peaks below `AsyLim` (in degrees) is corrected (asymmetry correction [192]) by a formula which depends on four refinable parameters `Asy1`, `Asy2`, `Asy3`, and `Asy4` (see 42b) [199]. For further details see Ref. [192, 200].

43: `Rpolarz` = the polarization factor (see 40) [192].

44: `NCY` = the number of cycles of the refinement process.

45: Zero in most cases, see Ref. [192].

46: The parameters are the four relaxation factors for shifts [192]:

- `R_at` = atomic parameters as coordinates, magnetic moments, site occupancies and isotropic displacement (temperature) factors.
- `R_an` = anisotropic displacement (temperature) factors.
- `R_pr` = profile parameters, asymmetry, overall displacement (temperature), cell constants, preferred orientation parameters, strains, size, propagation vectors and user-supplied parameters.

- **R_gl** = global parameters as zero-shift, background, displacement and transparency.

They influence only the modification of parameters after each cycle.

47: **Thmin** = starting angle 2θ for calculated pattern in degrees.

48: **Step** = step size $\Delta 2\theta$ in degrees.

49: **Thmax** = end angle 2θ for calculated pattern in degrees.

50: The parameter **PSD** describes the incident beam angle at sample surface in degrees.

51: **Sent0** = the angle in degrees at which the sample intercepts completely the X-ray beam. Below **Sent0** a part of the beam doesn't touch the sample and the intensity of reflections below this value have to be multiplied by the factor $\sin(\theta)/\sin(\text{Sent0})$

52: The value is the number of parameters in the refinement (here $N = 56$). If $N = 0$ then no refinement takes place. At the beginning of the refinement procedure this is helpful to tune parameters by hand.

53: **Zero** = zero point for 2θ in degrees: $2\theta(\text{true}) = 2\theta(\text{obs}) - \text{Zero}$

54: The parameter **Sycos** describes the systematic 2θ shift due to sample displacement given by

$$\Delta(2\theta) = 2 \cdot \Delta\theta = 2 \cdot \frac{s}{R} \cos(\theta) \equiv \text{Sycos} \cdot \cos(\theta) \quad (\text{C.18})$$

with s the displacement of the sample with respect to the axis of the goniometer, R the radius of the goniometer circle, and $\Delta 2\theta$ in radian [192]. As the angles are expressed in degrees in FULLPROF, the sample offset is given by

$$s = \frac{\pi}{180} \cdot R \cdot \text{Sycos}. \quad (\text{C.19})$$

55: **Sysin** = systematic 2θ shift with $\sin(2\theta)$ dependence due to the sample transparency coefficient [192].

56: One wavelength = **Lambda** can also be refined.

57: If **MORE** $\neq 0$ then read in following line the microabsorption coefficients [192].

58: In this row the six background coefficients B_m are listed (see 4).

- 59: `Nat` = number of crystallographic unequal atomic positions in unit cell (asymmetric unit).
- 60: `Dis` = number of distance constraints [192].
- 61: `Mom` = number of magnetic moment constraints [192].
- 62: The parameters `Pr1`, `Pr2`, and `Pr3` define the preferred orientation direction in reciprocal space (see 7).
- 63: If `Jbt` = 0 then the phase will be refined with the Rietveld Method in a given structural model. A profile matching mode with constant or variable scale factor is also possible with `Jbt` = 2 and `Jbt` = 3, respectively [192]. If `Jbt` = 1 then the phase is treated with the Rietveld method and it is considered as pure magnetic. In the latter case only magnetic atoms are required. In order to obtain the correct values of the magnetic moments the scale factor and structural parameters must be constrained to have the same values as their crystallographic counterpart.
- 64: If `Irf` = 0 then the list of reflections for this phase is automatically generated from the space group symbol. The reflection list can also be read from a file [192].
- 65: If `Isy` = 0 then the symmetry operators are generated automatically from the space group symbol. In the case of a pure magnetic phase (`Jbt` = 1) the parameter `Isy` must be always equal to one. Then, the symmetry operators are listed separately (see 91).
- 66: Zero in most cases, see Ref. [192].
- 67: The parameter fixes the number of further parameters defined by user.
- 68: Zero in most cases, see Ref. [192].
- 69: Zero in most cases, see Ref. [192].
- 70: Beside the general peak shape given in 2 an individual peak shape can be chosen for the present phase.
- 71: If `MORE` \neq 0 then a new line is read to create further output files which can be e.g. used as input files in other programs like SCHAKAL. A list of all atoms within the unit cell can as well be created [192].
- 72: Space group symbol, e.g. P 21/n, P 42/m, I 4 m m. For a cubic space group the old notation is used, e.g. F m 3 m instead of F m -3 m. Upper and/or lower case characters can be used. It is advisable to check the symmetry operators in the output file (see 26 or 30).

- 73: Identification characters for an atom, e.g. CA or FE1.
- 74: The parameter is a link to scattering data (atomic scattering factor) for the respective atom, e.g. FE (use only upper case letters) for iron.
- 75: Fractional atomic coordinates inside the unit cell.
- 76: The parameter **Biso** is the isotropic displacement (temperature) parameter in square of Ångström (see 83).
- 77: **Occ** = occupation number, i.e. multiplicity of the respective position (here two for Fe or Re and four for Ca or O) divided by the multiplicity of the general position of the group (here four). If these parameters are refined one can gain the stoichiometry of the sample.
- 78: Zero in most cases, see Ref. [192].
- 79: Zero in most cases, see Ref. [192].
- 80: If **N_t** = 0 then the respective atom is assumed to be isotropic, i.e. only one temperature factor is required. If the atom is anisotropic **N_t** = 1 then the anisotropic temperature factors (six tensor components B_{ij} [201]) together with the codewords are given in two additional lines. For the magnetic phase these additional lines are always required [192].
- 81: **Scale** = the scale factor of the phase. This parameter is important for a quantitative phase analysis. The relative weight fraction W_p of phase p in a mixture of n phases is given by

$$W_p = \frac{\text{Scale}_p Z_p M_p V_p}{\sum_{i=1}^n \text{Scale}_i Z_i M_i V_i} \quad (\text{C.20})$$

with Z the number of formula units per unit cell, M the formula unit in atomic mass units, and V the unit cell volume [202].

- 82: **Shape1** = the profile shape parameter, i.e. η_0 if **Npr** = 5 (see 2).
- 83: At the beginning of a refinement procedure a common temperature factor is assumed for all atoms [201]. The parameter is given by

$$\text{Bov} = 8\pi^2 \overline{u_s^2} \quad (\text{C.21})$$

with $\overline{u_s^2}$ the root-mean square thermal displacement in square of Ångström defined in Eq. 5.2. In an advanced stage of the Rietveld refinement for each atom an additional individual atomic temperature factor **Biso** (see 76) is refined. Equation C.21 changes to

$$\text{Bov} + \text{Biso} = 8\pi^2 \overline{u_s^2} \quad (\text{C.22})$$

84: **Str1, Str2, Str3** = strain parameters [192].

85: Angle dependence of the FWHM H_K (see number 2). For a Gaussian curve it is given by

$$H_K = U \tan^2(\theta) + V \tan(\theta) + W + \frac{\text{GauSiz}}{\cos^2(\theta)} \quad (\text{C.23})$$

where **U, V, W**, and **GauSiz** (see 88) are the refinable parameters characterizing the instrumental resolution function [65, 203].

86: For a Lorentz curve the FWHM H_K is given by

$$H_K = X \tan(\theta) + \frac{Y + \text{LorSiz}}{\cos(\theta)} \quad (\text{C.24})$$

with **X, Y** (see 87), and **LorSiz** (see 89) refinable parameters.

87: One parameter in Eq. C.24.

88: **GauSiz** = the isotropic size parameter of gaussian character (see 85). It is only $\neq 0$ if **Npr** = 7

89: The parameter **LorSiz** (see Eq. C.24) is only $\neq 0$ if **Npr** = 7.

90: One can select a model for **LorSiz**. Zero in most cases, see Ref. [192].

91: **Nsym** = number of symmetry operators.

92: **Gen** = 1 non-centrosymmetric structure.

93: The parameter **Laue** is an integer which corresponds to a laue class (1:(-1), 3:(*mmm*), ..., 14:(*m3m*)). The number is used to check the symmetry operators given by the user.

94: **MagMat** = number of magnetic rotation matrices for each symmetry operator.

95: The symmetry operator (here identity) is given in this row in numeric form. If **Isy** = -1 then it is given in alpha-numeric form [192].

96: The rotation matrix (here unit matrix) is as well given in the numeric form [192].

97: The parameter is a link to scattering data. The character **M** followed by the chemical symbol and formal charge state means take the magnetic form factor for the respective atom. In this case the value for Re^{+5} is not known and therefore it is approximated with the value of Mo^{+3} . This value is known but not tabulated and hence it is given separately (see 101).

98: *Mag* = ordinal number of the magnetic rotation matrix.

99: *Vec* = number of propagation vectors to which the atom contributes (required for incommensurate structures).

100: *Rx, Ry, Rz* = components along the crystallographic axes of the magnetic moments in Bohr magnetons. If *Jbt* = -1 then the three parameters correspond to the spherical components of the magnetic moment [192].

101: The symbol identifies this set (here *MM03*)

102: Zero in most cases, see Ref. [192].

103: Zero in most cases, see Ref. [192].

104: If the parameter is equal to one then a magnetic form factor is given in the following line.

105: This line contains the coefficients for the analytical approximation to the magnetic form factor.

106: Cell parameters: lattice constants and angles.

The program was used under Windows95/NT together with WINPLOTR, a program for graphical representation of the patterns [204]. The input/output file was further used for the graphical representation of the monoclinic unit cell (see e.g. Fig. 5.3) with the program STRUPLO [205].

Do not start by refining all parameters at the same time. A sensible sequence of refinement is the following:

1. scale factor
2. ... + zero point of detector + 1st background parameter + lattice constants
3. ... + atomic positions + overall Debye-Waller factor
4. ... + peak shape function and asymmetry parameters
5. ... + atom occupancies (if required)
6. ... + individual isotropic thermal parameters
7. ... + additional background parameters
8. ... + *Sycos* + *Sysin*

The output file has to be carefully checked after each refinement. For instance thermal and peak shape function parameters can become poorly defined and act as a dumping ground for systematic errors.

Bibliography

- [1] G. A. Prinz, Phys. Today **48**, 58 (1995).
- [2] J. M. Kikkawa and D. D. Awschalom, Nature (London) **397**, 139 (1999).
- [3] P. Grünberg, R. Schreiber, Y. Pang, M. B. Brodsky, and H. Sowers, Phys. Rev. Lett. **57**, 2442 (1986).
- [4] M. N. Baibich, J. M. Broto, A. Fert, D. F. Van Nguyen, F. Petroff, P. Etienne, G. Creuzet, A. Friedrich, and J. Chazelas, Phys. Rev. Lett. **61**, 2472 (1988).
- [5] <http://www.storage.ibm.com/hardsoft/diskdrdl/technolo/gmr/gmr.htm>.
- [6] J. Wecker and J. Bangert, in *Magnetische Schichtsysteme in Forschung und Anwendung, Vorlesungsmanuskripte des 30. Ferienkurses* (Institut für Festkörperforschung, Forschungszentrum Jülich GmbH, 1999), p. D 6.5.
- [7] K. Kobayashi, T. Kimura, H. Sawada, K. Terakura, and Y. Tokura, Nature (London) **395**, 677 (1998).
- [8] R. M. Hazen, Spektrum der Wissenschaft **8**, 42 (1988).
- [9] *Perovskite: A Structure of Great Interest in Geophysics and Materials Science*, Vol. 45 of *Geophysical Monograph*, edited by A. Navrotsky and D. J. Weidner (American Geophysical Union, Washington, 1989).
- [10] *Humboldts travels in Siberia (1837 – 1842): the gemstones; Russian gemstones in the early part of the 19th century; extracts and commentaries on Reise nach dem Ural, Altai und dem Kaspischen Meer by Gustav Rose*, translation and commentary by J. Sinkankas, edited by G. M. Sinkankas (Geoscience Press, Phoenix, 1994).
- [11] H. D. Megaw, Proc. Phys. Soc. (London) **58**, 133 (1946).
- [12] H. F. Kay and P. C. Bailey, Acta Crystallogr. **10**, 219 (1957).

- [13] F. S. Galasso, *Perovskites and High T_c Superconductors* (Gordon and Breach Science Publishers, New York, 1990), p. 223.
- [14] O. Hassel, *Kristallchemie*, Vol. XXXIII of *Wissenschaftliche Forschungsberichte, Naturwissenschaftliche Reihe* (Verlag von Theodor Steinkopf, Dresden, 1934), p. 18.
- [15] G. H. Jonker and J. H. Van Santen, *Physica* (Amsterdam) **XVI**, 337 (1950).
- [16] G. H. Jonker and J. H. Van Santen, *Physica* (Amsterdam) **XIX**, 120 (1953).
- [17] G. H. Jonker, *Physica* (Amsterdam) **XXII**, 707 (1956).
- [18] J. H. Van Santen and G. H. Jonker, *Physica* (Amsterdam) **XVI**, 599 (1950).
- [19] G. H. Jonker, *Physica* (Amsterdam) **XX**, 1118 (1954).
- [20] L. Kelvin, *Mathematical and Physical Papers* (Cambridge University Press, London, 1884), Vol. 2, p. 307.
- [21] J. Volger, *Physica* (Amsterdam) **XX**, 49 (1954).
- [22] J. B. Goodenough and J. M. Longo, in *Landolt-Börnstein*, Vol. 4a of *New Series, group III*, edited by K.-H. Hellwege and A. M. Hellwege (Springer, Berlin, 1970), p. 126.
- [23] R. M. Kusters, J. Singleton, D. A. Keen, R. McGreevy, and W. Hayes, *Physica B* **155**, 362 (1989).
- [24] R. von Helmolt, J. Wecker, B. Holzapfel, L. Schultz, and K. Samwer, *Phys. Rev. Lett.* **71**, 2331 (1993).
- [25] A. Urushibara, Y. Moritomo, T. Arima, A. Asamitsu, G. Kido, and Y. Tokura, *Phys. Rev. B* **51**, 14103 (1995).
- [26] J. B. Goodenough, *Magnetism and the Chemical Bond* (Wiley-Interscience, New York, 1996).
- [27] S. Satpathy, Z. S. Popović, and F. R. Vakažlović, *J. Appl. Phys.* **79**, 4555 (1996).
- [28] I. Solovyev, N. Hamada, and K. Terakura, *Phys. Rev. Lett.* **76**, 4825 (1996).
- [29] W. Westerburg, Master's thesis, Johannes Gutenberg-Universität Mainz, 1998.
- [30] P. Schiffer, A. P. Ramirez, W. Bao, and S.-W. Cheong, *Phys. Rev. Lett.* **75**, 3336 (1995).

- [31] S.-W. Cheong and C. H. Chen, in *Colossal Magnetoresistance, Charge Ordering and Related Properties of Manganese Oxides*, edited by C. N. R. Rao and B. Raveau (World Scientific, Singapore, 1998), p. 241.
- [32] Y. Tomioka and Y. Tokura, in *Colossal Magnetoresistive Oxides*, Vol. 2 of *Advances in Condensed Matter Science*, edited by Y. Tokura (Gordon and Breach Science Publishers, Singapore, 2000), p. 281.
- [33] J. M. D. Coey, M. Viret, and S. von Molnár, *Adv. Phys.* **48**, 167 (1999).
- [34] C. Zener, *Phys. Rev.* **82**, 403 (1951).
- [35] P. W. Anderson and H. Hasegawa, *Phys. Rev.* **100**, 675 (1955).
- [36] P. de Gennes, *Phys. Rev.* **118**, 141 (1960).
- [37] J. Kanamori, *J. Phys. Chem. Solids* **10**, 87 (1959).
- [38] J. B. Goodenough, *Phys. Rev.* **100**, 564 (1955).
- [39] J. C. Phillips, *Phys. Rev.* **133A**, 1020 (1964).
- [40] P. M. Tedrow and R. Meservey, *Phys. Rev. B* **7**, 318 (1973).
- [41] Y. Okimoto, T. Katsufuji, T. Ishikawa, A. Urushibara, T. Arima, and Y. Tokura, *Phys. Rev. Lett.* **75**, 109 (1995).
- [42] J.-H. Park, C. T. Chen, C.-W. Cheong, W. Bao, G. Meigs, V. Chakarian, and Y. U. Idzerda, *Phys. Rev. Lett.* **76**, 4215 (1996).
- [43] W. E. Pickett and D. J. Singh, *J. Magn. Magn. Mater.* **172**, 237 (1997).
- [44] J.-H. Park, E. Vescovo, H.-J. Kim, C. Kwon, R. Ramesh, and T. Venkatesan, *Nature (London)* **392**, 794 (1998).
- [45] R. Meservey and P. M. Tedrow, *Phys. Rep.* **238**, 173 (1994).
- [46] R. J. Soulen Jr., J. M. Byers, M. S. Osofsky, B. Nadgorny, T. Ambrose, S. F. Cheng, P. R. Broussard, C. T. Tanaka, J. Nowak, J. S. Moodera, A. Barry, and J. M. D. Coey, *Science* **282**, 85 (1998).
- [47] E. H. Hall, *Am. J. Math.* **2**, 287 (1879).
- [48] R. Karplus and J. M. Luttinger, *Phys. Rev.* **95**, 1154 (1954).
- [49] I. A. Campbell and A. Fert, in *Ferromagnetic Materials*, edited by E. P. Wohlfarth (North Holland, Amsterdam, 1982), Vol. 3, p. 754.

- [50] S. V. Vonsovskii, *Magnetism* (John Wiley & Sons, New York, 1974), Vol. 1, p. 44.
- [51] C. M. Hurd, in *The Hall Effect in Metals and Alloys, The International Cryogenics Monograph Series*, edited by K. Mendelssohn and K. D. Timmerhaus (Plenum Press, New York, 1972), p. 158.
- [52] S. V. Vonsovskii, *Magnetism* (John Wiley & Sons, New York, 1974), Vol. 2, p. 1146.
- [53] L. Berger, *Phys. Rev. B* **2**, 4559 (1970).
- [54] N. W. Ashcroft and N. D. Mermin, *Solid State Physics*, international ed. (Saunders College, Philadelphia, 1976), p. 99.
- [55] H. Ibach and H. Lüth, *Solid-State Physics*, 3rd ed. (Springer, Berlin, 1991), p. 99.
- [56] H. Vanderstraeten, Ph.D. thesis, Katholieke Universiteit Leuven, 1991.
- [57] M. M. Woolfson, *An Introduction to X-ray Crystallography*, 2nd ed. (Cambridge University Press, London, 1997), p. 161.
- [58] J. A. Ibers, D. H. Templeton, B. K. Vainshtein, G. E. Bacon, and K. Lonsdale, in *Atomic Scattering Factors*, Vol. III Physical and Chemical Tables of *International Tables For X-ray Crystallography*, 2nd ed., edited by K. Lonsdale (Kynoch Press, Birmingham, 1968), p. 201.
- [59] M. A. Krivoglaz, *X-ray and Neutron Diffraction in Nonideal Crystals* (Springer, Berlin, 1996), p. 168.
- [60] G. E. Bacon, *Neutron Diffraction*, 3rd ed. (Clarendon Press, Oxford, 1975), p. 38.
- [61] U. Buchenau, in *Magnetismus von Festkörpern und Grenzflächen, Vorlesungsmanuskripte des 24. Ferienkurses* (Institut für Festkörperforschung, Forschungszentrum Jülich GmbH, 1993), p. 13.6.
- [62] G. E. Bacon, *Neutron Diffraction*, 3rd ed. (Clarendon Press, Oxford, 1975), p. 226.
- [63] W. Marshall and S. W. Lovesey, in *Theory of Thermal Neutron Scattering*, Vol. 5 of *The International Series of Monographs on Physics*, edited by W. Marshall and D. H. Wilkinson (Clarendon Press, Oxford, 1971), p. 173.
- [64] G. E. Bacon, *Neutron Diffraction*, 3rd ed. (Clarendon Press, Oxford, 1975), p. 202.

- [65] A. W. Hewat, *Mat. Sci. Forum* **9**, 69 (1986).
- [66] <http://www.ill.fr/YellowBook/D2B/>.
- [67] H. Ullmaier, in *Streumethoden zur Untersuchung kondensierter Materie, Vorlesungsmanuskripte des 27. Ferienkurses* (Institut für Festkörperforschung, Forschungszentrum Jülich GmbH, 1996), p. B 8.8.
- [68] H. M. Rietveld, *Acta Crystallogr.* **22**, 151 (1967).
- [69] H. M. Rietveld, *J. Appl. Cryst.* **2**, 65 (1969).
- [70] C. Giacovazzo, in *Fundamentals of Crystallography*, Vol. 2 of *International Union of Crystallography Texts on Crystallography*, edited by C. Giacovazzo (University Press, Oxford, 1992), p. 90.
- [71] E. Prince, in *The Rietveld Method*, Vol. 5 of *International Union of Crystallography Monographs on Crystallography*, edited by R. A. Young (University Press, Oxford, 1993), p. 43.
- [72] J. Rodríguez-Carvajal, *Physica B* **192**, 55 (1993).
- [73] F. Martin, Ph.D. thesis, Johannes Gutenberg-Universität Mainz, to be published 2001.
- [74] S. Friedrich, Master's thesis, Johannes Gutenberg-Universität Mainz, 1999.
- [75] Y. P. Lee, V. G. Prokhorov, J. Y. Rhee, K. W. Kim, G. G. Kaminsky, and V. S. Flis, *J. Phys.: Condens. Matter* **12**, L133 (2000).
- [76] M. Mauer, Master's thesis, Johannes Gutenberg-Universität Mainz, 1998.
- [77] M. Maier, Ph.D. thesis, Johannes Gutenberg-Universität Mainz, to be published 2001.
- [78] G. Jakob, Ph.D. thesis, Technische Hochschule Darmstadt, 1993.
- [79] M. Deutsch and M. Hart, *Phys. Rev. B* **26**, 5558 (1982).
- [80] N. Maskil and M. Deutsch, *Phys. Rev. A* **37**, 2947 (1988).
- [81] H. C. Wolfe, *Phys. Rev.* **43**, 221 (1933).
- [82] E. U. Condon and G. H. Shortley, *The Theory of Atomic Spectra* (Cambridge University Press, London, 1935), p. 323.
- [83] R. L. Snyder, in *The Rietveld Method*, Vol. 5 of *International Union of Crystallography Monographs on Crystallography*, edited by R. A. Young (University Press, Oxford, 1993), p. 118.

- [84] R. M. Langer, Phys. Rev. **37**, 457 (1931).
- [85] T. Steinborn, Ph.D. thesis, Technische Hochschule Darmstadt, 1994.
- [86] D. Reisinger, Master's thesis, Johannes Gutenberg-Universität Mainz, 2000.
- [87] <http://www-hfml.sci.kun.nl/hfml/20t-magnet.html>.
- [88] H. Fritzsche, in *Solid State Physics, Electrical, Magnetic, and Optical Properties*, Vol. 6, Part B of *Methods of experimental Physics*, edited by K. Lark-Horovitz and V. A. Johnson (Academic Press, New York, 1959), p. 152.
- [89] A. N. Gerritsen and W. J. de Haas, Physica (Amsterdam) **VII**, 802 (1940).
- [90] G. J. Snyder, M. R. Beasley, T. H. Geballe, R. Hiskes, and S. DiCarolis, Appl. Phys. Lett. **69**, 4254 (1996).
- [91] G. J. Snyder, R. Hiskes, S. DiCarolis, M. R. Beasley, and T. H. Geballe, Phys. Rev. B **53**, 14434 (1996).
- [92] P. Mandal, K. Bärner, L. Haupt, A. Poddar, R. von Helmolt, A. Jansen, and P. Wyder, Phys. Rev. B **57**, 10256 (1998).
- [93] K. Kubo and N. Ohata, J. Phys. Soc. Jpn. **33**, 21 (1972).
- [94] J. A. Fernandez-Baca, P. Dai, H. Y. Hwang, C. Kloc, and S.-W. Cheong, Phys. Rev. Lett. **80**, 4012 (1998).
- [95] D. Emin and T. Holstein, Ann. Phys. (N.Y.) **53**, 439 (1969).
- [96] K. Khazeni, Y. X. Jia, L. Lu, V. H. Crespi, M. L. Cohen, and A. Zettl, Phys. Rev. Lett. **76**, 295 (1996).
- [97] Y. Tokura, A. Urushibara, Y. Moritomo, T. Arima, A. Asamitsu, G. Kido, and N. Furukawa, J. Phys. Soc. Jpn. **63**, 3931 (1994).
- [98] J. Ye, Y. B. Kim, A. J. Millis, B. I. Shraiman, P. Majumdar, and Z. Tešanović, Phys. Rev. Lett. **83**, 3737 (1999).
- [99] L. Friedman and T. Holstein, Ann. Phys. (N.Y.) **21**, 494 (1963).
- [100] M. Jaime, H. T. Hardner, M. B. Salamon, M. Rubenstein, P. Dorsey, and D. Emin, Phys. Rev. Lett. **78**, 951 (1997).
- [101] M. Jaime, H. T. Hardner, M. B. Salamon, M. Rubenstein, P. Dorsey, and D. Emin, J. Appl. Phys. **81**, 4958 (1997).

- [102] A. Asamitsu and Y. Tokura, *Phys. Rev. B* **58**, 47 (1998).
- [103] P. Matl, N. P. Ong, Y. F. Yan, Y. Q. Li, D. Studebaker, T. Baum, and G. Doubinina, *Phys. Rev. B* **57**, 10248 (1998).
- [104] S. H. Chun, M. B. Salamon, and P. D. Han, *Phys. Rev. B* **59**, 11155 (1999).
- [105] W. E. Pickett and D. J. Singh, *Phys. Rev. B* **55**, R8642 (1997).
- [106] P. Wagner, I. Gordon, A. Vantomme, D. Dierickx, M. J. van Bael, V. V. Moshchalkov, and Y. Bruynseraede, *Europhys. Lett.* **41**, 49 (1998).
- [107] M. Ziese and C. Sritiwarawong, *Europhys. Lett.* **45**, 256 (1999).
- [108] P. G. Radaelli, D. E. Cox, M. Marezio, S.-W. Cheong, P. E. Schiffer, and A. P. Ramirez, *Phys. Rev. Lett.* **75**, 4488 (1995).
- [109] A. S. Alexandrov and A. M. Bratkovsky, *Phys. Rev. Lett.* **82**, 141 (1999).
- [110] H. Y. Hwang, S.-W. Cheong, N. P. Ong, and B. Batlogg, *Phys. Rev. Lett.* **77**, 2041 (1996).
- [111] A. Gupta, G. Q. Gong, G. Xiao, P. R. Duncombe, P. Lecoeur, P. Trouilloud, Y. Y. Wang, V. P. Dravid, and J. Z. Sun, *Phys. Rev. B* **54**, R15629 (1996).
- [112] B. Mayer, L. Alff, T. Träuble, R. Gross, P. Wagner, and H. Adrian, *Appl. Phys. Lett.* **63**, 996 (1993).
- [113] N. D. Mathur, G. Burnell, S. P. Isaac, T. Jackson, B. S. Teo, J. L. MacManus-Driscoll, L. F. Cohen, J. Evetts, and M. G. Blamire, *Nature (London)* **387**, 266 (1997).
- [114] K. Steenbeck, T. Eick, K. Kirsch, H.-G. Schmidt, and E. Steinbeiß, *Appl. Phys. Lett.* **73**, 2506 (1998).
- [115] J. S. Moodera, L. R. Kinder, T. M. Wong, and R. Meservey, *Phys. Rev. Lett.* **74**, 3273 (1995).
- [116] X. W. Li, Y. Lu, G. Q. Gong, G. Xiao, A. Gupta, P. Lecoeur, J. Z. Sun, Y. Y. Wang, and V. P. David, *J. Appl. Phys.* **81**, 5509 (1997).
- [117] M. Viret, M. Drouet, J. Nassar, J. P. Contour, C. Fermon, and A. Fert, *Europhys. Lett.* **39**, 545 (1997).
- [118] J. M. DeTeresa, A. Barthélémy, A. Fert, J. P. Contour, R. Lyonnet, F. Montaigne, P. Seneor, and A. Vaurès, *Phys. Rev. Lett.* **82**, 4288 (1999).

- [119] C. Kwon, Q. X. Jia, Y. Fan, M. F. Hundley, D. W. Reagor, J. Y. Coulter, and D. E. Peterson, *Appl. Phys. Lett.* **72**, 486 (1998).
- [120] R. Mathieu, P. Svedlindh, R. A. Chakalov, and Z. G. Ivanov, *cond-mat/0007194* (unpublished).
- [121] H. S. Wang and Q. Li, *Appl. Phys. Lett.* **73**, 2360 (1998).
- [122] J. E. Núñez-Regueiro, D. Gupta, and A. M. Kadin, *J. Appl. Phys.* **79**, 5179 (1996).
- [123] J. C. Simmons, *J. Appl. Phys.* **34**, 1793 (1963).
- [124] J. C. Simmons, *J. Appl. Phys.* **34**, 2581 (1963).
- [125] M. Jullière, *Phys. Lett.* **54B**, 225 (1975).
- [126] M. Tinkham, *Introduction to Superconductivity, International Series in Pure and Applied Physics*, 2nd ed. (McGraw-Hill, Inc., Singapore, 1996), p. 74.
- [127] A. Sommerfeld and H. Bethe, in *Handbuch der Physik*, edited by H. Geiger and K. Schell (Springer, Berlin, 1933), Vol. 24/2, p. 450.
- [128] J. C. Simmons, *J. Appl. Phys.* **34**, 238 (1963).
- [129] J. M. Rowell, in *Tunneling Phenomena in Solids*, edited by E. Burstein and S. Lundqvist (Plenum Press, New York, 1969), p. 385.
- [130] R. H. Fowler and L. Nordheim, *Proc. Roy. Soc. A (London)* **119**, 173 (1928).
- [131] S. P. Isaac, N. D. Mathur, J. E. Evetts, and M. G. Blamire, *Appl. Phys. Lett.* **72**, 2038 (1998).
- [132] M. J. Calderón, L. Brey, and F. Guinea, *Phys. Rev. B* **60**, 6698 (1999).
- [133] X. W. Li, A. Gupta, G. Xiao, and G. Q. Gong, *Appl. Phys. Lett.* **71**, 1125 (1997).
- [134] J. E. Evetts, M. G. Blamire, N. D. Mathur, S. P. Isaac, B. Teo, L. F. Cohen, and J. L. Macmanus-Driscoll, *Phil. Trans. R. Soc. Lond. Ser. A* **356**, 1593 (1998).
- [135] J. Klein, C. Höfener, S. Uhlenbruck, L. Alff, B. Büchner, and R. Gross, *Europhys. Lett.* **47**, 371 (1999).
- [136] L. I. Glazman and K. A. Matveev, *Sov. Phys. JETP* **28**, 1276 (1988).

- [137] R. Gross, L. Alff, B. Büchner, B. H. Freitag, C. Höfener, J. Klein, Y. Lu, W. Mader, J. B. Philipp, M. S. R. Rao, P. Reutler, S. Ritter, S. Thienhaus, S. Uhlenbruck, and B. Wiedenhorst, *J. Magn. Magn. Mater.* **211**, 150 (2000).
- [138] C. Höfener, J. B. Philipp, J. Klein, A. Marx, B. Büchner, and R. Gross, cond-mat/0005158 (unpublished).
- [139] A. Shengelaya, G. Zhao, H. Keller, and K. A. Müller, *Phys. Rev. Lett.* **77**, 5296 (1996).
- [140] J. M. D. Coey, M. Viret, L. Ranno, and K. Ounadjela, *Phys. Rev. Lett.* **75**, 3910 (1995).
- [141] G. F. Dionne, *J. Appl. Phys.* **79**, 5172 (1996).
- [142] J. S. Moodera, J. Nowak, and R. J. M. van de Veerdonk, *Phys. Rev. Lett.* **80**, 2941 (1998).
- [143] F. K. Patterson, C. W. Moeller, and R. Ward, *Inorg. Chem.* **2**, 196 (1963).
- [144] F. S. Galasso, F. C. Douglas, and R. J. Kasper, *J. Chem. Phys.* **44**, 1672 (1966).
- [145] T. Nakagawa, *J. Phys. Soc. Jpn.* **24**, 806 (1968).
- [146] S. Nakayama, T. Nakagawa, and S. Nomura, *J. Phys. Soc. Jpn.* **24**, 219 (1968).
- [147] M. T. Anderson, K. B. Greenwood, G. A. Taylor, and K. R. Poeppelmeier, *Prog. Solid. St. Chem.* **22**, 197 (1993).
- [148] C. Stölzel, Ph.D. thesis, Technische Hochschule Darmstadt, 1995.
- [149] B. Nadgorny, private communication.
- [150] L. H. Brixner, *J. Inorg. Nucl. Chem.* **14**, 225 (1960).
- [151] H. L. Yakel, *Acta Crystallogr.* **8**, 394 (1955).
- [152] B. García-Landa, C. Ritter, M. R. Ibarra, J. Blasco, P. A. Algarabel, R. Mahendiran, and J. García, *Solid State Commun.* **110**, 435 (1999).
- [153] Y. Tomioka, T. Okuda, Y. Okimoto, R. Kumai, K.-I. Kobayashi, and Y. Tokura, *Phys. Rev. B* **61**, 422 (2000).
- [154] A. Dorn, Master's thesis, Johannes Gutenberg-Universität Mainz, 2000.

- [155] H. Asano, S. B. Ogale, J. Garrison, A. Orozco, Y. H. Li, E. Li, V. Smolyaninova, C. Galley, M. Downes, M. Rajeswari, R. Ramesh, and T. Venkatesan, *Appl. Phys. Lett.* **74**, 3696 (1999).
- [156] J. Kondo, *Prog. Theor. Phys.* **32**, 37 (1964).
- [157] M. Viret, L. Ranno, and J. M. D. Coey, *Phys. Rev. B* **55**, 8067 (1997).
- [158] A. Maignan, B. Raveau, C. Martin, and M. Hervieu, *J. Solid State Chem.* **144**, 224 (1999).
- [159] T. Manako, M. Izumi, Y. Konishi, K.-I. Kobayashi, M. Kawasaki, and Y. Tokura, *Appl. Phys. Lett.* **74**, 2215 (1999).
- [160] D. D. Sarma, E. V. Sampathkumaran, S. Ray, R. Nagarajan, S. Majumdar, A. Kumar, G. Nalini, and T. N. Guru Row, *Solid State Commun.* **114**, 465 (2000).
- [161] J. Lindén, T. Yamamoto, M. Karppinen, H. Yamauchi, and T. Pietari, *Appl. Phys. Lett.* **76**, 2925 (2000).
- [162] G. Bergmann, *Phys. Today* **32**, 25 (1979).
- [163] N. W. Ashcroft and N. D. Mermin, *Solid State Physics*, international ed. (Saunders College, Philadelphia, 1976), pp. 8, 36.
- [164] J. Smit, *Physica (Amsterdam)* **XXI**, 877 (1955).
- [165] C. M. Hurd, in *The Hall Effect in Metals and Alloys, The International Cryogenics Monograph Series*, edited by K. Mendelssohn and K. D. Timmerhaus (Plenum Press, New York, 1972), p. 154.
- [166] L. Pinsard-Gaudart, R. Suryanarayanan, A. Revcolevschi, J. Rodríguez-Carvajal, J. M. Greneche, P. A. I. Smith, R. M. Thomas, R. P. Borges, and J. M. D. Coey, *J. Appl. Phys.* **87**, 7118 (2000).
- [167] A. S. Ogale, S. B. Ogale, R. Ramesh, and T. Venkatesan, *Appl. Phys. Lett.* **75**, 537 (1999).
- [168] R. Boucher, E. Steinbeiß, K. Kirsch, R. Mattheis, M. Bibes, and K. Steenbeck, Symposium on Spin-Electronics Halle, Germany, July 3-6, 2000 (unpublished).
- [169] F. S. Galasso, in *Structure, Properties and Preparation of Perovskite-Type Compounds*, Vol. 5 of *International Series of Monographs in Solid State Physics*, edited by R. Smoluchowski and N. Kurth (Pergamon Press, Oxford, 1969), p. 126.

- [170] J. Longo and R. Ward, *J. Am. Chem. Soc.* **83**, 2816 (1961).
- [171] H. Spiering, L. Deák, and L. Bottyán, *Hyp. Interact.* **125**, 197 (2000).
- [172] R. D. Shannon, *Acta Crystallogr. A* **32**, 751 (1976).
- [173] J. A. Alonso, M. T. Casais, M. J. Martínez-Lope, J. L. Martínez, P. Velasco, A. Muñoz, and M. T. Fernández-Díaz, *Chem. Mater.* **12**, 161 (2000).
- [174] A. F. Hollemann and E. Wiberg, *Lehrbuch der Anorganischen Chemie* (Walter de Gruyter & Co., Berlin, 1964), Vol. 57 – 70, p. 551.
- [175] *International Tables For Crystallography*, 2nd ed., edited by T. Hahn (Kluwer Academic Publishers, Dordrecht, 1987), Vol. A Space-Group Symmetry, p. 177.
- [176] http://www.isis.rl.ac.uk/ISISPublic/reference/Neutron_properties.htm.
- [177] Special Feature Section: Neutron Scattering Lengths and Cross Sections of the Elements and their Isotopes, *Neutron News* **3**, 29 (1992).
- [178] A. M. Glazer, *Acta Crystallogr. B* **28**, 3384 (1972).
- [179] A. M. Glazer, *Acta Crystallogr. A* **31**, 756 (1974).
- [180] C. Giacovazzo, in *Fundamentals of Crystallography*, Vol. 2 of *International Union of Crystallography Texts on Crystallography*, edited by C. Giacovazzo (University Press, Oxford, 1992), p. 148.
- [181] R. Kajimoto, Y. Yoshizawa, H. Kawano, Y. Tokura, K. Ohoyama, and M. Ohashi, *Phys. Rev. B* **60**, 9506 (1999).
- [182] M. K. Wilkinson, E. O. Wollan, H. R. Child, and J. W. Cable, *Phys. Rev.* **121**, 74 (1961).
- [183] N. N. Greenwood and T. C. Gibb, *Mössbauer Spectroscopy* (Chapman and Hall Ltd., London, 1971).
- [184] A. W. Sleight and J. F. Weiher, *J. Phys. Chem. Solids* **33**, 679 (1972).
- [185] J. Gopalakrishnan, A. Chattopadhyay, S. B. Ogale, T. Venkatesan, R. L. Greene, A. J. Millis, K. Ramesha, B. Hannoyer, and G. Marest, cond-mat/0004315 (unpublished).
- [186] P. Gülich, R. Link, and A. Trautwein, *Mössbauer Spectroscopy and Transition Metal Chemistry*, Vol. 3 of *Inorganic Chemistry Concepts* (Springer, Berlin, 1978).

- [187] W. Prellier, V. Smolyaninova, A. Biswas, C. Galley, R. L. Greene, K. Ramesha, and J. Gopalakrishnan, *J. Phys.: Condens. Matter* **12**, 965 (2000).
- [188] R. P. Borges, R. M. Thomas, C. Cullinan, J. M. D. Coey, R. Suryanarayanan, L. Ben-Dor, L. Pinsard-Gaudart, and A. Revcolevschi, *J. Phys.: Condens. Matter* **11**, L445 (1999).
- [189] N. Auth, Master's thesis, Johannes Gutenberg-Universität Mainz, to be published 2001.
- [190] K. Kobayashi, T. Kimura, Y. Tomioka, H. Sawada, K. Terakura, and Y. Tokura, *Phys. Rev. B* **59**, 11159 (1999).
- [191] C. Ritter, M. R. Ibarra, L. Morellon, J. Blasco, J. García, and J. M. De-Teresa, *J. Phys.: Condens. Matter* **12**, 8295 (2000).
- [192] FULLPROF help file:
<http://www.ill.fr/YellowBook/D20/DataTreatment/fullprof.help>.
- [193] D. B. Wiles and R. A. Young, *J. Appl. Cryst.* **14**, 149 (1981).
- [194] R. A. Young, in *The Rietveld Method*, Vol. 5 of *International Union of Crystallography Monographs on Crystallography*, edited by R. A. Young (University Press, Oxford, 1993), p. 22.
- [195] H. Krischner and B. Koppelhuber-Bitschnau, *Röntgenstrukturanalyse und Rietveldmethode, Eine Einführung*, 5th ed. (Vieweg, Braunschweig, 1994), p. 166.
- [196] W. A. Dollase, *J. Appl. Cryst.* **19**, 267 (1986).
- [197] R. A. Young, in *The Rietveld Method*, Vol. 5 of *International Union of Crystallography Monographs on Crystallography*, edited by R. A. Young (University Press, Oxford, 1993), p. 33.
- [198] H. Krischner and B. Koppelhuber-Bitschnau, *Röntgenstrukturanalyse und Rietveldmethode, Eine Einführung*, 5th ed. (Vieweg, Braunschweig, 1994), p. 110.
- [199] J.-F. Béjar and G. Baldinozzi, *J. Appl. Cryst.* **26**, 128 (1993).
- [200] H. Toraya, in *The Rietveld Method*, Vol. 5 of *International Union of Crystallography Monographs on Crystallography*, edited by R. A. Young (University Press, Oxford, 1993), p. 259.

- [201] H. Krischner and B. Koppelhuber-Bitschnau, *Röntgenstrukturanalyse und Rietveldmethode, Eine Einführung*, 5th ed. (Vieweg, Braunschweig, 1994), p. 104.
- [202] R. J. Hill and C. J. Howard, *J. Appl. Cryst.* **20**, 467 (1987).
- [203] G. Caglioti, A. Paoletti, and F. P. Ricci, *Nucl. Inst. Methods* **3**, 223 (1958).
- [204] Obtaining and Installing WINPLOTR/FULLPROF for Windows:
<http://www.ccp14.ac.uk/tutorial/fullprof/wininst.htm>.
- [205] Obtaining and Installing STRUPLO for Windows:
<http://www.chem.gla.ac.uk/~louis/struplo/>.

List of Publications

Magnetoresistivity and crystal structure of epitaxial $\text{La}_{0.67}\text{Ca}_{0.33}\text{MnO}_3$ films

G. JAKOB, F. MARTIN, W. WESTERBURG, AND H. ADRIAN
Proceedings of the International Conference on Magnetism 1997, Cairns, Australia
J. Magn. Magn. Mater. **177–181**, 1247–1248 (1998).

Evidence of charge-carrier compensation effects in $\text{La}_{0.67}\text{Ca}_{0.33}\text{MnO}_3$

G. JAKOB, F. MARTIN, W. WESTERBURG, AND H. ADRIAN
Phys. Rev. B **57**, 10252–10255 (1998).

Small-polaron transport in $\text{La}_{0.67}\text{Ca}_{0.33}\text{MnO}_3$ thin films

G. JAKOB, W. WESTERBURG, F. MARTIN, AND H. ADRIAN
Phys. Rev. B **58**, 14966–14970 (1998).

Growth mechanism and transport properties of thin $\text{La}_{0.67}\text{Ca}_{0.33}\text{MnO}_3$ films

F. MARTIN, G. JAKOB, W. WESTERBURG, AND H. ADRIAN
Proceedings of the 7th European Magnetic Materials and Applications Conference 1998, Zaragoza, Spain
J. Magn. Magn. Mater. **196–197**, 509–511 (1999).

High-temperature transport properties of $\text{La}_{0.67}\text{Ca}_{0.33}\text{MnO}_3$ films

W. WESTERBURG, G. JAKOB, F. MARTIN, AND H. ADRIAN
Proceedings of the 7th European Magnetic Materials and Applications Conference 1998, Zaragoza, Spain
J. Magn. Magn. Mater. **196–197**, 536–538 (1999).

Resistivity and Hall effect at high temperatures in $\text{La}_{0.67}\text{Ca}_{0.33}\text{MnO}_3$

G. JAKOB, W. WESTERBURG, F. MARTIN, AND H. ADRIAN,
P. J. M. VAN BENTUM, AND J. A. A. J. PERENBOOM
Proceedings of the 43rd Conference on Magnetism and Magnetic Materials 1998, Miami, USA
J. Appl. Phys. **85**, 4803–4805 (1999).

**Current dependence of grain boundary magnetoresistance
in $\text{La}_{0.67}\text{Ca}_{0.33}\text{MnO}_3$ films**

W. WESTERBURG, F. MARTIN, S. FRIEDRICH, M. MAIER, AND G. JAKOB
J. Appl. Phys. **86**, 2173–2177 (1999).

**Charge-carrier density collapse in $\text{La}_{0.67}\text{Ca}_{0.33}\text{MnO}_3$ and $\text{La}_{0.67}\text{Sr}_{0.33}\text{MnO}_3$
epitaxial thin films**

W. WESTERBURG, F. MARTIN, AND G. JAKOB, P. J. M. VAN BENTUM,
AND J. A. A. J. PERENBOOM
Eur. Phys. J. B **14**, 509–513 (2000).

Hall effect of epitaxial double-perovskite $\text{Sr}_2\text{FeMoO}_6$ thin films

W. WESTERBURG, F. MARTIN, AND G. JAKOB
Proceedings of the 44th Conference on Magnetism and Magnetic Materials 1999,
San Jose, USA
J. Appl. Phys. **87**, 5040–5042 (2000).

Transport and magnetic properties of $\text{La}_{1-x}\text{Ca}_x\text{MnO}_3$ -films ($0.1 < x < 0.9$)

G. JAKOB, F. MARTIN, S. FRIEDRICH, W. WESTERBURG, AND M. MAIER
Proceedings of the 22nd International Conference on Low Temperature Physics 1999,
Espoo and Helsinki, Finland
Physica B **284–288**, 1440–1441 (2000).

Epitaxy and Magnetotransport of $\text{Sr}_2\text{FeMoO}_6$ thin films

W. WESTERBURG, D. REISINGER, AND G. JAKOB
Phys. Rev. B **62**, R767–R770 (2000).

Crystal structure and transport properties of $\text{Sr}_2\text{FeMoO}_6$ thin films

W. WESTERBURG, D. REISINGER, AND G. JAKOB
Proceedings of the 8th European Magnetic Materials and Applications Conference
2000, Kiyv, Ukraine
Materials Science Forum, accepted.

Magnetic and structural properties of the double-perovskite $\text{Ca}_2\text{FeReO}_6$

W. WESTERBURG, O. LANG, C. RITTER, C. FELSER, W. TREMEL, AND
G. JAKOB
Eur. Phys. J. B, submitted.

Curriculum Vitae

Personal data:

Name: Wilhelm Westerburg
 Date of birth: July 19, 1971
 Place of birth: Nastätten (Germany)
 Nationality: German

School education:

1978 – 1982 Mühlbach-primary-school in Miehlen
 1982 – 1991 Staatliches Wilhelm-Hofmann-Gymnasium in St. Goarshausen
 June 1991 Abitur (school leaving exam and university entrance qualification)

Military service:

July 1991 – Sept. 1992 Compulsory military service

Study of physics:

October 1992 Inscription in the department of physics at the Johannes Gutenberg-University Mainz
 October 1994 Intermediate diploma
 Dec. 1996 – Feb. 1998 Diploma work at the institute of Physics, supervised by Prof. Dr. H. Adrian,
‘Aufbau eines Hochtemperatur-Hochfeld-Meßplatzes und Untersuchung der Magnetotransporteigenschaften von $La_{1-x}Ca_xMnO_3$ -Filmen’
 Februar 1998 Diploma in physics
 March 1998 Beginning of Ph.D. research as academic employee of the Johannes Gutenberg-University Mainz at the institute of physics
 July 23, 2001 doctoral examination

Danksagung (Acknowledgements)

An dieser Stelle möchte ich allen, auch den nicht namentlich erwähnten, die in irgendeiner Weise zum Gelingen dieser Arbeit beigetragen haben, ganz herzlich danken.

Herrn Prof. Dr. Hermann XXXXXX danke ich für die Chance diese Promotion in seiner sehr gut ausgestatteten Arbeitsgruppe durchzuführen. Weiterhin möchte ich mich bei ihm für die Gelegenheit bedanken meine Ergebnisse auf mehreren Konferenzen im In- und Ausland vorzustellen. Seine Korrektur hat die Qualität dieser Arbeit wesentlich verbessert.

Herrn Dr. Gerhard XXXXXX danke ich für seine vorbildliche Unterstützung und Betreuung meiner Promotion. Er nahm sich immer die Zeit bei auftretenden Problemen und war immer zu Diskussionen bereit. Es gibt quasi nichts was der Kerl nicht weiß und was er nicht weiß, weiß auch kein anderer normal Sterblicher. Durch seine Ideen zu Experimenten und Theorien wurden viele Publikationen und am Ende diese Arbeit erst möglich. Ich danke ihm auch für die Korrektur dieser Arbeit.

Meinem Mitstreitern auf dem Gebiet der magnetischen Perowskite, dem Westwäller Doktoranden Dipl.-Phys. Frank XXXXXX, den Diplomanden Daniel XXXXXXXXXXXX und Nicole XXXX, sowie dem Austauschstudenten Pedro Latorre XXXXXXXX danke ich für die sehr gute Zusammenarbeit und experimentelle Unterstützung.

Dem Fachmann für Laserablation Dipl.-Phys. Markus XXXXXX, auch ein Westwäller, danke ich für die Benutzung seiner perfekt konstruierten Anlage. Nur durch seine technische Hilfe war es überhaupt möglich beide Laser und Kammern in Betrieb zu halten.

Besonders möchte ich meinem sympathischen Zimmerkollegen, dem Rheingauer Dipl.-Phys. Michael XXXXXX danken. Er machte durch seine offene und hilfsbereite Art den doch oft trockenen Alltag angenehmer. Gedankt sei ihm auch für sein soziales Engagement innerhalb der Gruppe und für die Korrektur dieser Arbeit.

Für das ausgezeichnete Arbeitsklima und die fruchtbare Zusammenarbeit danke ich allen weiteren ehemaligen und momentanen Mitgliedern der Arbeitsgruppe.

Neben der Wissenschaft gab es immer auch noch etwas Zeit für diverse Feiern, bei denen öfters einiges an Alkohol vernichtet wurde. An dieser Stelle sei besonders Herrn Dr. Patrick XXXXXXXX, auch El Haib genannt, gedankt.

Den Pulverexperten Dipl.-Chem. Olaf XXXX und Dipl.-Chem. Irene XXXX aus dem AK Tremel danke ich für die Pulverpräparation in großen Mengen, durch die die Neutronenstreuungen erst möglich wurde.

Für die durchgeführten Mössbauermessungen an $\text{Ca}_2\text{FeReO}_6$ danke ich Dipl.-Chem. Markus XXXXXXXX und Dr. Franz XXXX aus dem AK Gütlich.

Danken möchte ich auch Dr. Jos XXXXXXXXXXXX, Dr. Jan van XXXXXXXX und Harry XXXXXXXX für die Hilfe während der Hochfeldmessungen am High Field Magnet Laboratory in Nijmegen.

Herrn Dr. Clemens XXXXXXX, dem 'local contact' am ILL danke ich für die Unterstützung bei den Neutronenstreuungen und Rietveld refinements.

Herrn Dipl.-Ing. Jürgen XXXXXXXX, auch Ricci genannt, danke ich für die technische Unterstützung bei einer Vielzahl von Problemen und Frau Anja Dion für viele REM und AFM Bilder.

Die für die Experimente so lebenswichtige Versorgung mit flüssigem Helium verdanke ich Herrn XXXXXXX und Herrn XXXXX.

Bei Frau XXXXX bedanke ich mich für die Entwicklung zahlreicher Schwarzweißfilme.

Herrn Joachim XXXXXXXX danke ich für das Ansetzen der Pulverproben.

Den Mitarbeitern des Forschungszentrums Karlsruhe Herrn Dr. G. XXXXXXX und Dr. J. XXXXX danke ich für die Rutherford-Rückstreu-Analyse der Manganoxid- und Doppelperowskitschichten.

Bedanken möchte ich mich auch bei Dr. habil. Leonore XXXXX für die Justage der Vierkreiser Röntgenanlage.

Ebenso trug die Mechanik- und die Elektronik-Werkstatt des Instituts zum Gelingen des Projektes bei.

Schließlich möchte ich mich ganz herzlich bei meinen Eltern und meiner Freundin Nicole für ihr Verständnis und ihre Unterstützung bedanken. Sie haben mit mir zusammen alle Belastungen getragen, die mit dieser Arbeit verbunden waren.

Diese Arbeit wurde durch die Deutsche Forschungsgemeinschaft Projekt Ja821/1-3 und das Materialwissenschaftliche Forschungszentrum Mainz gefördert.